Université de Lille

iemn

Thèse de doctorat de l'Université de Lille

École Doctorale Sciences Pour l'Ingénieur
IEMN - Institut d'électronique de microélectronique et de nanotechnologie

Thèse défendue par **Vincent Notot**

Soutenue le 22/01/2021

Pour obtenir le titre de DOCTEUR DE L'UNIVERSITE

Spécialité **Electronique, microélectronique, nanoélectronique et micro-ondes**

Propriétés électroniques et de transport des super-réseaux de boites quantiques épitaxiallement connectées

---

Composition du jury

Emmanuel	**LHUILLIER**	INSP	**Rapporteur**	*President du jury*
Laurence	**RESSIER**	LPCNO	**Rapporteure**	
Peter	**REISS**	SYMMES	**Examinateur**	
Odile	**ROBBE**	PhLAM	**Examinatrice**	
Bruno	**GRANDIDIER**	IEMN	**Directeur de thèse**	
Louis	**BIADALA**	IEMN	**Co-Directeur de thèse**	

Abstract

Semiconductor colloidal quantum dots are fluorescent semiconductors of nanometric size, generally between 2 and 10 nm. These materials have raised the interest of the scientific community for more than thirty years because of their particular opto-electronic properties, which result from the strong confinement of charge carriers. Thanks to on-going developments in their chemical synthesis to produce monolayers of nanocrystals whose facets can now be fused, electronic coupling between quantum dots within arrays is now within reach. However, electronic transport in such a network is still limited and requires further study at the scale of the single nanocrystal.

Scanning tunneling microscopy is a suitable tool for studying the electronic properties of individual nanostructures. In this work, this technique was used to characterize square superlattices of lead selenide quantum dots. To begin with, we studied the electronic and structural properties of a superlattice deposited on a gold substrate. After annealing the samples to ensure high stability of the tunnel junction, tunnel spectroscopy revealed a p-doped monolayer comprising two types of nanocrystals: those, the majority, exhibiting discrete states on both sides of the band gap, where the analysis of the width of the peaks shows a more or less pronounced coupling of the valence band states and those, in lower concentration, having a peak in the forbidden band. To better understand the origin of this peak, the superlattice was also studied on a thin layer of silicon oxide that electronically decouples the grating from the silicon substrate. In this case, the appearance of vibronic states associated with the peak in the band gap indicates the presence of localized states. These traps are attributed to the loss of ligands on certain facets of the nanocrystals. By keeping these facets passivated with ligands, the transport properties of the superlattices were finally investigated by multi-tip scanning tunneling microscopy. Conductivity measurements show the importance of film cracks on the electrical conduction. However, at the micrometer scale, state-of-the-art conductivities of the order of 10-5 S have been obtained, demonstrating the interest of fusing colloidal quantum dots to tend towards band transport.

Résumé

Les boites quantiques colloïdales semiconductrices sont des semi-conducteurs fluorescents de taille nanométrique, généralement comprises entre 2 et 10 nm. Ces matériaux ont suscité l'intérêt de la communauté scientifique depuis plus de trente ans en raison de leurs propriétés opto-électroniques particulières qui résultent du fort confinement des porteurs de charge. Grâce aux développements continuels de leur synthèse chimique pour produire des mono-couches de nanocristaux dont les bords peuvent être à présent fusionnés, le couplage électronique entre boîtes au sein de réseaux semble à portée de main. Cependant, le transport électronique dans de tel réseau est encore limité et nécessite une étude approfondie à l'échelle du nanocristal unique.

La microscopie à effet tunnel est un outil adéquat pour étudier les propriétés électroniques de nanostructures individuelles. Dans ce travail, cette technique a été utilisée pour caractériser des super-réseaux carrés de boîtes quantiques de séléniure de plomb. Pour commencer, nous avons étudié les propriétés électroniques et structurelles d'un super-réseau déposé sur un sub-strat en or. Après recuit des échantillons pour assurer une grande stabilité de la jonction tunnel, la spectroscopie tunnel a révélé une monocouche dopée p comportant deux types de nanocristaux : ceux, majoritaires, présentant des états discrets de part et d'autre de la bande in-terdite, dont l'analyse fine de la largeur des pics montre un couplage plus ou moins prononcé des états de bande de valence et ceux, en moindre concentration, possédant un pic dans la bande interdite. Pour mieux comprendre l'origine de ce pic, le super-réseau a également été étudié sur une fine couche d'oxyde de silicium qui découple électroniquement le réseau du substrat de silicium. Dans ce cas, l'apparition d'états vibroniques associés au pic dans la bande interdite indique la présence d'états localisés. Ces pièges sont attribués à la perte de ligands sur certaines facettes des nanocristaux. En conservant la passivation de ces facettes par des ligands, les propriétés de transport de super-réseaux ont finalement été étudiées par microscopie à effet tunnel à pointes multiples. Des mesures de conductivité montre l'importance des fissures du film sur la conduction électrique. Néanmoins à l'échelle du micromètre, des conductivités à l'état de l'art de l'ordre de 10-5 S ont été obtenues, démontrant l'intérêt de fusionner les boîtes quantiques colloïdales pour tendre vers un transport de bande.

Acknowledgements

Contents

Introduction

Since their discovery, colloidal semiconductor quantum dots (QDs) have been seen as an interesting alternative in the deposition of semiconductor thin film thanks to their electronic properties tuneable by size, shape and composition. The ability to absorb and emit light at different wavelengths make them very attractive for a plethora of optoelectronic applications ranging from remote phosphor emitters in commercially available display screens to potential super-emitters for quantum communication. Moreover, their rather easy synthesis as dispersed colloids allows them to be directly used in solution-based processes, such as spin- or dip-coating, drop casting or doctor-blading.

Colloidal QDs are widely used as building block for self-assembled array. QDs deposited thin films consist of ordered or randomly packed QD assemblies where each QD is separated from its nearest neighbour by capping ligands. However, the presence of these ligands is problematic for applications relying on charge transport. The recent development of synthesis protocol enabling the formation of superlattices of epitaxially connected colloidal QDs has the potential to overcome this problem. The elimination of any tunnelling barrier between adjacent QD was expected to yield high mobility and band-like charge transport. Unfortunately, these materials has so far not exhibited the great enhancement in carrier mobility nor the band transport predicted by theoretical calculation. Therefore, to get better understanding of the transport properties of these QD superlattice, experimental investigation of individual QD in the superlattice as well as information on the local transport properties are mandatory. By mean of scanning tunnelling microscopy (STM) and spectroscopy (STS) under cryogenic conditions, this thesis aims at the study of the electronic and transport properties of PbSe QD superlattice.

This thesis is divided into five chapters. The first chapter describes the context in which this work takes place. The attention will be turned to the of quantum dots array materials and the self-assembly of epitaxially connected quantum dots. In particular, we will describe the electronic and transport properties of these materials. We will show that structural disorder and defects still limits the full potential of the QD solid.

The second chapter deals with the experimental techniques used in this work. A theoretical background of scanning tunnelling microscopy (STM) and spectroscopy (STS) are provided. It

starts with a description of the tunnel effect up to the presentation of the microscope. A special focus is given to the STS on quantum dots and the peculiar tunnelling regimes occurring when a quantum dot is inserted in a double barrier tunnel junction. In a second step, multi probe scanning tunnelling microscopy is presented, starting with a brief explanation of the four-point measurements and a list of probe configurations to readily get access to the resistivity of the materials depending. Then a detailed presentation of the microscope, from the UHV system to the preparation of the tips, is given.

In the third chapter, we will inverstigate the electronic properties the PbSe QD superlattice deposited on a gold substrate. STM and scanning transmission electronic microscopy (STEM) are used to characterize the QD array. High resolved STEM images reveal the atomic connection between the QDs and the long-range square order of the superlattice, which is also found in STM. STS was first performed on QDs in the superlattice to investigate the electronic properties of the as-synthesized sample. A lack of homogeneity in the measured spectra, which was attributed to the large discrepancy in the nano-environment. We will show that annealing the superlattice at 120 °C leads to a stable and reproducible spectroscopy of the QDs across the superlattice. While clear peaks corresponding to the discrete levels of the QDs are resolved, we show that the QDs are p-type doped and that only the hole states contribute to the tunneling current. From the analysis of the linewidth, we show a to quantum mechanical coupling between the QDs. The hallmark of band formation is observed in a few regions of the sample. Finally, a small amount of QDs show a peak in the apparent band gap measured with STS.

In the fourth chapter, we will address the exact nature of an in-gap state observed in the STS spectra by changing the host substrate. By replacing the gold susbtrate with a highly doped silicon substrate terminated with an oxide layer, the lever arm of the double barrier tunnel junction becomes more asymmetric. This will enable us to reverse the potential distribution across the junction in comparison with the gold substrate used in the second chapter. In such a way, the lever arm reaches values below 0.5 and allows to expand the energy scale to get more insight into the peak shape, highlighting the contribution of vibronic states to the tunneling current and the importance of residual charges at the interface between the superlattice and the SiO_2 surface.

The fifth chapter will focus on the study of the local transport properties of the superlattice. By performing four-probe STM transport measurements, we will study the PbSe QD superlattices in a controlled and non-destructive way. While a first linear probe configuration is used in order to measure the sample conductivity, a second square probe configuration shows the presence of a conductance anisotropy. We unveil the origin of the conductance anisotropy by studying the structural morphology of the superlattice which is obtained from high resolution scanning electronic microscopy images. We conclude the chapter by an estimation of the charge mobility of the sample.

Chapter 1

Individual and superlattice of quantum dots semiconductor

1.1 The quantum confinement effect

Classification of nanostructures

a)   b)   c)   d)

3D (bulk)   2D (quantum well)   1D (quantum wire)   0D (quantum dote)
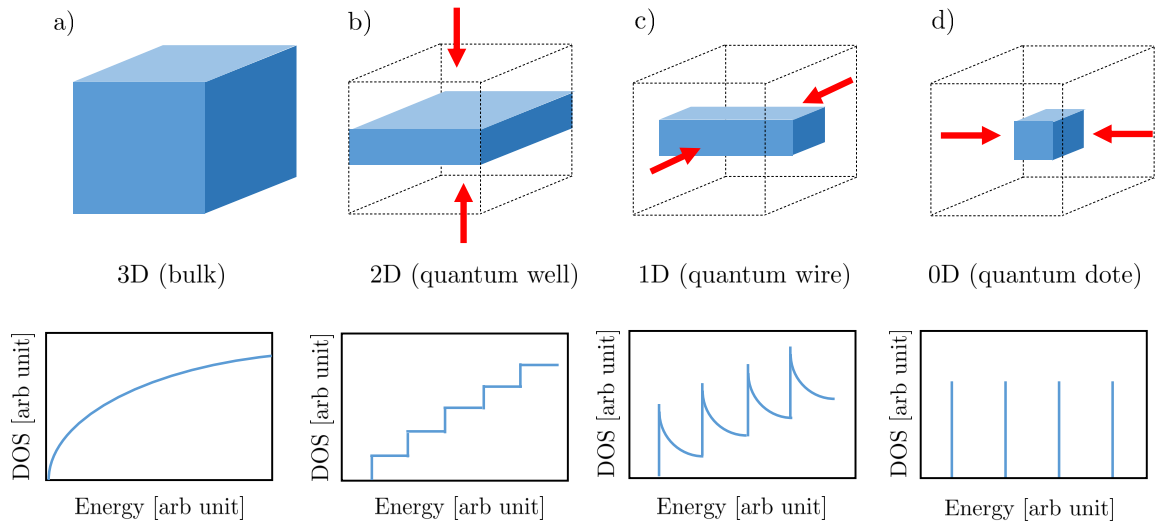
Figure 1.1: Schematic representation of a macroscopic semiconductor with different dimensions. The associated DOS of each case is represented below. The bulk semiconductor (3D) shows a quasi continuous band of states. The quantum well (2D) exhibits a step like form representative of the formation of band states while the nanowire/nanorod (1D) shows Van Hove singularities in their DOS. For the quantum dot (0D), the DOS shows sharp and discrete peaks corresponding to single quantum states.

When one of the dimension is reduced to the nanoscale, materials show very fascinating properties. The quantum confinement effect emerges from this size reduction. According to the geometrical constrains, the quantum size effect produces a discreteness of the accessible carri-

ers energies. In such quantum-confined systems, several parameters, assumed to be constant in bulk semiconductors, are instead dependent of the dimension of the material. For instance, the band gap, the band edge positions and density of state (DOS) (see Figure **??**) change due to quantum confinement. Therefore, semiconductor quantum structures are classified in accordance to the number of degrees of freedom experienced by electrons and holes inside the material.

Quantum Well : Quantum wells are thin structures with thicknesses of the order of a few nanometers. They are described as two-dimensional structures as the charge carriers can move freely along two directions. Their DOS exhibits a step like shape [**?**].

Quantum rods : These are one-dimensional (1D) structures in which electrons are free to move in one direction, while quantization occurs in the remaining two directions. They appear like tubes and wires with diameters in the nanometer range and lengths of several micrometers. Quantum rods show $E^{-1/2}$ dependence for each discrete group of energy levels, called Van Hove singularities.

Quantum dots : QDs are nanosized crystals composed of several tens to a few thousand atoms. These structure are described as zero-dimensional (0D) objects because the electrons and holes are totally confined and behave as stationnary waves. The QD DOS consists of discrete peaks [**?**].

1.1.1 What are QDs ?

QDs are a class of materials in which quantum confinement effects are strongly enhanced. They correspond to small semiconductor crystals with a size on the order of a few nanometers. From a fundamental point of view the QDs are described by the text-book example of the 'particle in a box' problem. A QD is thus a 0D material and exhibits discrete quantized levels (see Figure **??**). This is due to confinement effects that collapse the continuous density of states of bulk solids into discrete "atomic-like" electronic states. Particularly, QDs are significant for optoelectronic applications due to their precisely tunable bandgap and emission color. Indeed, by properly adjusting the size of a QD one can precisely tailor its properties for the desired applications.

Because of their unique properties, nanostructures are good candidates for many applications in the development of novel optoelectronic devices including solar cells, LEDS, transistor or photodetector [**?**, **?**, **?**, **?**, **?**]. In several cases, research has even been translated into the production of commercial devices. For example, in 2019, Samsung announced the creation of a quantum-dot-based display of 4 inch with higher definition and lower power consumption than commercial liquid crystal display. Many other companies start using QDs technology for enhanced resolution, such as Sony (through the company QD vision) or Amazon with the Ama-

zon Kindle [**?**].

Depending on their growth technique, two main classes of QDs exist :

Epitaxial quantum dots : The epitaxial QDs correspond to a wide range of structures where an epitaxial growth is used. These QDs can be fabricated thanks to lithographic patterning of epitaxial quantum well [**?**], self-assembly induced by Stranksky-Krastanow growth mode [**?**] , droplet-epitaxy [**?**], etc. Epitaxial quantm dots are usually flat-shaped (see Figure**??** (a)) with a height along the growth direction of a few nm while the in-plane extension can go from 10 nm to tens of nm. The large range of accessible sizes (up to 100 nm) for the epitaxial QD is an advantage, but unfortunately the quality of the confinement and the minimal size of the QDs are still limited. Epitaxial QDs find application in lasers working in the near infrared wavelength range (from 0.9μm to 1.3μm), communication and information processing to replace classic wire circuits (energy saving and operation speed-up). However, the cost of production of the epitaxial QDs is high since it requires ultra high vacuum equipment like molecular beam epitaxy machines and the evaporation cells need to be filled with expensive high purity materials. One the other hand, from one wafer, one can fabricate millions of devices at once.
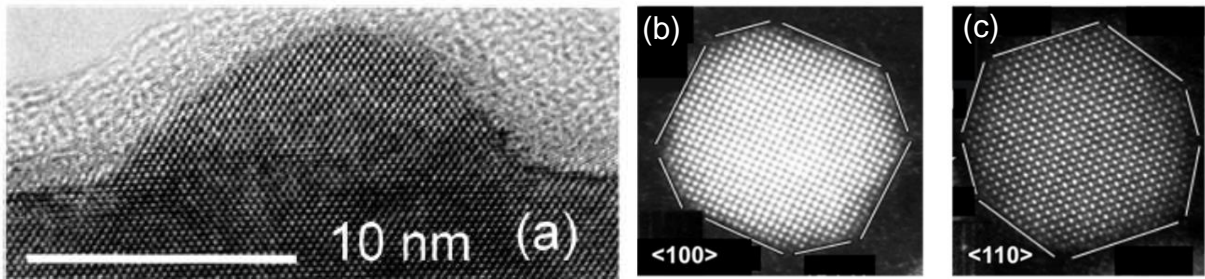
Figure 1.2: (a) Cross-sectionnal TEM image of an uncapped InAs-GaAs self-assembled QD. Figure taken and adapted from[**?**]. (b) and (c) HAADF-STEM images of a PbSe QD. The perpendicular direction to the plane is (b) <110> . Atomic columns are seen, each consisting of equal numbers of Pb and Se, (c) <100> and the column of pure Pb (bright) and pure Se (dark gray) are seen. Figures taken and adapted from [**?**].

Colloidal nanocrystals : Colloidal QDs on the other hand allow for a strong confinement regime as the typical size of these QDs is below 10 nm (see Figure **??** (b) and (c)). For the colloidal QDs, corresponding precursors are injected in a solvent and mixed in a flask at moderate temperatures which is cheaper than the growth of epitaxial QDs. The shape of QDs is very flexible and a wide catalog of forms and sizes can be found in the literature. Shapes from star shape QD [**?**], nanoplatelets [**?**] (2D quantum well), cubes [**?**], nanorods [**?**] (quasi-1D) and many fancy others shapes [**?**] have been synthesized. Moreover colloidal QDs are very versatile in terms of composition. A lot of studies has been done with II-VI compounds (PbSe, PbS, CdSe,ZnSe, ect) and few others with III-V compounds based QDs (such as InAs or InP). Moreover, the small size of these systems allows to reach the strong confinement regime which easily enables one

4

to tailor the optical transition over a very broad range. While the synthesis of colloidal QDs is cheap and easy, integration into the devices may be trickier and technologically challenging.

1.1.2 Quantum confinement in semiconductor QDs

Quantum confined exciton

Inside a bulk crystalline semiconductor, an electron from the conduction band and a hole from the valence band can be paired together thank to Coulombic interaction to form an exciton. The exciton is characterized by its Rydberg energy Ry^* defined by :

$$Ry^* = \frac{e^2}{2\epsilon_r a_B} = \frac{\mu e^4}{2\epsilon_r^2 \hbar^2} = \frac{\mu}{m_0} \frac{1}{\epsilon_r^2} \times 13.6 \tag{1.1}$$

where m_0 is the free electron mass, ϵ_r the relative permittivity of the material, $\mu = 1/m_e^* + 1/m_h^*$ is the reduce effective mass of the exciton and 13.6 is the Rydberg energy of the hydrogen atom. By analogy with the hydrogen atom, an exciton is also described by its Bohr radius :

$$a_B = \frac{\epsilon_r \hbar^2}{\mu e^2} \tag{1.2}$$

The Bohr radius corresponds to the mean distance between the electron and the hole. By comparing the size of the QD to the exciton Bohr radius it is possible to determine when the confinement energy will be dominant over the Coulombic energy of the exciton. Depending on the Bohr radius of the material, two kinds of confinement regime can be distinguished :
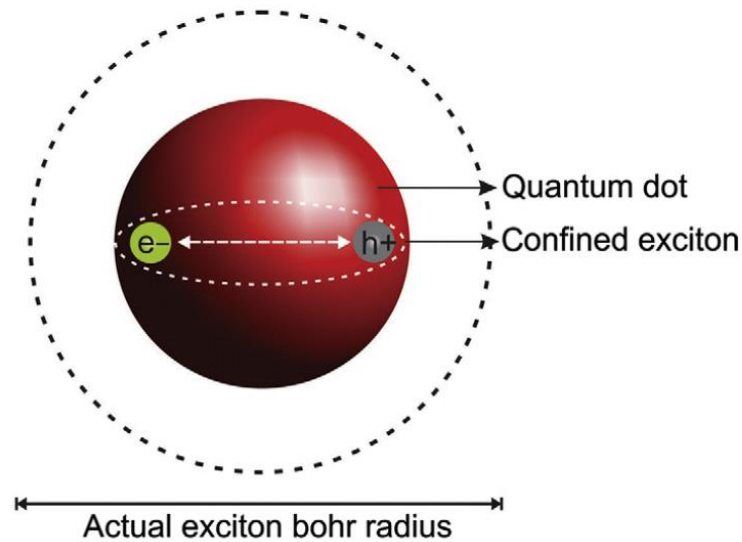
Figure 1.3: Comparison of exciton radius and QD size. Figure taken from [?]

Weak confinement regime : In this case, the exciton Bohr radius is smaller than the QD size. The quantum confinement is negligible compared to the Coulombic interaction and therefore, the effect of the confinement is treated as a perturbation.

Strong confinement regime : The exciton Bohr radius is larger than the QD size. This time the exciton is strongly confined in the QD (see Figure **??**) and it is the Coulombic interaction which is treated as perturbation.

For example, the Bohr exciton radius is about 5.4nm for CdSe [**?**, **?**] and 46 nm for PbSe [**?**]. In our work, the PbSe QDs will have a diameter of 5.8 nm. Therefore our QDs belong to the strong confinement regime.

QD as a large molecule

In analogy with molecules, the electronic structure of a single QD can be described by the Linear Combination of Atomic Orbital (LCAO). The diatomic hydrogen molecule is the simplest example of multiple electron molecule. The two atomic orbitals combine to form two molecular orbitals (MOs) that spread out over the two H atoms. The two MOs are called bonding and anti-bonding MOs. The bonding MO is lower in energy than the individual atomic orbitals. On the contrary, the anti-bonding MO is higher in energy. The electrons occupy the different orbitals in a way that minimizes the potential energy. Therefore, in the H_2 molecule both electrons occupy the bonding MO, leaving the anti-bonding MO empty. The highest occupied molecular orbital is referred as HOMO and the lowest unoccupied molecular orbital is called LUMO. For larger material, the number of atomic orbitals combined to form MOs increases. The bigger the material, the more energy levels are created which decrease the HOMO-LUMO bandgap. Thanks to the large number of atom the energy states due to the MOs of a bulk material lye very close to each another and constitute a quasi-continuum or a band. The HOMO level is the top of the VB, whereas the LUMO is the bottom of the CB. For a semiconductor QD the number of atoms is less important ((10^2 to 10^5) than in the bulk. The electronic structure will be characterized by energy bands with a large density of levels and discrete energy levels near the band edges, where the density of MOs is small. The HOMO-LUMO bandgap is larger than for the QDs for the bulk material. Moreover, in the case of QDs, this gap is size dependent and decreasing with increasing number of atoms in the QD. This approach gives a simple yet general description of the electronic structure of a QD. Moreover it illustrates clearly the reasons of the size dependence of the bandgap in QDs. The profound impact of spatial confinement on the optical properties on colloidal QDs is illustrated in Figure**??**.
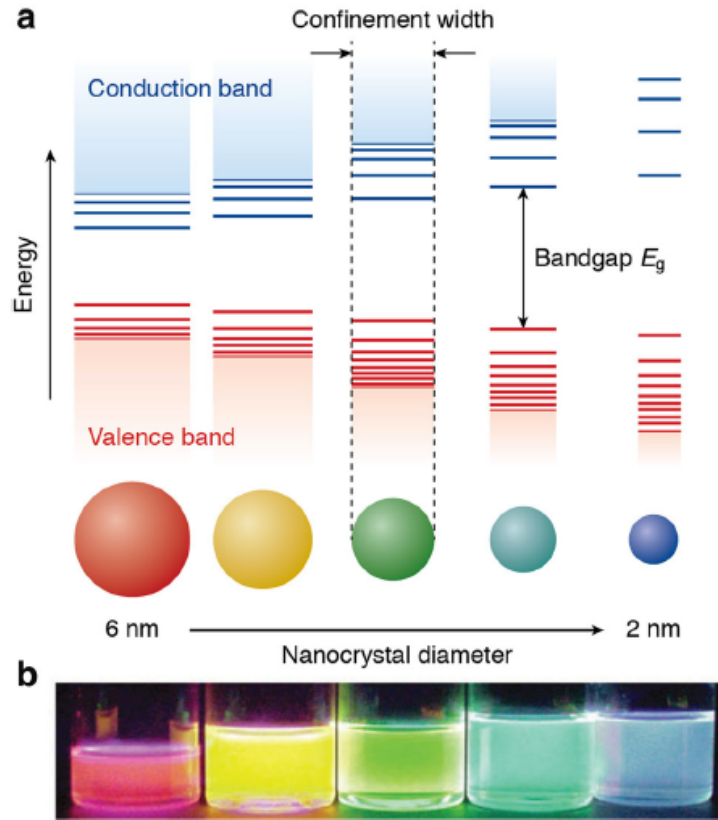
Figure 1.4: a) Simplified schematic of the energy levels in QDs with increasing confinement. The bandgap of the semiconductor particle increases with decreasing size. Taken from [?]. b) Photograph of five colloidal dispersion of CdSe QDs with decreasing size (from 6 to 2 nm). The color of the light emitted by the QDs change from red to blue, under UV excitation. Taken from [?]

1.2 Lead Chalcongenide quantum dots

The QDs studied in this work are composed of Lead Selenide (PbSe). Lead salts materials such as PbSe or PbS (Lead Sulfide) are mostly known for being among the oldest and most common materials in the fabrication of infrared detectors. Atoms in PbSe are arranged with a rock salt crystal structure where the lead and the selenide ions form two separate face-centered cubic lattice interpenetrating each other. These two lattices are separated by half a lattice parameter. The lattice parameter being 6.12 Angstrom $\mathring{A}$. [?].

PbSe is mainly known to have unique electronic structure. The fundamental gap of this material occurs at the L-point of the Brillouin zone. Because there is four L-points in a Brillouin zone, the first valence and conduction states are fourfold degenerate [?, ?]. In PbSe QDs,the addition of a twofold spin degeneracy leads to an eight fold degeneracy of the quantum states [?, ?, ?]. The high dielectric constant ($\epsilon = 227$) and the small electron and hole effective masses at the L-point of the Brillouin zone ($m_h^* \sim m_e^* \simeq 0.16$ [?]) creates an exciton Bohr radius of 46 nm [?] (compared to 20 nm for PbS). This large exciton Bohr radius allows for the tuning of the
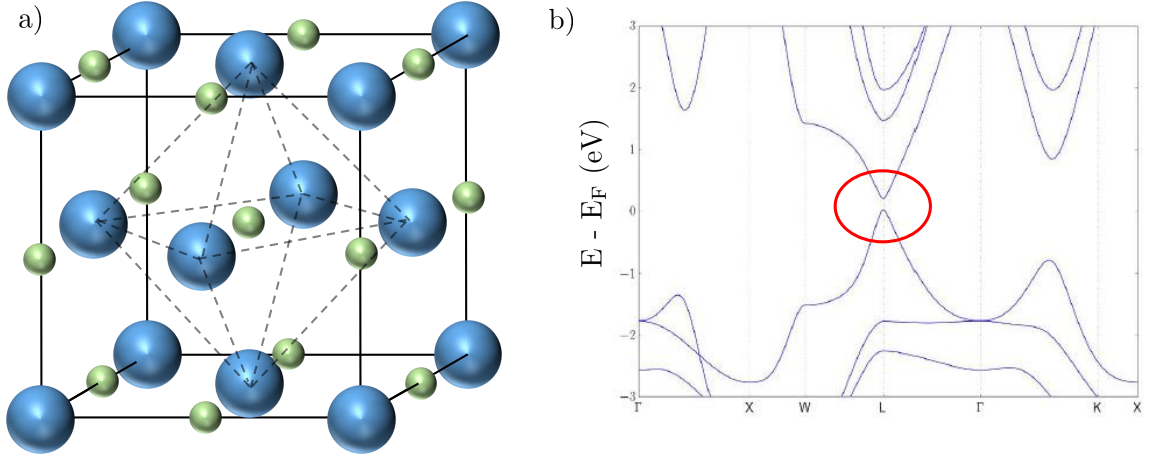
Figure 1.5: a) The rock salt structure of PbSe. Each atom has six nearest neighbors with octahedral geometry.b) Band structure of bulk PbSe. The bandgap is located at the L-point of the Brillouin zone. Figure taken from [?]

bandgap and absorption edge across the near-infrared to the visible spectrum [?]. Therefore quantum confinement effect is strongly pronounced in PbSe QDs. Bulk PbSe exhibits a narrow band gap of $\simeq$ 0.26-0.29 eV at 300 K and 0.16 eV at 4K [?, ?]. Due to quantum confinement effects, the gap can increase to values between 0.35 eV and 1 eV for QDs with diameter of 17 nm and 3 nm, respectively [?, ?], covering the whole short-wave infrared region. The analytic relation between the energy gap (in eV) and effective diameter D (in nanometer) of PbSe QDs is given by [?] :

$$E_{\text{gap}}(D) = E_{\text{gap}}(\infty) + \frac{1}{0.0105 \times D^2 + 0.2655 \times D + 0.0667} \tag{1.3}$$

where $E_{\text{gap}}(\infty)$ is the bulk band gap. Equation ?? shows a size dependence in $1/D$ because the coefficient of D^2 is small.

1.3 Quantum mechanical coupling and QD arrays

As discussed above, the QDs belong to the strong confinement regime due to their small size. Although electrons are spatially confined and localized within the QD, when two QDs are brought close to each other, their electronic wavefunction can overlap leading to delocalization of the latter over the entire structure. When the orbitals of two QDs overlap and have the same sign, their wavefunction constructively interferes and gives rise to a bonding orbital :

$$\Psi = C_1 \Psi_1 + C_2 \Psi_2 \tag{1.4}$$

where C_1 and C_2 are the normalization constants and Ψ_1 and Ψ_2 are the wavefunctions of two QDs. The coefficients depend on the energy mismatch of the orbital of the QDs but for two identical QDs, $C_1 = C_2 = 1/\sqrt{2}$. If the two orbitals have opposite sign, $C_1 = -C_2$. This leads to destructive interference and the creation of an antibonding orbital. In such a system

the electron is delocalized over the whole structure leading to a reduction of the confinement effect. Putting it simply the electrons have more space and thus can occupied a larger volume. When many QDs are coupled together in a QD array, their electronic coupling leads to the formation of bands [**?**].
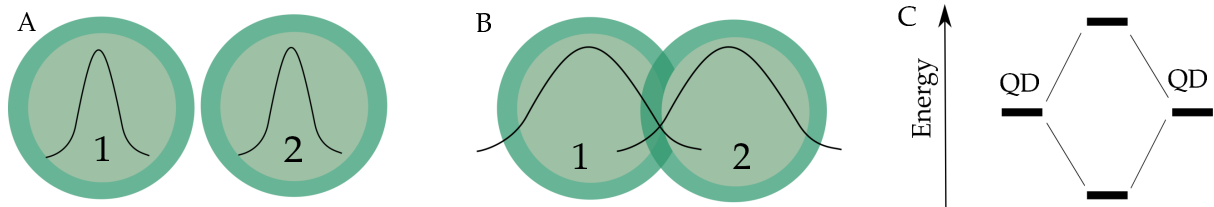
Figure 1.6: Illustration of the mechanical quantum coupling. Schematic representation of the ground state wavefunctions of two QDs: not coupled (A) and coupled with delocalization over the two QD(B). (C) Illustration of the hybridization when the electron wavefunction is delocalized over the QD dimer.

These QD solid thin films are of great interest for optoelectronic and charge transport applications. But their performances are limited by the nature, height and size of the energy barrier between two neighboring QDs. Thus the geometry of the QDs, the capping molecules, the distance between QDs and the disorder in the assembly of QDs can strongly interfere with the collective transport properties of a QD solid film.

In the case of PbSe, the large exciton Bohr radius lead to stronger confinement regime and more significant function overlap within the QD array. This should lead to stronger coupling between the QDs, which is favorable for a better transport of the carrier across the device.

1.4 Synthesis of colloidal quantum dots

Colloidal QDs are composed of two mains parts. The first is an inorganic core that confers to the QD its optical and electronic properties and on which it will be possible to tune and adjust these properties. It can be made of a single material or a combination of two or more materials just like PbSe. The second part are the surfactants molecules, often called ligands. They are amphiphilic organic molecules and are composed of a polar head and of a non polar part. The polar head, the binding group, can attach the undercoordinated surface atom. The non polar part consists in a long alkyl chain. Ligands are an important aspect of the colloidal QD [**?**] as they are used to control the QD growth during the synthesis. Ligands are important to keep the QDs stabilized in the solution preventing the aggregation and are also used to passivate the surface of the QDs. In the case of PbSe QDs, typical ligands are oleic acid ($C_{18}H_{34}O_2$) and oleylamine ($C_{18}H_{35}NH_2$).
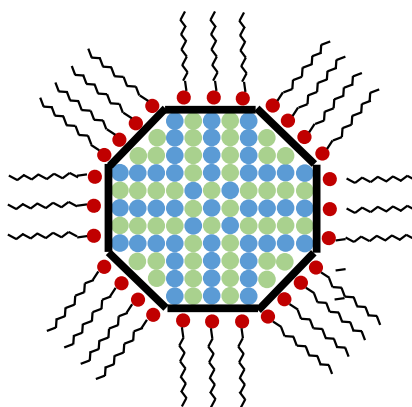
Figure 1.7: Schematic representation of a colloidal QD showing the crystalline and multifaceted nature of the inorganic core. The monolayer of amphiphilic organic molecules (the ligand shell) bound to the surface is also schematized.

1.4.1 Colloidal nanocrystal synthesis

Synthesis of colloidal QDs allows chemists to create nanometric crystals while precisely controlling their size and shape. The QDs exhibit very few defects which is an asset for avoiding non radiative recombination processes. In order to benefit from the quantum confinement effect in QDs a meticulous, controllable procedure that can be stopped when the desired dimensions are reached is required.

Colloidal QDs are fabricated by injecting precursors containing metal and chalcogendide (usually inorganic salt or organometallic compounds) at high temperature and high concentration within a high boiling point solvent containing coordinating ligands. The organic ligands are used to mediate the QD growth and stabilize it in the colloidal dispersion. Following the injection, the precursors decompose in the solvent resulting in a high concentration of metal and chalcogenide ions over a short period of time. This leads to the nucleation event and the latter the growth of the nuclei. Two approaches are possible to achieve such chemical reaction. In the first method, named 'hot injection', one of the precursors is rapidly injected in a hot apolar solvent (from 100°C to 300°C) already containing the other precursors [?, ?]. Subsequently, a quick and sudden increase in the total precursor concentration is observed. The second process is the 'heating-up' method. Every components of the reaction are loaded in a single flask and the temperature is quickly increased. This is done in order to realize a sudden nucleation [?, ?]. PbSe QDs are synthesized by rapidly injecting lead oleate and trioctylphosphine selenide (TOPSe) dissolved in trioctylphosphine into diphenylether solvent at 150°C. The reaction temperature is adjusted in the range of 90-220°C to obtain different sizes of PbSe QD [?].

The method develop in 1993 by Bawendi *et al* [?] was based upon the work of LaMer and

Dinegar in 1950 about colloid formation [**?**]. They reported a method for the synthesis of nanoparticles of CdSe based on the high-temperature nucleation and growth of nanoparticles from organometallic precursors. The synthesis of monodisperse QDs is achieved by separating the nucleation and the growth stages of the formation of the QDs. In the LaMer model three different regimes can be observed (see Figure **??**) :

Induction regime : The first regime, the induction of the reaction, starts with the injection of precursors and ends when small nuclei are formed. Monomers are formed thanks to the addition of precursors. When the concentration of these monomers starts increasing, small but unstable atomic clusters start to form.

Nucleation regime : The second regime corresponds to the nucleation period during which the nuclei become large enough to grow rather than redissolve into the solvent. This happens above a certain radius r_c corresponding to the critical QD radius. This is the radius at which the probabilities of growth and dissolution become equal (see Fig.**??**b). The nucleation stage is thus the time period where a single step nucleation event occurs. The nuclei only reach the critical radius r_c at a critical concentration of monomer c_c, where the solution is supersaturated. This supersaturation is the crucial parameter and can be obtained by the sudden increase of monomers, by rapidly injecting precursors at high temperature.
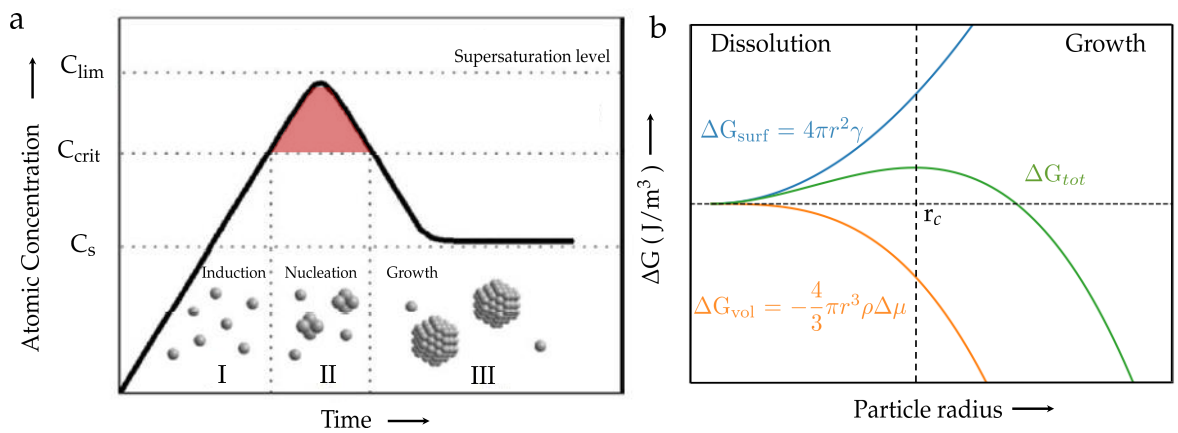
Figure 1.8: (a) La Mer diagram representing the stages of the QD nucleation and growth: The induction or generation of atoms regime (stage I), the self-nucleation regime (stage II) and the growth regime (stage III) . The red area in the curve show the range where the supersaturated solution has a concentration higher than the critical concentration C_{max}. This is where the growth of the dot is favored over dissolution. Figure taken from [**?**]. (b) Evolution of the Gibbs free energy during the formation of the nuclei. The critical radius r_c is the threshold below which the QD redissolve. Above this radius the QD grows in solution. This critical radius originates from the balance between the surface ΔG_s and volume energies ΔG_v.

Growth regime : The last regime is the growth of the crystal nuclei via the addition of monomer units and aggregation of smaller clusters already formed. In general, the growth

regime is stopped before an equilibrium state is reached in order to prevent Ostwald ripening. Ostwald ripening corresponds to the growth of larger QDs at the expense of the smaller ones which tend to lead to a broadening of the size distribution. Therefore Ostwald ripening must be as short as possible to synthesized monodisperse solution of QDs.

The nucleation of the colloidal QD can be explained by the classical nucleation theory (CNT) developed by Becker and Döring. This model uses the fact that a thermodynamic system tends to minimize its Gibbs free energy. It describes the nucleation with two Gibbs energy terms, a volume and a surface term [?, ?, ?] :

$$\Delta G_{tot} = \Delta G_{vol} + \Delta G_{surf} = -\frac{4}{3}\pi r^3 \rho \Delta\mu + 4\pi r^2 \gamma \tag{1.5}$$

Where r is the crystal nucleus radius, ρ the density of the crystalline phase, γ the interfacial tension between the developing crystal and the supersaturated solution, and $\Delta\mu$ represents the chemical potential difference between the nuclei and the monomers in solution. Creating volume is energetically favorable because it decreases the system total free energy, hence the negative sign of ΔG_{vol}. ΔG_{surf} is positive because the surface atoms will not have saturated bonds. Because ΔG_{vol} and ΔG_{surf} have opposite sign and different dependence in size, ΔG_{tot} reaches a maximum when the nuclei reaches the critical radius.
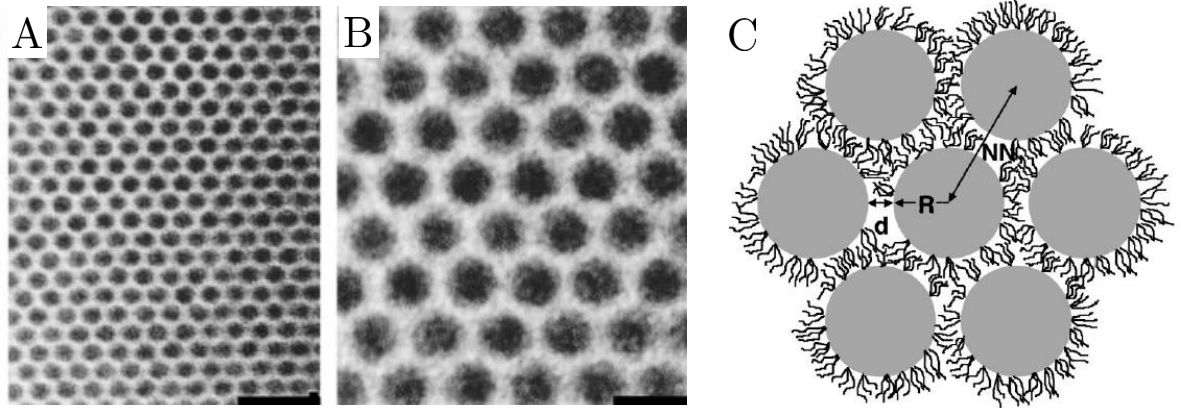
Figure 1.9: Monolayer of 4,8 nm CdSe dots at (A) low magnification (scale bar = 20 nm) and at (B) higher magnification (scale bar = 8 nm). The space between the dots is due to the presence of the native ligands. (C) Schematic representation of the local arrangement of the QDs ordered in an array with ligands in between them. **R** stands for the radius of the QD, **N − N** for the nearest neighbor distance and **d** is the inter-particle separation between dots in the solid. Figure taken and adapted from [?].

1.5 Array of coupled nanocrystals

Aside from their individual electronic and optical properties, the colloidal QDs have been used to create 2D and 3D self-assembled superlattices in a bottom-up approach. QD solids can be divided in two categories : (1) QD arrays consisting of individual QDs with an inorganic core

plus an organic surrounding, but without direct contact between the neighboring QDs and (2) high ordered QD superlattice where the QDs are directly connected through atomic bridges, called neck.

1.5.1 Self-assembly of quantum dots with inorganic capping

In the first class of QDs solid, each particle is stabilized in the matrix thanks to the use of surface ligands (see Figure **??**). The organic core allows for precise tuning of the discrete electronic states by adjusting precisely the size of the QDs. This size dependence originates from the strength of the quantum confinement. The ligands capping the core are used to control the growth during synthesis, passivate the surface dangling bonds and stabilize the QDs into the array. As mentioned above, one of the first synthesis of single-component self-assembly was reported on CdSe dots by Murray *et al.* [**?**] in 1995.
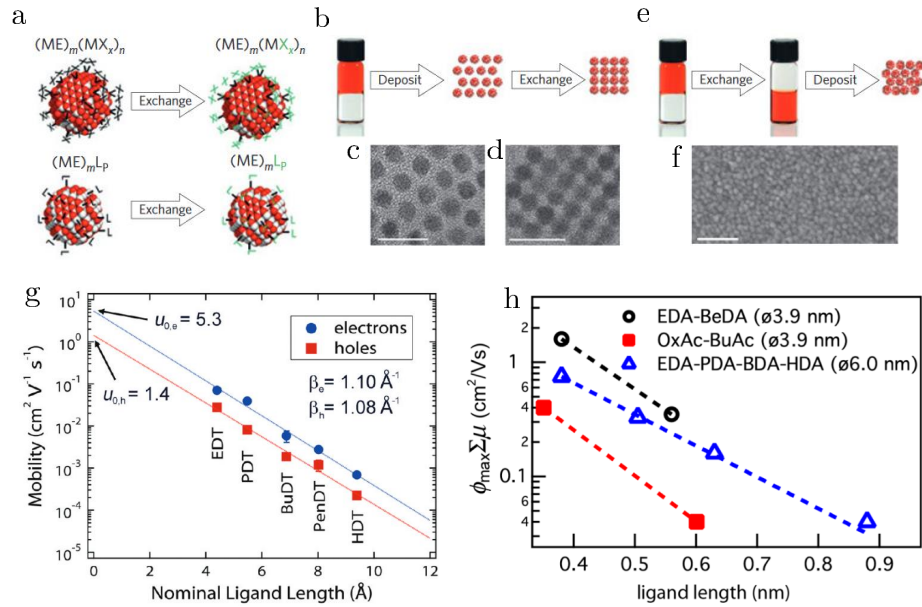
Figure 1.10: a) Schematic representation of X- and L-type ligands and their exchange for ligands of the same type. b, e) Schematic of solid-state ligand exhange (b) and solution-phase ligand exchange (e). c, d) TEM images of 6 nm PbSe QD films before (c) and after (d) solid-state exchange of long-chain oleate for compact, thiocyanate ligands. Scale bars, 20 nm. f) SEM image of solution-deposited, thiocyanate-exchanged 3.9 nm CdSe QD films. Scale bar,50 nm. Figures taken and adapted from [**?**]. g) Carrier mobility as function of ligand size in ambipolar PbSe (6.1 nm) QD field-effect transistors. Extracted from [**?**]. d) Effect of the various ligand size on the carrier mobility length of a 3.9 nm PbSe QD solid. Extracted from [**?**]

Unfortunately, the long organic ligands have quickly been problematic for charge transport applications. Because of their length and insulating behavior, the long ligands introduce large interdot distance and prevent strong electronic coupling between the neighboring QDs. Instead the carriers are forced to move trough interdot tunneling across the film. The transport

behavior of these materials is well described by variable range hopping [?]. As a result, very low mobilities have been reported (from 10^{-12} to 10^{-4} cm^2/(Vs)) [?, ?, ?].

In order to tackle this problem, chemical methods have been introduced to exchange the long native ligand with shorter organic [?, ?, ?, ?] and inorganic ligands [?]. The typical ligands exchange takes place when the native ligands are replaced by shorter ligands with head group providing the same type of binding (see Fig. ??a). The ligand exchange can be performed by a 'solid exchange' technique. It starts with the deposition of the QDs on a substrate in order to form a QD solid. Then the substrate with the QD film is immersed in a new solution where the exchange happens (Fig ?? b). A second method, called the 'solution exchange' consists in exchanging the long native ligands with more compact ligands in solution (Fig ?? e). This allows the deposition of dense and close-packed QD assemblies. The large area coating enabled by the 'solution exchange' process is of great interest for the integration in solution-deposited QDs devices.

The effect of the decreasing ligand size on the mobility in QD film is shown in Fig ?? (g) where an increase in the mobility over three decades (from 10^{-4} to 10^{-1} cm^2/(Vs)) is observed for PbSe QD based-FET. Similarly, Fig ?? (h) shows the increase in mobility over 2 decades for similar devices using the time resolved microwave conductivity technique (TRMC). The highest mobility is peaked at 2 cm^2/(Vs). Unfortunately the ligand volume lost in the 'solid exchange' can compromise the order of the QD film and often causes the formation of voids and cracks [?, ?]. The 'solution exchange' process damages the geometry of the self-assembly leading to a lack of long range order in these samples [?], as shown in Fig.?? f. Thus, band formation only happens when the coupling energy overcomes the energetic and translational inherent disorder of these systems. The decreasing ligand size coupled with the doping of colloidal QDs used to control the carrier statistics and Fermi energy in a semiconductor has led to significant increase in the devices performances. But in contrast with bulk semiconductor, doping in colloidal semiconductor QDs is rather complicated due to the difficulty to incorporate foreign atoms of different size inside the QD small volume. These difficulties are often attributed to 'self-purification', an intrinsic mechanism whereby impurities are expelled from the QDs [?, ?].

Throughout the years many studies on group III-V, II-VI, IV-VI semiconductors have been reported using different types of ligands and processes, in order to increase the mobility in QD film. Examples of the highest mobilities reported in the litterature on self-assembled QD solids prepared with organic ligands are listed in Table 1.1. While most studies report mobilities in the range ~ 0.1 cm^2/(V.s), the best examples of chemical engineering of the exchange ligand process and doping of QDs have increased the mobilities up to 5 - 27 cm^2/(V.s). An exceptionally high mobility, over 400 cm^2/(V.s) has been reported by the Talapin group upon sintering colloidal CdSe QDs. Achieving such mobilities approaching the bulk mobilities makes QD solid film viable for optoelectronics applications.

Material	Treatment	QD diameter (nm)	mobility (cm^2 V^{-1} s^{-1})	measurement technique	Ref.
InP	$Sn_2S_6^{4-}$, 350°C RTA	3.8	$\mu_n = 0.09$	FET	[?]
InAs	$Cu_7S_4^{-}$, 350°C RTA	4.5	$\mu_n = 16$	FET	[?]
	$Sn_2S_6^{4-}$, 350°C RTA	4.5	$\mu_n = 3.96$	FET	[?]
InSb	S^{2-}	4.5	$\mu_n = 1.5 \times 10^{-4}$	FET	[?]
			$\mu_p = 6.0 \times 10^{-4}$		
CdSe	$In_2Se_4^{-2}$, 200°C anneal	3.9	$\mu_n = 16$	FET	[?]
	SCN, In-doped, 250°C anneal	3.9	$\mu_n = 27$	FET	[?]
	$[Cd_2Se_3]^{2-}$, 350°C anneal	4.7	$\mu_n = 400$	FET	[?, ?]
PbS	N_2H_4	8.5	$\mu_n = 0.1$	FET	[?]
	$CH_3NH_3I + PN_2I$	3	$\mu_n = 0.1$	FET	[?]
	SCN, 150°C anneal	6.3	$\mu_n = 0.33$	FET	[?]
			$\mu_p = 0.13$		
PbSe	N_2H_4	9.2	$\mu_n = 0.95$	FET	[?]
	N_2H_4	5.7	$\mu_n = 29.4$	THz	[?]
	NaOH	5.7	$\mu_n = 35$	THz	[?]
	2DA	5.7	$\mu_n = 47$	THz	[?]
	SCN^{-}, Pb-doped	6	$\mu_n = 10$	FET	[?]
	SCN^{-}, Se-doped	6	$\mu_p = 0.5$	FET	[?]
	S^{2-}, $PbCl_2$	6	$\mu_n = 7$	FET	[?]
	S^{2-}, ALD Al_2O_3 75°C	6.3	$\mu_n = 7$	FET	[?]
	Na_2Se, $PbCl_2$	6.5	$\mu_n = 4.5$	FET	[?]
PbTe	NH_4SCN	3.9	$\mu_n = 2.8$	Hal	[?]

Table 1.1: Electron or hole mobilities reported in thin films of semiconductor QDs measured with different techniques. Field-effect transistor (FET) measurements (FET), terahertz spectroscopy (THz) measurements and Hall measurements (Hal).

1.5.2 Epitaxially connected quantum dot superlattices

Formation of the network

The intense research on overcoming the limitations stated above have mainly focused on exchanging the native ligands with shorter organic or inorganic substitutive ligands. These approaches, described in the previous section, also led to the discovery of new methods for the creation of QD superlattices where each QD is epitaxially connected through covalent bonds.

The synthesis of epitaxially connected QDs in a superlattice with long range order has the potential to improve the device performances drastically. Moreover, theoretical investigations including atomic thigh binding calculation, have predicted the appearance of electronic mini-bands with unique structures, including a Dirac cone and topological gaps in the case of a honeycomb shaped superlattice [**?**, **?**, **?**, **?**]. The synthesis of this new class of materials has been pioneered by the group of D.Vanmaekelbergh with PbSe QD superlattices consisting of the square or honeycomb geometry [**?**, **?**].
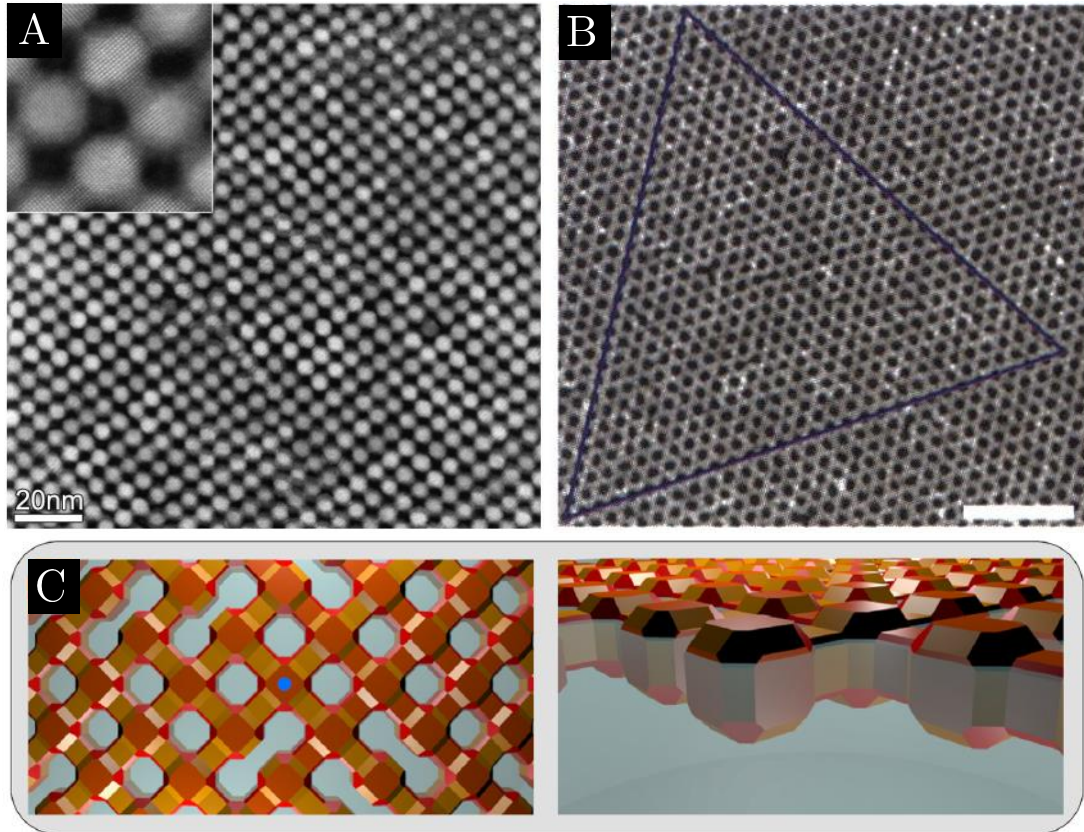
Figure 1.11: High angle annular dark field scanning electron transmission (HAADF-STEM) image of the square (A) and (B) honeycomb structure. The equilateral triangle shows the long-range ordering of the structure. Scale bar is 50 nm. Figure taken from [**?**, **?**]. Square lattice based on the 2D self-assembly of colloidal semiconductor QDs. Figure taken and adapted from [**?**].

In order to synthesize such highly ordered 2D superlattices, a dispersion of QDs in a non-polar solvent (usually toluene) is dropcasted onto a surface of an immiscible liquid, ethylene glycol in this case. Then the toluene is evaporated in a nitrogen purged glovebox. During this evaporation, the QDs concentrate over time and a mono-layer of a square lattice (visible in Figure **??**) is formed at the air-liquid interface. The detachment of the capping molecules from specific facets (here the {100} facets) and their dissolution in ethylene glycol drives the crystal attachment. This structure can later be transformed into 2D CdSe lattices through cation-

exchange that keeps the whole geometry intact [?]. A few other studies have managed epitaxial connection of QDs through other chemical processes. Both for PbS and CdSe QDs, initially separate QDs were successfully connected together after exposure to ammonium sulfide [?]. Similarly, epitaxially connected patch of PbS QDs with square geometry were fabricated by treating thin films of QDs using dimethylformamide [?]. Unfortunately, the resulting arrays only showed very local connectivity and lacked of long range order or did not yield dense superlattices. But recently new chemical process involving injection of sodium sulfide or amine based groups such as aniline have been able to trigger the epitaxial connection of PbSe and PbS QDs into a square superlattice with long range order [?].
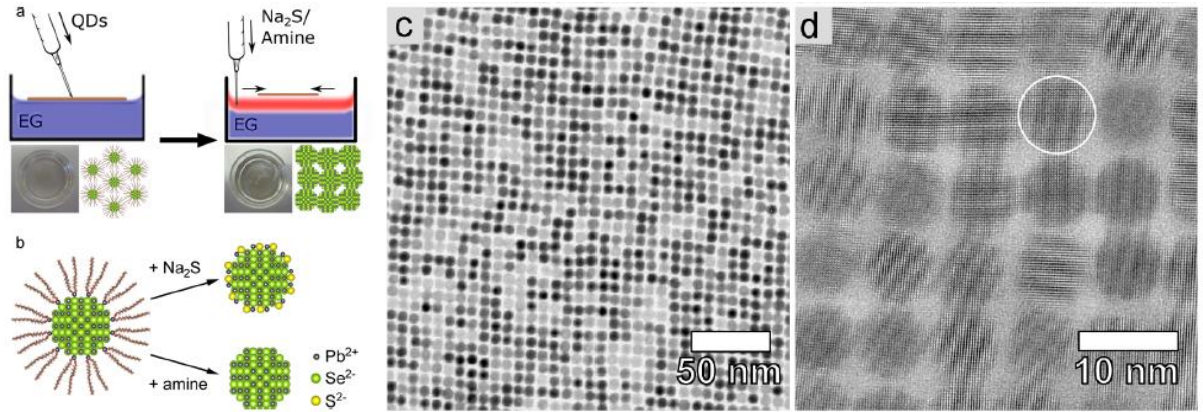
Figure 1.12: (a) A schematic representation of the experimental method used for the synthesis of QD superlattices. (b) Model showing two mechanisms to trigger the epitaxial connection of the QDs. (c) PbSe superlattices formed with aniline starting from 7.8 nm QDs with partial ligand shell. (d) HRTEM image showing the high degree of epitaxial connections. Figure taken and adapted from [?]

Predicted band structure of quantum dot superlattices

Due to the epitaxial connection of the QDs, a strong interdot coupling in this type of QD solid is expected. For example, band structure of a honeycomb CdSe superlattice predicted the existence of Dirac cones using atomistic tight binding method calculations [?]. The band structure of such graphene-type honeycomb lattice made of CdSe QDs is shown in Figure **??** (A,B) where (A) shows the conduction band and (B) the valence band. The associated theoretical model of the QD honeycomb structure with the QDs connected through their (110) facets is shown in Figure **??** (C). The conduction band is constituted of two envelops with two and six bands. At the K and K' points, two Dirac cones with a linear dispersion relation similar to the graphene band structure are predicted. Additionally, flat bands are predicted as a result of the absence of hybridization between the $1S$ and $1P$ states of the QDs under the effect of the strong quantum confinement. Similar features have been predicted in the case of HgTe QDs with the same honeycomb geometry [?].
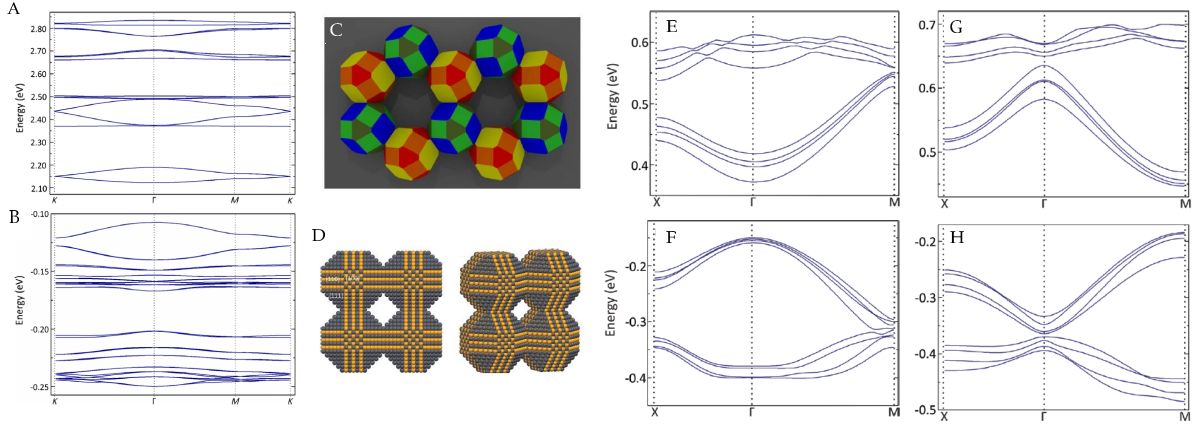
Figure 1.13: Theoretical calculations of the conduction (A) and valence (B) bands for a planar honeycomb structure composed of CdSe QDs. The calculations were made for a model where the QDs are fused following their (110) facets. Figures taken and adapted from [?]. Calculated conduction bands structures (E) and (G) and valence bands structures (F) and (H) for a PbSe square superlattice and for two different number n of {100} biplanes ((E) and (F) : even; (G) and (H) : odd) composing the neck between two fused QDs. The model for this square superlattice is shown in (D). Figures taken and adapted from [?].

In the case of square superlattices composed of QDs with atomically bonded facets, the theoretical calculations predict electronic bands structures composed of successive band [?]. This is due to the strong coupling between the wave functions of the nearest-neighbor QDs. In the case of PbSe superlattices, the position in k space of the conduction and valence band edges depends on whether the number of biplanes of atoms in the QDs is odd (Figure ?? (E) and (F)) or even (Figure ?? (G) and (H)).

The coupling of the wavefunction between QDs, and thus the width of the bands, strongly depends on the necking between QDs, i.e., the number of atoms at the QD bonding plane. This is illustrated in Figure ??. The square superlattices where modeled with 2D lattices of <001>-oriented CdSe QDs attached via perpendicular {100} facets. Each QD has the form of a truncated cube (see Figure ?? (D)) with a truncation factor q. In Figure ?? (a) and (d) the band structure for $q = 0$ (a homogeneous 2D film) is shown and compared with the corresponding electronic structure of a QD superlattice with q = 0.45 (Figure ?? (b) and (e)) as well as that of individual NCs with the same truncation (Figure ?? (c) and (f)). It is clear that the 2D film presents very dispersive bands (because carriers are free to move in two directions) in comparison to the truncated superlattice. In the latter case, the truncation creates an opening of the band gap induce by the periodic scattering of the electronic waves. Therefore, the band structures predicted by the theoretical calculations should lead to high charge carrier mobility in the epitaxially connected QDs superlattices.
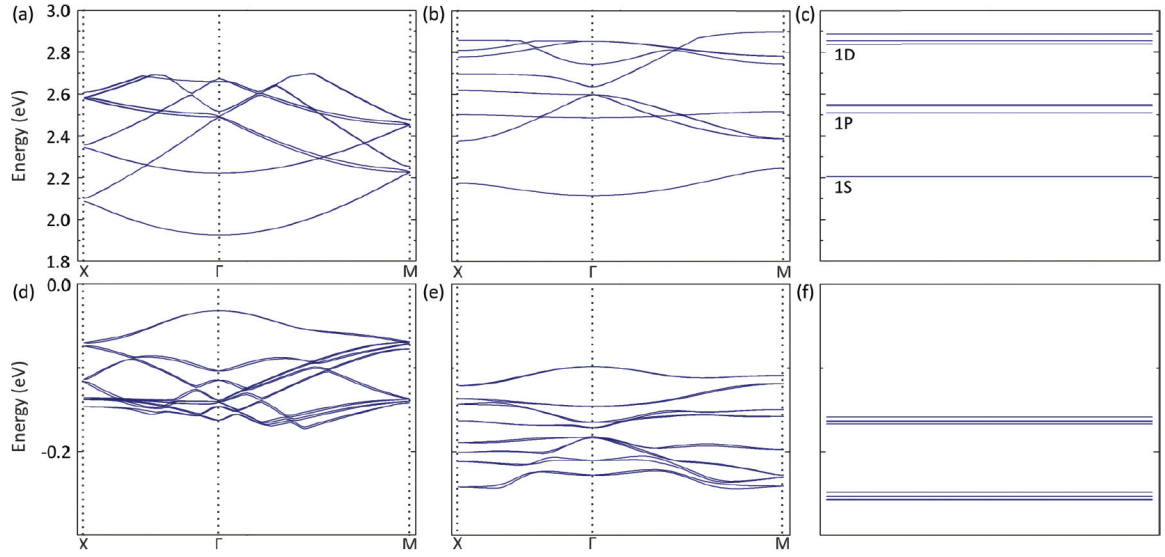
Figure 1.14: (a) Conduction and (d) valence band for uniform 2D (zero truncation) film composed of CdSe QDs. (b) and (e) : Similar plots for a 2D superlattice composed of truncated CdSe QDs ($q = 0.45$) and for an isolated truncated ($q = 0.45$) CdSe QD ((c) and (f)). Figures taken and adapted from [?].

Transport properties

Balazs *et al* synthesized PbSe superlattices following the method described above but performed ligands exchange using ethanedithiol (EDT) and ethylenediamine (EDA) [?]. Following this treatment, the samples were characterized with ion-gel-gated-field-effect transistors (IGFETs). The EDA treated samples exhibited stronger necking between the QDs yielding an average two-terminal electron mobility of $13\,\mathrm{cm}^2/(\mathrm{V.s})$ and contactless mobility of $24\,\mathrm{cm}^2/(\mathrm{V.s})$. The average mobility value is consistent with the DC mobility measured by Evers *et al* [?] on similar PbSe superlattice (but without ligand exchange). In this case, multi-probe scanning tunneling microscopy was used to determine the mobility of the 2D PbSe network. The tips were set in a square configuration with a tip separation of 500nm. A mobility of 12 or 3 $\mathrm{cm}^2/(\mathrm{V.s})$ was found depending on the direction of the electron flow with respect to the crack inside the network. By contrast, Terahertz spectroscopy techniques lead to much higher mobilities (around 260 $\mathrm{cm}^2/(\mathrm{V.s})$) than standard DC techniques on the very same sample. This striking difference lays in the size of the area probed by the different techniques: 500 nm for DC techniques and less than 50 nm for THz spectroscopy. These results suggest the presence of long-range disorder that strongly affect the coupling between QDs, thereby the mobility of the charge carrier. Alimoradi Jazi *et al.* used liquid electrolyte gating to study the injection of carriers. Hall bars were fabricated enabling the study of four-probe conductance. Out of these experiments over 13 devices, a mean mobility of 3.8 $\mathrm{cm}^2/(\mathrm{V.s})$ with a maximum mobility of 18 $\mathrm{cm}^2/(\mathrm{V.s})$ was measured [?]. A similar low mobility of 1.5 $\mathrm{cm}^2/(\mathrm{V.s})$ was measured by the same group using the same liquid electrolyte gating on a 2D PbSe superlattice with a honeycomb structure [?]. Surprisingly, low mobility values were also reported on similar superlattices de-

spite the strong fusion of the QDs facets and the high order of the array. Whitham *et al* reported mobilities of 0.54 cm^2/(V.s) for holes and 0.2 cm^2/(V.s) for electron [?] and Walravens *et al* reported hole mobility of 1.9×10^{-2} cm^2/(V.s) [?]. A summary of the different mobilities found in the literature is listed in Table 1.2.

Geometry	QD diameter (nm)	mobility (cm^2 V^{-1} s^{-1})	measurement technique	Ref.
Square	5.2	$\mu_n = 13$ (avg) - 24(best)	FET	[?]
Square	5.8	$\mu_n = 2 - 13$	Multi tips STM	[?]
Square	5.8	$\mu_n = 260$	THz	[?]
Square	5.5	$\mu_n = 3.8$ (avg) - 18(best)	EGT	[?]
Square	6.5	$\mu_n = 0.2$	FET	[?]
Square	6	$\mu_n = 1.9 \times 10^{-2}$	FET	[?]
Square	5.5	$\mu_n = 2.6$	TRMC	[?]
Square	6.5	$\mu_n = 2.6$	FET	[?]
Square	6.5	$\mu_n = 2.6$	FET	[?]
Honeycomb	6.15	$\mu_n = 1.5$	EGT	[?]
Honeycomb	6.15	$\mu_n = 1.5$	THz	[?]

Table 1.2: Electron or hole mobilities measured in two-dimensional QD superlattices. FET, field-effect transistor measurements; THz, terahertz spectroscopy measurements; EGT, Electrolyte gated transistor; TRMC, Time Resolved Microwave Conductivity

Disorder and defects in expitaxial superlattices

Despite their epitaxial connection which should drastically increase the interdots coupling and their high degree of order, the epitaxial superlattices have yet to surpass the charge transport properties of the self-assembly QD solid prepared with organic ligands. In addition, the predicted band-like transport and other Dirac point (in the case of the honeycomb structure) have not been observed. Indeed, the epitaxial connection usually generates crystal defects that reduce atomic lattice coherence. Whitham *et al* attributed the poor transport properties to different sources of disorder such as dispersion in size, coupling energy disorder (due to the variation of the connection width) and missing connections [?]. The combined effect of all these sources of disorder have a deleterious influence on the transport properties. A small defect concentration restricts the localization length to less than 10 nm [?].
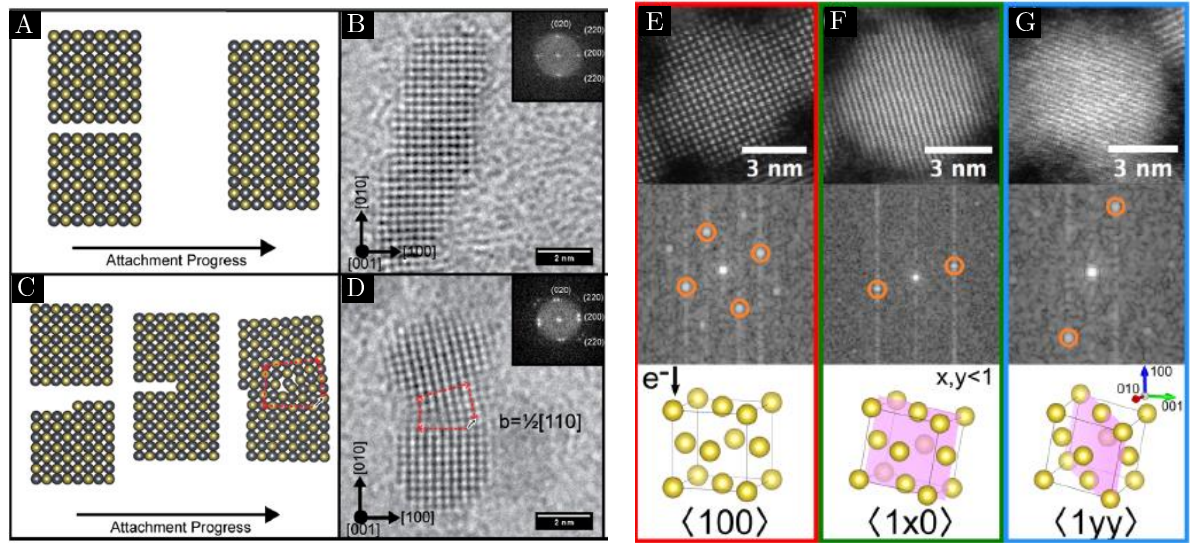
Figure 1.15: (A) Schematic representation of the process leading to perfect attachment of PbTe nanocrystals on (100) facets and (B) corresponding experimental HRTEM image and FFT of three PbTe nanocrystals with perfectly attached 100 facets. (C) Schematic representation of a step edge leading to an edge dislocation during the attachment of PbTe nanocrystals on (100) facets. (D) Experimental HRTEM image and corresponding FFT of PbTe nanocrystals imperfectly attached on (100) facets. Figure taken and adapted from [?]. Example of QDs (E) aligned in the out-of-plane direction, (F) rotated toward ⟨110⟩, or (G) rotated toward ⟨111⟩. Figure taken and adapted from [?]

Defects can arise during the QDs attachment like step edge leading to edge dislocation (see Figure **??** c-d), twin boundaries or stacking faults [?], even when the QDs have the same out of plane alignment. In PbSe superlattices the QDs are attached along the (100) facets. Thus it is expected that the ⟨100⟩ direction should be the predominant out of plane orientation. McCray *et al.* reported that only 28.1% (over 1823 particles) of the QDs had this out plane orientation (Figure **??** e) while 47.4% of the QDs were tilted toward the ⟨110⟩ direction (Figure **??** f) and 16.8% tilted over the ⟨111⟩ direction [?] (Figure **??** g). This rotational misorientation prevents the QDs to get perfectly aligned with their neighbors. While it has been reported that thermal treatment of the superlattice could arrange the interfacial state of the QDs connection by decreasing the density of points defects and edge dislocations, the associated mobilities after annealing were still low[?]. This indicates that other sources of disorder are still involved in the limitation of charge transport. These persistent defects are challenging to remove [?]. Moreover, surface traps states are known to arise in colloidal QDs due to the removal of ligands from the surface [?, ?, ?]. These undesirable states are usually strongly localized with an energy position deep inside the band gap (see Figure **??**). They are also responsible for the weak transport properties in the QDs solid film. Strategies to passivate the surface and eliminate such traps have shown to be efficient in increasing the performance of QDs based devices [?].
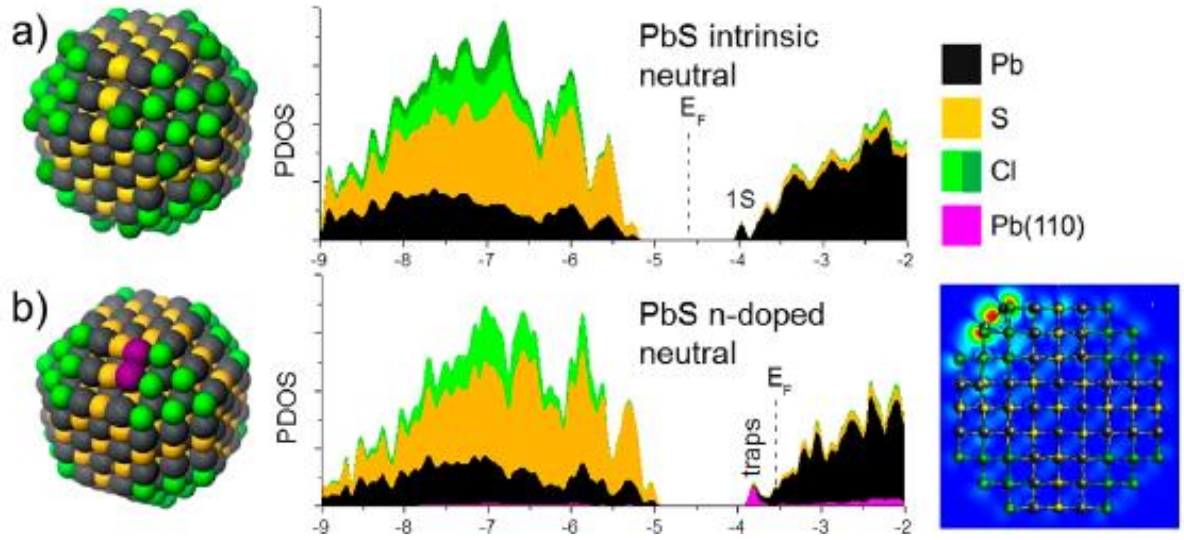
Figure 1.16: Structures of PbS QDs used in calculations with corresponding projected densities of states and spatial charge densities of the lowest energy state on the conduction band side: (a) electronically balanced dot, (b) doped dot due to removal of halide ligands from (110) facets (darkgreen) resulting in formation of Pb dimers (purple) and related localization of charge at its surface (right panel). Figure taken and adapted from [?].

1.6 Conclusion

The recent preparation of atomically connected QDs superlattices led to the elimination of any tunnelling barrier between adjacent QDs in QD solid thin film. Thanks to these atomic necking, these QD films were expected to yield high mobility and band-like charge transport. Unfortunately, charge transport experiments have reported poor transport properties with mobilities lower than expected. Therefore, new insights into structural and electronic structure in QD thin films through careful experimental investigations are needed to understand this surprisingly low transport properties. While structural disorder has been investigated to explain the low transport properties, the electronic structure of the superlattice still lacks of experimental studies. Optical spectroscopy techniques (such as absorption or photoluminescence spectroscopy) may bring information in this regard but has limitation as it does not investigate separately electron and hole but involves transitions between two states. On the other hand, scanning tunneling spectroscopy (STS) is not affected by this limitation and has showed to be a viable tool to probe individual energy levels of semiconductors colloidal QDs [?, ?, ?]. Moreover, STS offers two other unique aspects. It allows to first access information about the topographic structure of the film. Thus, it enables interesting correlation between the physical characteristics of the QD and its structure. Second, STS is able to measure the electronic structure of an individual QD and not average values coming from an ensemble of QDs, which is crucial to investigation electronic properties of QD array. By bringing information on the density of states of a material on a local scale STS is a suitable technique to provide unique

information on the electronic properties of the epitaxial superlattice. In this work, STS was used to investigate PbSe QDs superlattice. Also, we tried to correlate the electronic structure of individual QDs to the electronic structure of QD superlattices.

Chapter 2

Experimental Techniques

2.1 Scanning Tunneling Microscopy

2.1.1 Introduction

In the past forty years, science and technology has turned toward the production, investigation and manipulation of smaller and smaller objects. Unfortunately, optical microscopy is limited due to the diffraction limits of optical wavelengths. Therefore scientists had to develop new techniques relying on other particles than photons to improve or surpass the maximum resolution achievable by optical microscopes. It is this motivation that leads to the invention of the Scanning Tunneling Microscopy (STM) [**?**, **?**]. Initially developed in 1981 at the IBM Zurich Research Laboratories in Switzerland by Gerd Binnig and Heinrich Roher, the STM is a powerful experimental method used for the investigation and characterization of conductive surfaces (thus metal and semiconductor) with sub-nanometer resolution. Due to the incredible breakthrough this invention has been for the scientific community, his inventors, Roher and Binnig, were rewarded with a Nobel Prize in 1986 [**?**].

The next section will be dedicated to the study of each aspect of the working principle of a STM, starting with the theoretical basis of the Tunnel Effect. Then the basis of the operation of the STM will be developed to explain the atomic resolution.

2.1.2 The rectangular potential barrier and the transmission coefficient

The tunnel effect is a pure quantum effect in which a particle of energy E gains the ability to cross a thin potential barrier of higher energy ($\Phi_0 > E$), which would normally be impossible according to classical physics. This counterintuitive effect originates directly from the wave-particle duality, another fundamental quantum concept.

Figure **??** represents a schematic vision of a potential barrier in one dimension. Two metallic electrodes are separated by a vacuum region. The potential barrier is characterized by its width d and its height Φ_0. Φ_0 depends on the work functions of both electrodes, which will
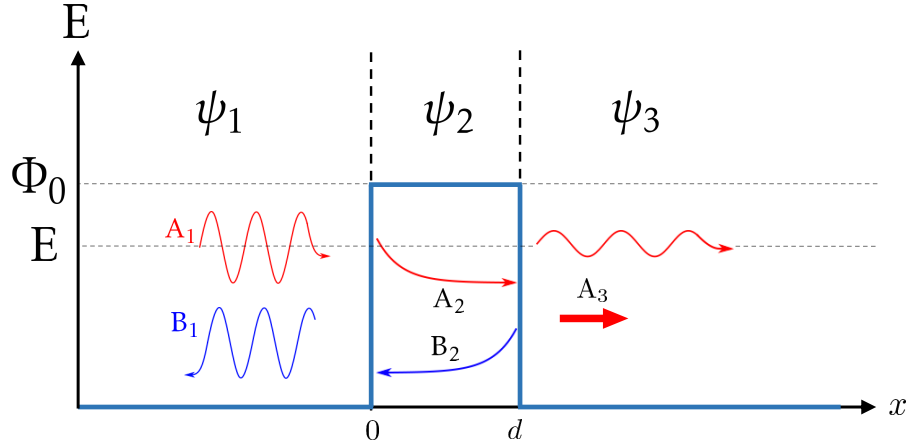
Figure 2.1: Schematic view of a 1D tunnel barrier along the axis x. An incident electronic plane wave of amplitude A_1 and energy E moves toward the barrier. A part of this initial wave is transmitted at the first interface (A_2) while the other part is reflected (B_1). This transmitted wave is again partially reflected (B_2). The transmitted part of A_2 finally reach the other side of the tunnel barrier (A_3).

be assumed equal here. An electron of mass m and of energy $E < \Phi_0$, possesses different wave functions ψ_i (i = 1,2,3) for each region of space (see Figure **??**). These wave functions are all solutions of the time-independent Schrödinger equation :

$$H\psi(x) = \left[\frac{-\hbar^2}{2m}\frac{\partial^2}{\partial x^2} + V(x)\right]\psi(x) = E\psi(x) \tag{2.1}$$

Where H is the Hamiltonian, $\hbar = \dfrac{h}{2\pi}$ is the reduced Planck constant, m and E the mass and the energy of the particle respectively. The first term of the Hamiltonian corresponds to the kinetic energy and the second term, $V(x)$, is the potential variation along the x axis. $V(x)$ can be represented as a Heaviside step function where $V(x) = 0$ for $x < 0$ and $x > d$, and $V(x) = \Phi_0$ for $0 < x < d$. As the barrier divides the space into three parts, the eq.**??** change for each of region :

$$\begin{aligned}
\frac{-\hbar^2}{2m}\frac{\partial^2\psi_1}{\partial x^2} &= E\psi_1 & x < 0 \\
\frac{-\hbar^2}{2m}\frac{\partial^2\psi_2}{\partial x^2} + \Phi_0\psi_2 &= E\psi_2 & 0 < x < d \\
\frac{-\hbar^2}{2m}\frac{\partial^2\psi_3}{\partial x^2} &= E\psi_3 & x > d
\end{aligned} \tag{2.2}$$

Therefore the general solutions of each of these equations are :

$$\begin{aligned}
\psi_1(x) &= A_1 e^{i\alpha x} + B_1 e^{-i\alpha x} & x < 0 \\
\psi_2(x) &= A_2 e^{kx} + B_2 e^{-kx} & 0 < x < d \\
\psi_3(x) &= A_3 e^{i\alpha x} & x > d
\end{aligned} \tag{2.3}$$

where A_i and B_i correspond here to the incident and reflected part in the different regions ($i = 1,2,3$) with the wave numbers $\alpha = \sqrt{\frac{2m}{\hbar^2}E}$ and $k = \sqrt{\frac{2m}{\hbar^2}(\Phi_0 - E)}$ because the energy of the particle is below the barrier height ($E < \Phi_0$).

Because each wave functions and their derivatives have to be continuous everywhere, we can deduce the coefficients A_i and B_i from the boundary conditions in $x = 0$ and $x = d$. Then we obtain a system of four equations :

$$A_1 + B_1 = A_2 + B_2 \qquad A_1 - B_1 = -\frac{ik}{\alpha}(A_2 - B_2)$$
$$A_2 e^{kd} + B_2 e^{-kd} = A_3 e^{i\alpha d} \quad A_2 e^{kd} - B_2 e^{-kd} = \frac{ik}{\alpha}A_3 e^{i\alpha d} \tag{2.4}$$

Resolving this system yield the probability $T(E)$, which is the probability for an electron to cross the barrier. $T(E)$ is given by the following expression :

$$T(E) = \left|\frac{A_3}{A_1}\right|^2 = \frac{1}{1 + \frac{\Phi_0^2}{4E(\Phi_0 - E)}\sinh^2(kd)} \tag{2.5}$$

From the above equation we can observe that $T(E)$ is never null, revealing that electrons always have a small probability to cross the barrier because of their wave–particle nature.
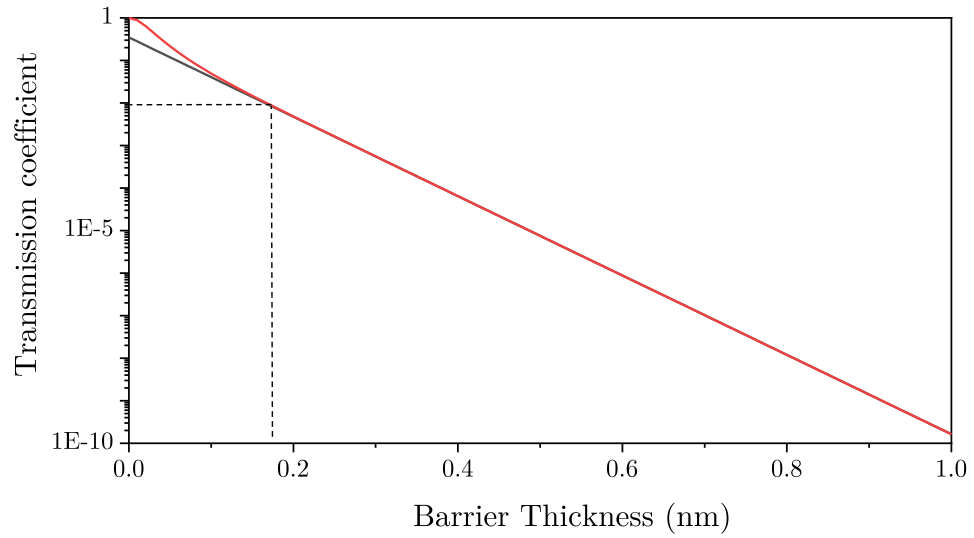
Figure 2.2: Plot of the Equation **??** (red curve) and the Equation **??** (black curve) representing the Transmission coefficient as function of the barrier thickness for an electron energy of 0.1 eV and $\Phi_0 = 4.5$ eV (work function of the tungsten).

Tungsten tips are often used as metallic electrodes in STM. Thus we consider a tungsten electrode with a work function $\Phi_0 = 4.5$ eV and an electron of energy $E = 0.1$ eV. Figure **??**

shows the evolution of $T(E)$ as function of the barrier thickness for these two parameters. From the grey dashed lines, it is clear that increasing the barrier thickness by 3 Å induces a drop in the transmission coefficient by almost three decades. Therefore, by considering a large barrier of a few angstroms and an electron of small energy ($kd \gg 1$), the function $\sinh^2$ dominates the expression $1/(1 + \sinh^2)$ and thus we can approximate $T(E)$ as :

$$T(E) \simeq \frac{16E(\Phi_0 - E)}{\Phi_0^2} e^{-2kd} \tag{2.6}$$

If the number of electrons tunneling from the right to the left is the same as the number of electrons flowing in the other direction, these two flows will compensate each other resulting in the absence of a measurable current. Therefore, the tunneling barrier needs to be polarized so that a current flows between the electrodes. In STM experiments the two electrodes used to apply bias are the tip and the substrate where the ground reference is usually the substrate. When a bias eV is applied across the junction, the barrier takes a trapezoidal form (see Fig.**??**). But if eV is small enough compared to the height of the barrier then we can make the approximation that the barrier is still a square (red dashed line in Fig.**??**) of height Φ :

$$\Phi = \frac{\Phi_{\text{tip}} + \Phi_{\text{sample}}}{2} - \frac{eV}{2} \tag{2.7}$$

where Φ_{tip} and Φ_{sample} are the work function of the tip and the sample, respectively.
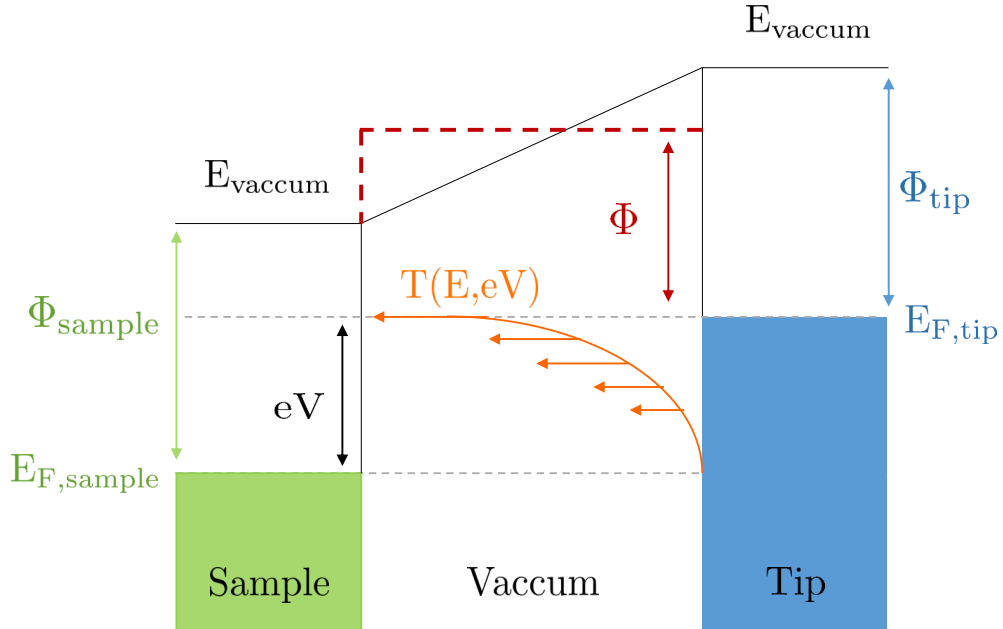
Figure 2.3: Schematic representation of a tunnel junction. When no bias is applied the barrier looks like a rectangle of height $\Phi = \frac{\Phi_{\text{sample}} + \Phi_{\text{Tip}}}{2}$, which is the mean value of the work functions of the electrodes. If a bias is applied then the barrier becomes trapezoidal. But if eV is small enough with respect to Φ, the barrier can be approximated as a rectangle (red dashed line).

Despite this change of the barrier height, the calculation of $T(E)$ is still valid. Therefore, the probability for an electron to cross the barrier becomes :

$$T(E,V,d) \simeq \frac{16(E-eV)(\Phi-(E-eV))}{\Phi^2} \exp\left(-2d\sqrt{\frac{2m}{\hbar^2}(\Phi-(E-eV))}\right) \qquad (2.8)$$

2.1.3 The tunnel current

The previous section discussed the tunnel effect and the calculation of the coefficient of transmission for an electron to cross a rectangular potential barrier when a bias is applied. Now an expression of the tunneling current is needed to be able to understand what information is obtained. In this section a general formula for elastic tunneling will be derived. The transmission rate from a state $|i\rangle$ to a final state $|f\rangle$ is given by the Fermi's Golden rule [?], written as :

$$W_{i\rightarrow f} = \frac{2\pi}{\hbar}\left|M_{fi}\right|^2 \delta(E_i - E_f) \qquad (2.9)$$

where M_{fi} is the transition matrix element between the two orbitals ψ_t and ψ_s in the tip and the sample, and where the term $\delta(E_i - E_f)$ only allows tunneling between electron level with the same energy, hence ensuring energy conservation. Thus by summing-up all the transition rates between the wavefunctions of the different energy levels one can write the current flowing from the tip to the sample and correspondingly from the sample to the tip as :

$$I_{t\rightarrow s} = \frac{2\pi e}{\hbar}\int_0^{\infty}\left|M_{ts}\right|^2 f_t(E-eV)[1-f_s(E)]\rho_t(E-eV)\rho_s(E)dE \qquad (2.10)$$

$$I_{s\rightarrow t} = \frac{2\pi e}{\hbar}\int_0^{\infty}\left|M_{ts}\right|^2 f_s(E)[1-f_t(E-eV)]\rho_t(E-eV)\rho_s(E)dE \qquad (2.11)$$

where $f(E)$ is the well-known Fermi-Dirac distribution and $\rho(E)$ is the density of states of either the tip or the sample. An electron of the tip in an occupied state (ρ_t, f_t) will be able to tunnel into an unoccupied state of the sample ($\rho_s, (1-f_s)$). Here the Fermi level of the sample is chosen as the reference, and therefore the tip Fermi level will be shifted by $\Delta E = eV$. The total current flowing between the sample and the tip can take the following expression :

$$I = I_{t\rightarrow s} - I_{s\rightarrow t} = \frac{2\pi e}{\hbar}\int_0^{\infty}\left|M_{ts}\right|^2\left[f_s(E)-f_t(E-eV)\right]\rho_t(E-eV)\rho_s(E)dE \qquad (2.12)$$

The Fermi-Dirac distribution is known to be a simple step function for temperature of T = 0K. By putting ourselves in the approximation of the low temperature (T = 0K) the above equation can be simplified to :

$$I(T = 0K) = \frac{2\pi e}{\hbar}\int_{E_{\mathrm{F}}}^{E_{\mathrm{F}}+eV}\left|M_{ts}\right|^2\rho_t(E-eV)\rho_s(E)dE \qquad (2.13)$$

The difficulty of the above equation is the calculation of the transition matrix element $\left|M_{ts}\right|^2$. In 1961, Bardeen [?] showed that this element could be determined by considering the

overlap of the surface wave functions of two subsystems, sample+vacuum and tip+vacuum and applying the time dependent perturbation theory to the system. The total separation of the tip and sample systems leads to two independent Schrodinger equations. The matrix is a surface integral of the wave functions (and its normal derivatives) of the sample and tip evaluated at the separation surface S and is given by :

$$M_{ts} = \frac{\hbar^2}{2m} \int (\psi_s^* \nabla \psi_t - \psi_t \nabla \psi_s^*) dS \tag{2.14}$$

In the case of a one dimensional rectangular barrier the matrix element $\left|M_{ts}\right|^2$ can be replaced by the transmission coefficient $T(E, V, d)$ from Equation **??** [**?**]. Then Equation **??** can be rewritten :

$$I = \frac{2\pi e}{\hbar} \int_{E_F}^{E_F + eV} T(E, V, d) \rho_t(E - eV) \rho_s(E) dE \tag{2.15}$$

As we have seen, the transmission coefficient is not a constant and depends on the applied bias voltage and the energy of the tunneling electrons. However, for small tunneling voltages eV in comparison of the mean height of the barrier Φ (see Figure **??**), the transmission coefficient $T(E, V, d)$ can be assumed constant in the energy range between E_F and $E_F + eV$. In this, approximation, the transmission factor $T(d)$ is independent of the energy E and the voltage V. Therefore, the tunneling current can be written as :

$$I = \frac{2\pi e}{\hbar} T(d) \int_{E_F}^{E_F + eV} \rho_t(E - eV) \rho_s(E) dE \tag{2.16}$$

Therefore the tunneling current is proportional, to the combined density of states of the tip and the sample at a given bias eV and the transmission coefficient at a certain distance d. Usually the tip density of states can be considered constant and put in front of the integral :

$$I \approx \frac{2\pi e}{\hbar} T(d) \rho_t(eV) \int_{E_F}^{E_F + eV} \rho_s(E) dE \tag{2.17}$$

When the density of states of the sample consists of discrete energy levels, as it is the case for QDs, the I(V) curves will show a succession of steps, each step corresponding to the transfer of electrons from the tip to a new energy level. Therefore, the tunneling current can provide a direct measurement of the density of states. Later, we will give more details about tunneling spectroscopy, which is associated with scanning tunneling microscopy.

2.2 The microscope

The STM is based on the tunnel effect, between two conductive electrodes. In the STM one electrode will be the substrate and the other one a sharp metallic tip used as a probe. This creates a tunneling junction as the one showed in Figure **??**. We will now discuss the microscope and its operating principle starting with lateral resolution.

2.2.1 The operating principles

Figure **??** illustrates a STM scanner and its associated electronic circuit allowing the operator to control the movement of the scanner. In inset, the representation of a tip scanning an atomic surface with a schematized electron flow is showed. The scanner allowing the tip to move freely and precisely in space is made of a piezo-electric material. Here the piezoelectric material is a ceramic of the PZT [**?**] (lead zirconate titanate) family as this material has a large piezoelectric constant. The piezoelectric material is arranged in a tube scanner where the electrodes are attached to the side of the tube, segmenting it in vertical quarters (+x, -x, +y, -y) while a last electrode is attached to the center of the tube to allow z motion (see Figure **??**). When an electric field is applied to the piezoelectric transducer, the transducer will expands or contract. These nanometric deformations will enable the tip to move laterally and vertically along the surface. This type of scanner allows to scan from a few angstroms to hundred of microns.
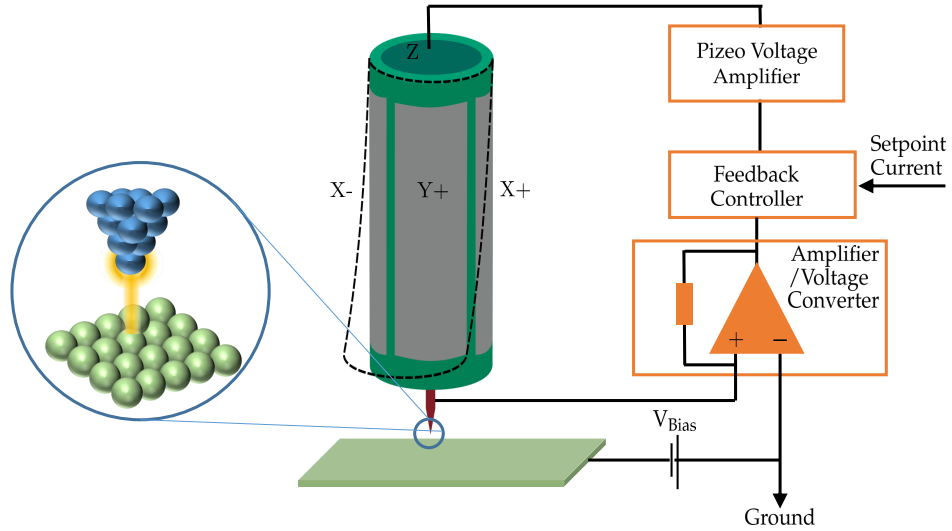
Figure 2.4: Sketch of the tunneling junction and the feedback controlling circuit in scanning tunneling microscopy. The tip is represented as atomically sharp and ideal conic shape. The piezoelectric tube is coupled to the tip and controlled by the electrical circuit. A voltage bias is applied between the tip and the sample and the resulting current is collected from the tip and amplified. After the current is compared in the feedback controller circuit, a voltage is applied to the piezo tube to change the tip-sample distance and to maintain a constant current.

The tip is mounted on the extremity of the piezo tube. The polarization of the tip is applied through the input V_{bias} with the sample as the ground electrode. If the tip is brought in proximity of the surface and moved laterally at a constant distance and a constant voltage then every morphological change in the surface will result in an increase/decrease between the tip and the surface. Therefore every change tip-sample distance will result in a change in the tunnel current. The detected tunnel current will be amplified by a current amplifier and converted into voltage (thank to a current-voltage converter). Thus the change in the current can produce a realistic image of the surface when transformed into height thanks to Eq.**??**. This mode is

called constant height mode. Unfortunately the sample is always slightly sloped with respect to the scanning plane of the tip, plus the surface is unknown and sudden and big changes of morphology can result in a crash of the tip.

Using a feedback system, allowing the operator to control the tip-to-sample distance, one can force the tip to retract when it is too close to the surface. In this case, the tunnel current is compared to a reference I_0 (the setpoint current). Then the error signal $I - I_0$ will be used as a setpoint for a digital or analog PID controller (Proportional Integrator Derivative controller) which will attempt to maintain the measured current constant. Thus, every time current variations are detected during the scanning of the tip, the tip-sample distance is modified to return to the setpoint current. This mode is called constant current mode.
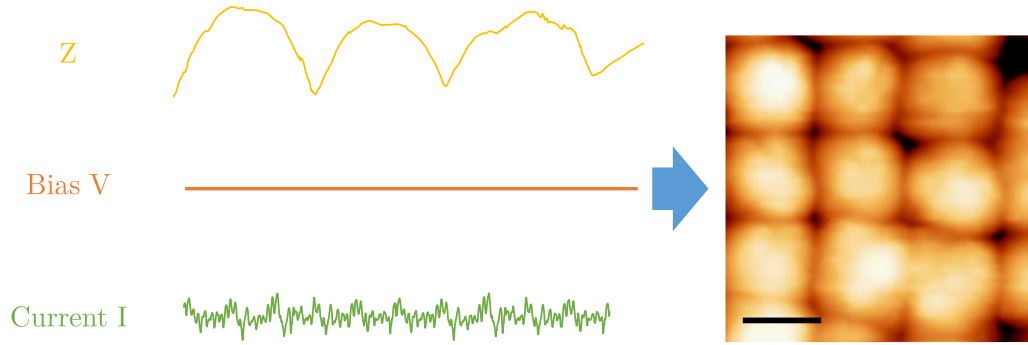
Figure 2.5: Evolution of the various parameters in the constant current topographic mode of the STM. The sample voltage V is kept constant. Thanks to a feedback loop, the tunnel current I is regulated such that it remains constant throughout the scan while the tip-to-sample distance is changed. Therefore, the vertical displacement of the scanner (feedback signal Z) reflects the surface topography. Right : STM image of a PbSe QD superlattice acquired for a setpoint current of 50pA and a voltage of +2.5V. Scale bar is 5 nm.

2.2.2 Lateral resolution of the STM

The tunneling current shows an exponential dependence. We can reasonably assume that it is only the very last atom of the tip that contributes to the tunneling process. If the atom wave function is a s wave, the square of the wave function in the barrier is :

$$|\psi|^2 \sim \frac{e^{-2kr}}{r^2} \tag{2.18}$$

Where r is equal to $r = \sqrt{x^2 + z^2}$ as shown in Fig.**??**. As $z \gg x$, we can write r as :

$$r \simeq z + \frac{x^2}{2z} \tag{2.19}$$
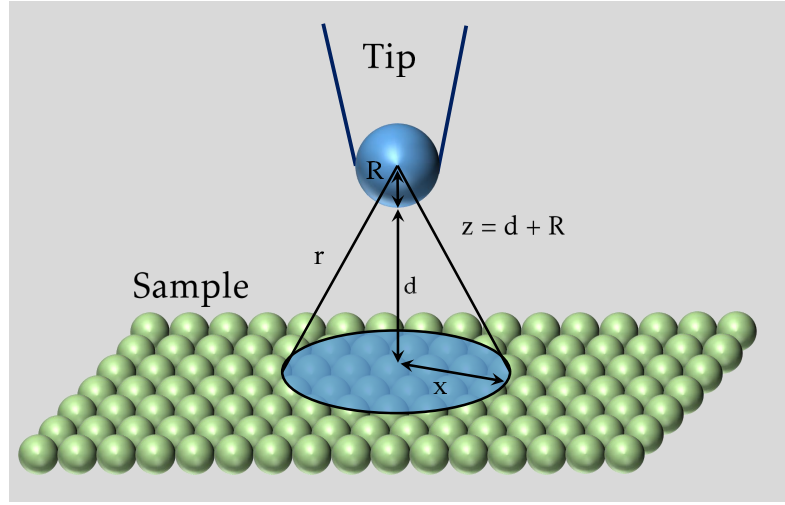
Figure 2.6: Visualization of the lateral resolution of the STM

Injecting Eq.**??** inside Eq.**??**, we obtain :

$$|\psi|^2 \simeq \frac{e^{2kz}}{z^2} e^{-k\frac{x^2}{z}} \qquad (2.20)$$

We can recognize a Gaussian function with a Full Width Hall Maximum (FWHM) of :

$$\Delta x \simeq \sqrt{\frac{2z}{k}} \qquad (2.21)$$

Then the height of the tip is given by :

$$z = R + d \qquad (2.22)$$

where R is the tip radius and d the tip-sample distance (as illustrated on Fig.**??**). In the past, controlled contact experiment has been done in order to estimate the real tip-sample distance and showed the that distance in scanning tunneling experiment is comprised between $d = 4$ Å and $d = 8$ Å [**?**, **?**, **?**]. In the case of a tungsten tip, $k \simeq 1 \text{Å}^{-1}$. According to Tersoff and Hamann [**?**], the height of the tip can be considered equal to the radius of curvature of the tip R (usually equal to a few nanometers), compared to the tip-sample separation (a few angstrom). Based on these values, we deduce:

$$\Delta x \simeq 1.4\sqrt{R} \qquad (2.23)$$

If we consider a tip having a radius of $R = 100$ Å, then a resolution Δx of 14 Å is obtained, which in theory cannot provide the expected atomic resolution. In reality, the atomic resolution is obtained thanks to some protrusions at the very end of the tip from which the tunnel current occurs. In this conditions, we can assume the radius of the protrusions to be around $R = 5$ Å and thus a resolution of $\Delta x = 4.4$ Å is achieved.

2.2.3 The Omicron LT-STM

The apparatus used for the investigation of the samples studied in this work is a commercial Low-Temperature Scanning Tunneling Microscope (LT-STM) from the company Omicron, now ScientaOmicron. This microscope is divided in three main stainless steel vacuum chambers (see Fig.**??**). The analysis chamber and the preparation chamber are kept under Ultra High Vacuum (UHV) thanks to the combination of a turbomolecular pump, an ion ion-getter pump and a titanium sublimation pump (TSP). The Load Lock is pumped with a turbo molecular pump coupled to a primary pump.
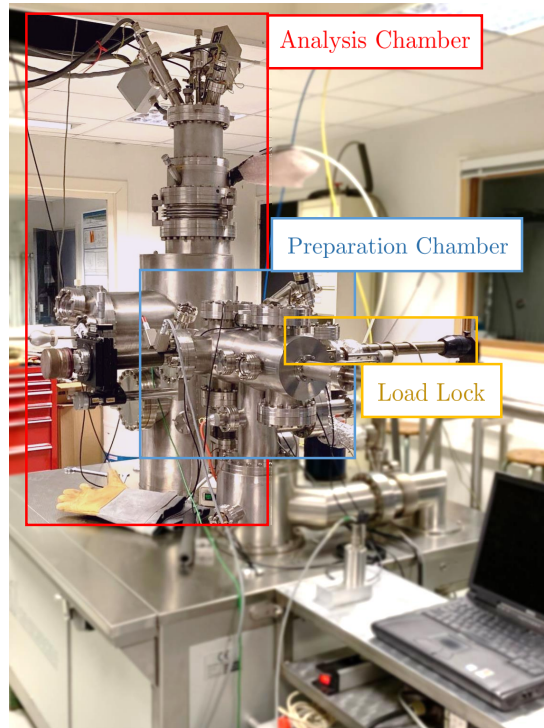
Figure 2.7: Presentation of the Omicron Low Temperature STM.

The Load Lock : This element can be considered as the gate of the STM that allows to load or withdraw samples and tips from the UHV chamber. There are three slots on the magnetic sliding transfer rod, allowing to transfer several tips/sample. The samples are loaded through a viewport that is close using a copper gasket usually (sometimes it can be viton gasket). When entering new elements into the STM, this load lock is pumped (for 9h usually overnight) with the turbo pump of the preparation chamber while being heated up to 120°C to remove contaminant like water. This allows to reach pressure of $P \simeq 10^{-8}$ Torr at best.

Preparation chamber : This part of the chamber is where tips and samples are being prepared before entering the analysis chamber for STM experiment. It also can be used to store tips/samples thanks to the presence of five slots on a storage compartment. The magnetic rod

allows to move samples/tips inside the analysis chamber or to place them on the manipulator. This is the central element of this chamber. It consists in a 3D movable heating stage able to rotate around its axis, with one slot to place the sample. Thanks to a resistive heater consisting of a tungsten filament that can be heated and a thermocouple, the sample temperature can be increased by thermal contact while controlling it. Furthermore, a top contact placed above the manipulator slot can be connected to tip in order to heat it by applying a DC current. Indeed, the polycrystalline tungsten tips used in our experiments must be heated to remove the oxide layer present on their surface. By applying a DC current, the tips are heated by Joule effect at high temperature until a orange color is obtained ($\sim$ 1000K). This is usually achieved by applying a current of about 2 to 3 amperes.

Analysis chamber :   The biggest part of the STM is the analysis chamber. This is where the STM stage is placed. The tip/sample are brought from the preparation chamber and placed on a carousel with six slots. A wobblestick is used to transfer the tip or sample from the carousel to the STM stage. The sample is mounted on a fixed slot. The tip in mounted on this stage with the help of a magnet placed on top of a piezo-ceramic tube supporting the tip and below the sample. The tip can be moved with the coarse approach, achieved thanks to slip-stick inertial sliders. This is used for large movement (5mm in XY and 10mm in Z). The fine approach of the tip to the surface and the image scans are made with the piezo-eletric tube. At room temperature, the piezo can scan over an area of $10\times10\mu$m. But as the temperature decreases so the piezo sensitivity and a smaller area can be covered. At 4K, the tube scan area is reduced to $1.8\times1.8\mu$m. The whole system is suspended with metallic springs in order to reduce vibration from outside and increase the mechanical stability. The STM stage is placed inside two cryostats connected to the STM for cooling down the system. There is one outer cryostat that completely covers the STM to shield it thermally. A smaller one is placed directly in contact with the STM stage to cool it down. The outter cryostat can be filled with liquid nitrogen to reach a temperature down to 77K. The inner crysotat can be filled with nytrogen and liquid helium to cool the STM down to 4K.

2.2.4   Scanning Tunneling Spectroscopy (STS)

In the above section the focus was made on the topographical mode of the STM allowing the study of structural and morphological properties of surfaces. But it is also possible to obtain information about the electronic structure of a sample. From Eq.**??**, the parameter on which the tunnel current depends are the voltage V and the tip-sample distance d. In the topographic mode the voltage V was fixed while the current I was regulated against d by the feedback loop. In the spectroscopic mode, the tip is kept upon an area of interest on the sample. Then to access the electronic properties of the samples the voltage is swept while the feedback loop is open (see Figure **??**). This way the empty and filled states of the sample can be probed.
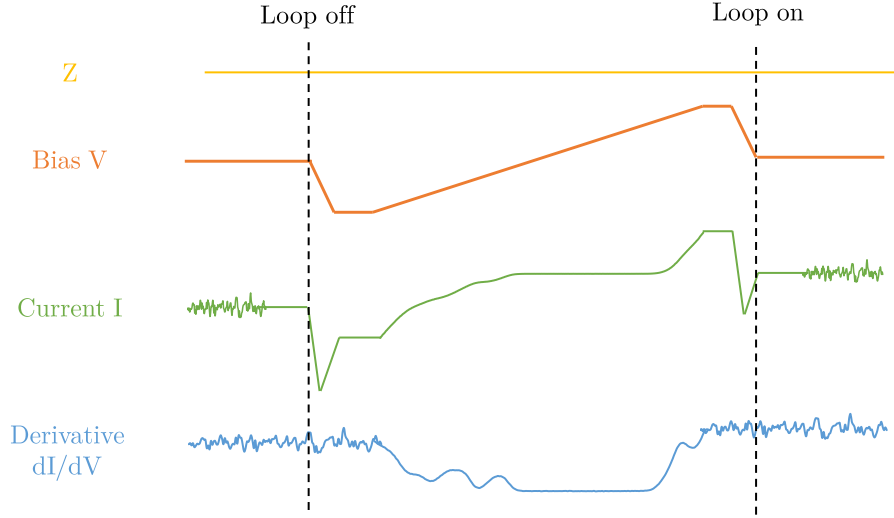
Figure 2.8: Evolution of the different parameters of the tunneling junction during a STS experiment. The tip-sample distance Z is fixed and the feedback loop is open. The bias V is ramped while the current I the measured. At the same time, the derivative (dI/dV) of the current is recorded thanks to a lock in amplifier.

If the density of states of the tip is assumed constant, then the tunneling current can be written:

$$I \propto \rho_t(E) \int_0^{ev} \rho_s(E) T(E, V, d) dE \tag{2.24}$$

By keeping the tip at distance d fixed (by opening the feedback loop) and changing progressively the bias from positive to negative values, the Fermi level of the tip will be shifted up or down compared to the Fermi level of the sample. At positive bias, an electron will tunnel from the tip to the sample (see Fig.**??**) giving a tunnel current proportional to the empty density of states of the sample. At negative bias, it is the electron from the filled states of the sample that tunnels to the tip and the tunnel current yields the filled states of the sample. One of the first report of this study has been done by Feenstra and al [**?**].

Thanks to a lock-in amplifier, we can modulate the voltage and get a direct measurement of dI/dV. The main interest of the dI/dV over the basic I(V) curve, is that the dI/dV is directly proportional to the LDOS. Thus from Eq.**??** we have :

$$\frac{dI}{dV} = e\rho_t \rho_s(eV) T(eV, eV) + e\rho_t \int_0^{eV} \rho_s(E) \frac{d}{d(eV)} (T(E, eV)) dE \tag{2.25}$$

Since ρ_t is considered as a constant, dI/dV is dependent of the variation of the density of state of the sample ρ_s. As $T(E, eV)$ is an exponential function it induces a larger contribution of the states lying at higher energy from the Fermi level. Thus, the signal of dI/dV increase exponentially too and may become significant at higher bias in semiconductor. It has been shown by Feenstra et al [**?**][**?**] that this 'parasite' dependence could be cancelled by normalizing

the differential conductance by a factor I/V :

$$\frac{\frac{\partial I}{\partial V}}{\frac{I}{V}} \propto \frac{\rho_s(eV) + \int_0^{eV} \frac{\partial}{\partial eV}(T(E,eV)) \frac{\rho_s(E}{T(eV,eV)} dE}{\frac{1}{eV} \int_0^{eV} \frac{T(E,eV)}{T(eV,eV)} \rho_s(E) dE} \tag{2.26}$$

The second term of the numerator is a slowly decaying background term. From this observation we can conclude that the main dependence of $\frac{\partial I}{\partial V}/\frac{I}{V}$ come from the LDOS of the sample $\rho_s(eV)$. Thus one can write :

$$\frac{\frac{\partial I}{\partial V}}{\frac{I}{V}} \propto \rho_s(eV) \tag{2.27}$$

This type of spectroscopy gives us information about the density of states in a very localized manner. Coupled with the high resolution of the topographical mode, one can search from structure and precisely characterize its electronic properties at the nanoscale.

Lock In Amplifier

While acquiring an I(V) curve may be a relatively easy thing to do, getting access to the dI/dV signal is trickier. One could say that it could be accessible by averaging multiple I(V) curves and using the numerical derivative of the current. Unfortunately, due to the current fluctuation (due to mechanical instability, electronic noise in the junction and in the instruments, for example) this method has a poor signal-to-noise ratio, making the spectroscopic features hard to distinguish. A better alternative is to use a Lock-In amplifier instead.

A Lock-In amplifier use a phase sensitive detection and it allows to measure the amplitude of an AC signal even in presence of strong noise. The noisy signal can be written as :

$$V_s(t) = A.\cos(2\pi f_s t + \theta_s) \tag{2.28}$$

If this signal is modulated by a reference :

$$V_r(t) = B.\cos(2\pi f_r t) \tag{2.29}$$

Then we obtain :

$$V_s(t) \times V_r(t) = \frac{1}{2} AB(\cos(f_r - f_s + \theta) + \cos(f_r + f_s + \theta)) \tag{2.30}$$

By artfully selecting $f_r = f_s$, then the product transforms into 2 terms : a phase dependent term $1/2AB\cos(\theta)$, and an oscillating term at the sum of the frequency $1/2AB\cos(2f_r + \theta)$. The constant term can be selected by applying a low pass filter with a threshold lower than f_r. This way the output signal contains information about the phase and the amplitude of both signals.

In the case of STM, a small high-frequency sinusoidal signal $V_{mod}\sin(\omega_{mod}t + \theta)$ is used to

modulate the bias voltage at the frequency ω_{mod}. Thus, in case of small modulation V_{mod}, the tunnel current can be expanded in a Taylor series :

$$I(V_{bias}+V_{mod}\sin(\omega t + \theta)) \simeq I(V_{bias}) + \frac{d}{dV}I(V_{bias})V_{mod}\sin(\omega t + \theta) + \frac{d^2}{dV^2}I(V_{bias})V_{mod}^2\sin(\omega t + \theta)+... \tag{2.31}$$

As explained above a reference signal $A\sin(\omega_{mod}t + \theta_r)$ at the same frequency ω_{mod} is used to modulate the current through a multiplier circuit. The mixed signal is composed of a constant term, $1/2A\frac{dI}{dV_{bias}}\cos(\theta - \theta_r)$, and several harmonics that can be removed with a low pass filter. In order to optimize the phase difference and get a higher amplitude with respect to the modulated signal the Lock-In also possessed a phase shifter. As a result, the output of the lock-in amplifier provides the quantity $dI(V)/dV$.

2.2.5 The spectroscopy technique applied to semiconductor colloidal quantum dots

A large part of this work relies on the study of colloidal quantum dot (QD) by STS. As the QDs are usually not grounded and deposited on a substrate, the interpretation of the STS data requires additional explanations.

Double Tunneling Barrier Junction

The QDs have to be deposited on a flat and conducting substrate either by binding the QDs to the substrate using chemical linkers, or by drop casting the suspension on a clean surface resulting in a close-packed array. Then, STM can be performed to characterize the QD individual shape or their packing when arranged in an assembly. The electronic structure of a QD is obtained by stabilizing the STM tip above a selected QD and the current is acquired as function of the bias applied between the tip and the substrate. In this case, the system Tip/QD/substrate form the so-called Double Barrier Tunnel Junction (DBTJ) [**?**], as shown in Fig.**??** (A). The tip-QD junction consists of a vacuum gap, whereas the junction between the particle and the substrate is mainly due to ligands.

Voltage distribution in the double-barrier tunnel junction : In the case of a DBTJ, the applied voltage will be distributed over the two barriers. The distribution of this voltage over the DBTJ is characterized by the lever arm η. From an electrical point of view, the DTBJ can be modeled as two capacitors in series according to the equivalent circuit shown in Figure **??**B. The total applied voltage V_{tot} is distributed over the capacitors with one fraction dropping over the QD-substrate junction :

$$V_{\text{QD/sub}} = V_{\text{tot}}\frac{C_1}{C_1 + C_2} \tag{2.32}$$

and the other over the tip-QD junction :

$$V_{\text{tip/QD}} = V_{\text{tot}}\frac{C_2}{C_1 + C_2} \tag{2.33}$$
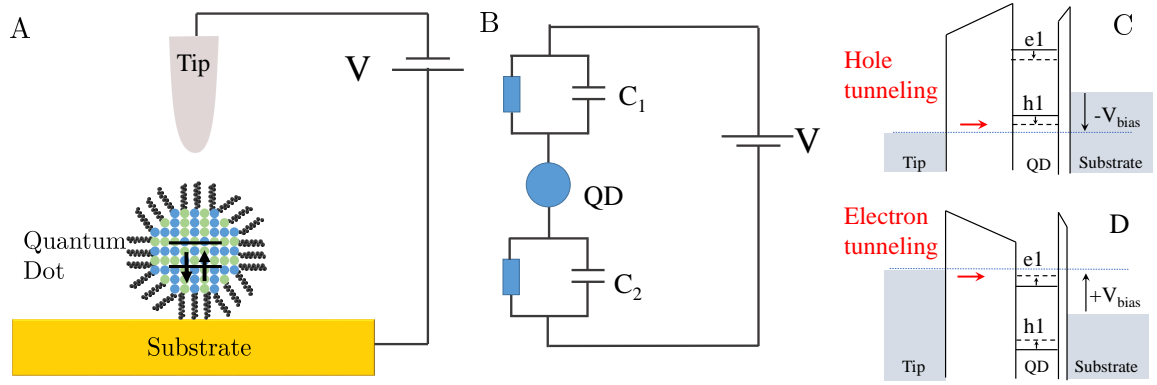
Figure 2.9: A) Schematic representation of a DBTJ configuration. B) Equivalent circuit of the DTBJ system. C) Electron tunneling through the lowest conduction level e_1 at positive bias. D) Hole tunneling at the highest valence level h_1 at negative. The effect of the bias positive (negative) voltage on the energetic position of the QD discrete states is illustrated by the shift upward (downward) from the solid lines to the dashed lines.

The lever arm η is defined as the fraction of the voltage applied between the tip and the substrate that drops between the QD and the tip, thus :

$$\eta = \frac{V_{\text{tip/QD}}}{V_{\text{tot}}} \tag{2.34}$$

Thus the effective potential at the QD will not be the same as the total applied bias when $\eta < 1$. In this case the discrete states of the QD will shift with the applied bias V_{tot} from their zero-bias position (Figure **??**(C) and (D)) because a higher bias V_{tot} has to be applied to the DBTJ in order to provide to the charge carrier enough energy to tunnel into the QD. Therefore, resonance peaks corresponding to the energies of levels relative to the Fermi level e_1 and h_1 will occur at specific voltages $V_{e_1^+}$ and $V_{h_1^-}$ which depend of the lever arm η [**?**].

In addition the tunneling rate of the electrons across the two barriers needs to be taken into account. Tunneling spectroscopy on QD is based on resonant tunneling of electrons (holes) across the DTBJ, as shown in Figure **??**(B) and (C). It involve two processes, tunneling from the tip and the QD at the rate Γ_{in}, and tunneling from the QD to the substrate at the rate Γ_{out}. The first one (Γ_{in}) can be modified by changing the width of the tip/QD barrier (by moving the tip closer for example) but the second one (Γ_{out}) is fixed. The ratio of these rates, Γ_{in}/Γ_{out}, will determine the electron occupation in the QD. This refers to the number of electrons added inside the QD. It will play a key role in the interpretation of tunneling spectra. Mainly, two tunneling regimes can be identified depending on the Γ_{in}/Γ_{out} ratio.

Shell Tunneling regimes

When $\Gamma_{in} \ll \Gamma_{out}$, the so-called shell-tunneling regime occurs and no more than one electron (hole) can be present at a time in the QD. When one electron is injected from the tip it is

evacuated trough the substrate by the time a second electron arrives from the tip [**?**, **?**]. In this regime, the peaks on both sides of the zero conductance gap are related to the electrons and the holes [**?**]. The voltages at which the resonances through the quantum states e_1 and h_1 occur can be written :

$$V_{e1}^+ = \frac{e1 + \Sigma_e}{\eta e} \quad \text{(electron)} \quad V_{h1}^- = \frac{h1 - \Sigma_h}{\eta e} \quad \text{(hole)} \tag{2.35}$$

Here Σ_e and Σ_h stand for the polarization energy of the hole and the electron, i.e., the energy needed to inject an electron (hole) inside a QD while the polarization charge left behind in the electrode still interact with the electron (hole). As mentioned above the value of these voltages is strongly related to the lever arm η and thus to the nature of the DBJT. The polarization energy depends on the dielectric mismatch between the QD core and its surrounding [**?**, **?**] :

$$\Sigma = \frac{1}{2} \frac{e^2}{4\pi\epsilon_0 R}\left(\frac{1}{\epsilon_{out}} - \frac{1}{\epsilon_{in}}\right) + \frac{0.47e^2}{4\pi\epsilon_0 \epsilon_{in} R}\left(\frac{\epsilon_{in} - \epsilon_{out}}{\epsilon_{in} + \epsilon_{out}}\right) \tag{2.36}$$

Where R is the radius of the QD, ϵ_{in} the dielectric constant of the QD and ϵ_{out} the effective dielectric constant of the environment of the QD. The zero conductance gap $\Delta V_{STM} = V_{e1}^+ - V_{h1}^-$ measured in STS experiments (see Figure **??** C and D) is then related to the real band gap $(e_1 - h_1)$ by the separation between the electron and hole resonances and the polarization energy :

$$\eta e \Delta V_{STM} = \eta e (V_{e1}^+ - V_{h1}^-) = e1 - h1 + \Sigma_h + \Sigma_e \approx e1 - h1 + 2\Sigma \tag{2.37}$$

where the approximation $\Sigma_h + \Sigma_e \approx 2\Sigma$ is good as the polarization energy is not sensitive to the exact shape of the wavefunction. The dI/dV spectra directly reflect the LDOS of the QD because electron-electron interaction are not present in the shell-tunneling regime. All the features of this regime are showed in Figure **??** (C) where a CdSe QD is measured under shell-tunneling condition [**?**].

Shell filling regime

When $\Gamma_{in} \gg \Gamma_{out}$, it becomes possible to fill the QD with two electrons (holes) at the same time. This leads to the splitting of the first resonance peak because of electron-electron repulsion. Hence, the voltage at which the resonance through the first electron level e_1 can be re-written :

$$V_{2e1}^+ = \frac{e1 + \Sigma_e + J_{e-e}}{\eta e} \quad \text{(2 electrons in the dot)} \tag{2.38}$$
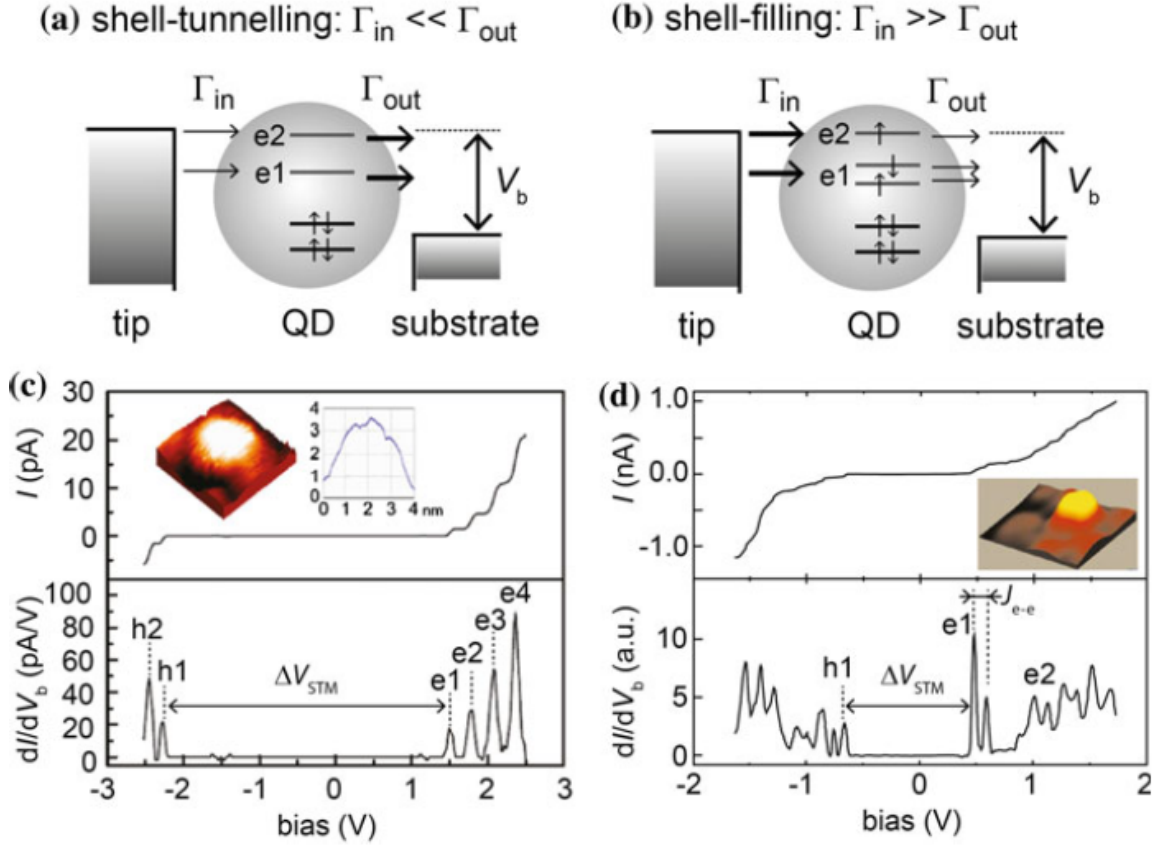
Figure 2.10: Illustration of the two different regimes in tunneling spectroscopy on isolated QD. The experimental result for shell tunneling regime acquired on CdSe QD [?] is shown in (c) while shell filling experimental spectrum of an InAs QD [?] is shown in (d). Figures taken and adapted from [?] and [?]

Where J_{e-e} correspond to the electron-electron repulsion [?, ?] :

$$J_{e-e} = \frac{e^2}{4\pi\epsilon_0 R}\left(\frac{1}{\epsilon_{out}} + \frac{0.79}{\epsilon_{in}}\right) \tag{2.39}$$

Just like the polarization energy, J_{e-e} depends on the mismatch between the dielectric constant of the QD (ϵ_{in}) and the effective dielectric constant of the surrounding (ϵ_{out}). The characteristic features of the shell-filling regime is visible in the Figure ?? (d), which shows experimental results on an InAs QD [?]. The doubling of the first peak above the zero conductance gap at positive bias on this spectra illustrates the splitting of the first electronic level because of the electron-electron interaction.

Electron or hole transport on both sides of the gap

In the case of colloidal QD with long native ligands or having core-shell heterostructure, a more symmetric potential distribution over the DBTJ happens, leading to a lever arm with value around $\eta = 0.5$. Moreover, the Fermi level is not always positioned midgap and lies closer to the valence or conduction band. If these two effects combine then it is possible that

tunneling of electrons (holes) on both sides of the zero conductance gap occurs. For example, at negative bias, it is possible that before the tip Fermi level reaches resonance with the first valence level of QD, the substrate Fermi level becomes resonant with a conduction band level, resulting in tunneling through this level. In this case, the zero conductance region ΔV_{STM} is not related to the separation between the first conduction and valence level. ΔV_{STM} is smaller than the actual gap, leading to misleading interpretation of the gap value. If holes tunnel on both sides of the zero conductance region, ΔV_{STM} is given by :

$$\Delta V_{\text{STM}} = \frac{1}{\eta(1-\eta)}(h_1 - \Sigma_h) \tag{2.40}$$

For the electron this relation changes to :

$$\Delta V_{\text{STM}} = \frac{1}{\eta(1-\eta)}(e_1 + \Sigma_e) \tag{2.41}$$

In the case of tunneling through the electron level e_1, this results in a conductance peak at a
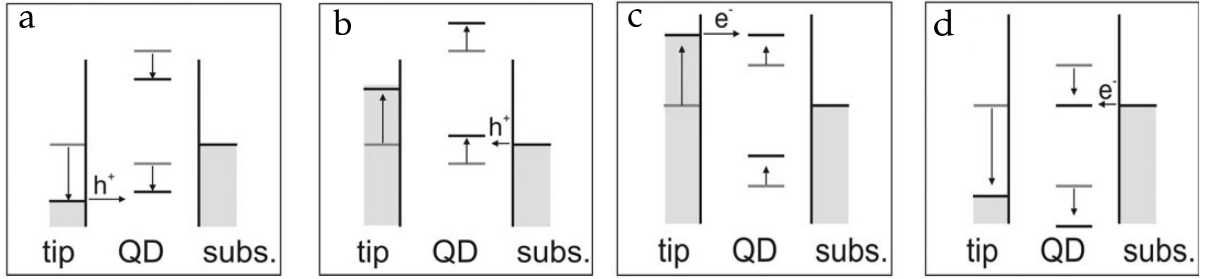
Figure 2.11: (a) and (b) panels show schematics of tunneling of holes through the h_1 valence level both at (a) negative and (b) positive bias. (c) and (d) panels show schematics of tunneling of electron through the e_1 valence level both at (c) negative and (d) positive bias. In the schematic diagrams, the position of the Fermi level of the substrate is kept constant. Figures taken and adapted from [?]

negative bias $V_{e_1}^-$ given by :

$$V_{e_1}^- = -\frac{e_1 + \Sigma_e}{e(1-\eta)} \tag{2.42}$$

Alternatively, in the case of tunneling through hole level h_1, the conductance peak occurs at a positive bias $V_{h_1}^+$ given by :

$$V_{h_1}^+ = -\frac{h_1 - \Sigma_h}{e(1-\eta)} \tag{2.43}$$

By combining the two above equations, an expression of the lever arm for unipolar transport can be found for both hole and electron unipolar transports :

$$\eta = \frac{V_{h_1}^+}{V_{h_1}^+ - V_{h_1}^-} \quad \text{(hole)} \quad \eta = \frac{V_{e_1}^-}{V_{e_1}^- - V_{e_1}^+} \quad \text{(electron)} \tag{2.44}$$

The easiest way to identify the nature of the peaks at positive and negative bias in a STM spectra is by looking at the shift in the peaks voltages as function of the setpoint current. Indeed, by increasing the setpoint current, the tip-QD distance changes, modifying the lever arm. At positive bias, $V_{e_1}^+$ will increase while $V_{h_1}^+$ will decrease and shift toward negative bias as the lever arm is reduced. At negative bias, on the other hand, the opposite happens where $V_{e_1}^-$ will move toward positive bias and $V_{h_1}^-$ will shift toward negative bias when reducing η. This behavior will be important to detect in order to identify the nature of the peaks measured in chapter 3.

2.3 MultiProbe Scanning Tunneling Microscopy

The goal of the former section was to present scanning tunneling microscopy. The main advantages of this technique are also its worst drawbacks. Indeed, the information about the electronic structure or the topography only relies on a very local, nanometric scale. However, the integration of nano-object and nano-devices into more complex systems requires the study of collective phenomena of conduction inside these structures. Most of the time, the transport properties of material are investigated with the help of lithographed contacts. But that method is very intrusive as it involves many technological processes on the sample. Moreover it does not allow much flexibility as the contact cannot be moved once deposited (for varying the distance between contact for example). On the other hand, MultiProbe STM is an experimental technique allowing to investigate transport properties on length from hundred of microns to hundred of nanometers under ultra high vacuum condition. The MultiProbe STM possess four independent STM tips that are used to contact the sample and measure its resistivity by varying the intertip distance. The addition of a SEM above the four STM tips allow to selectively choose any area of interest on the sample. The MultiProbe allows for flexible and non destructive resistance measurements that lithography cannot provide.

2.3.1 Electrical transport measurements

Principle of the four-point measurement

In order to characterize objects of small dimensions, the tips of the microscope are used as contact electrodes. The easiest way to get information about the resistance of a sample is to perform two-point resistance measurement, as shown in Fig. **??** (a). In this configuration the two tips are used to inject the current and to probe the voltage as well. Therefore the measured resistance $R_{measured} = V/I$ does not only include the contribution of the measured sample, but also the one of the parasitic resistance that come from the contact of the tip with the sample $R_{measured} = 2R_{Contact} + R_{sample}$ (the contact resistances are assumed to have the same value here). It should be noticed that in macroscopic measurements the contact resistance can often be neglected. But since the STM tip is usually small and sharp, the contact area with the sample is very small, leading to a large resistance contact. In the case of very good conductors

the contact resistance will dominate [**?**]. Therefore, four-point measurements are mandatory for contacting nano-scale object.
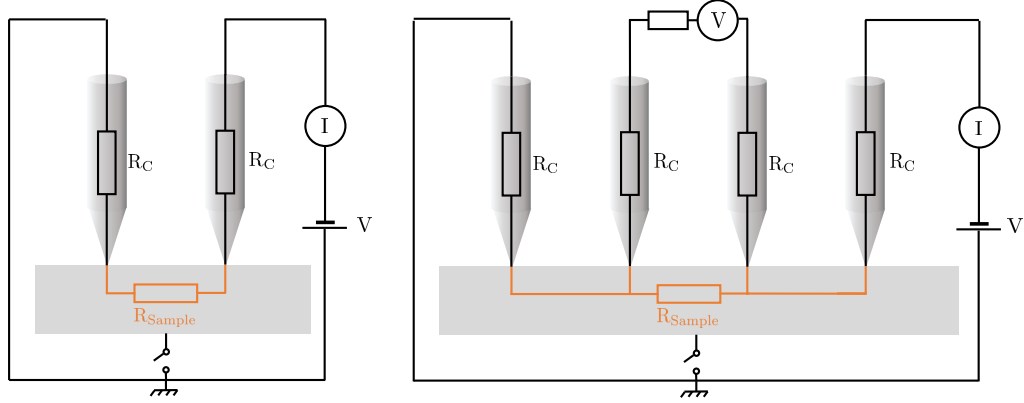
Figure 2.12: Two-tip resistance measurement in which the contact resistance influences the measured total resistance. Four-point resistance measurement, on the contrary, excludes the influence induced by the contact resistances.

The four-point measurement circuit is showed in Fig.**??** (b). Here, two tips are used to inject and collect the current into the sample while the two central tips are used as probes to measure the potential drop induced by the injection of the current. The current injected inside the sample is independent of the contact resistance at the source and drain tips. If the voltage measurement is performed with a large internal resistance such as $R_V \gg R_{sample} + 2R_{contact}$ then the contribution of the contact resistance to the measured resistance can be neglected [**?**].

Four-point measurement at the small dimension

At the macroscopic scale, the current flowing through a semiconductor during a four-point measurement can pass trough different channels, like the surfaces states (that can be associated with particular atomic reconstruction [**?**]), through space-charge layer (which can be caused by the pinning of the Fermi level at the surface of the semiconductor for example) and finally by the states from the bulk, independent of the surface [**?**]. Depending on the tip distance, the number of accessible channels can be varied. For example, at small tip separation, the current lines will stay shallow and the major contribution arises from the surface conductivity. These different conduction channels are illustrated on Figure **??**. Figure **??** shows the four-point resistance as function of the distance d between the tip is show for a clean Si wafer, i.e. with a Si(111)-7×7 surface, and for the same wafer with the $\sqrt{3} \times \sqrt{3}$ - Ag-Si(111) structure prepared. The four-point measurements are carried out with the four tips in the linear and equidistant configuration. The two different behaviors of the Si(111)-7×7 and $\sqrt{3} \times \sqrt{3}$ - Ag-Si(111) surfaces can be explained by considering the different channels discussed above.
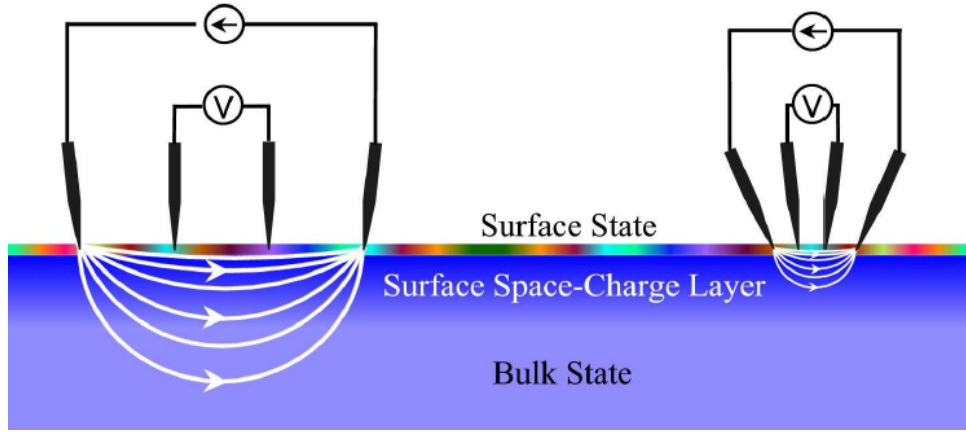
Figure 2.13: Four-point transport measurement on a surface at the a) macroscopic scale b) microscopic scale. The distribution of current flowing therough the sample is schematically drawn. Figure taken from [?].

For a sample considered like a tridimensional and homogeneous resistive material, then the measured resistance as function of the probe spacing is [?]:

$$R_{3D}^{4p}(d) = \frac{\rho_{3D}}{2\pi d} \tag{2.45}$$

Where ρ_{3D} is the resistivity of a 3D sample. The tilted blue band in Figure ?? represents the four-point measurement expected for a semi-infinite crystal following the above equation. But it only fits the experimental data for the sample with the 7×7 surface and for probe spacing between 10μm and 100μm. The central inset of Fig ?? (a) shows that the field lines are not disturbed by the crystal geometry in this case. On the contrary, when the probe spacing d exceed 100μm, the current cannot spread out due to the finite thickness of the sample. Thus the current distribution becomes compressed by the sample geometry as depicted by the right inset of Fig ?? (a). On the other hand, for small probe spacings (d¡10μm), a huge increase of the resistivity is measured. This is due to the special atomic reconstruction of the Si(111)-7×7 surface that creates dangling bonds at the surface. Because of this reconstruction, a Fermi level pinning in the middle of the gap is observed, creating a space charging region close to the surface with a low carrier density. As symbolized by the left inset of Figure ?? (a) the current only flows near the surface and does not reach the bulk. Therefore, the increase in resistivity is explained by a transport in this space-charge layer which, in this case, consists in a poorer conductor than the bulk.

The Si(111) - $\sqrt{3} \times \sqrt{3}$ - Ag surface exhibits a very different behavior. For this system the resistance shows a monotonous but small dependence on the probe spacing d. That is because this sample possesses a bi-dimensional free electron gas at the surface. Therefore the transport is dominated by this surface transport with a conductivity well above the bulk conductivity. In this case, the resistance does not depend on the probe spacing d [?] :

$$R_{2D}^{4p} = \frac{\rho_{2D}}{\pi}\ln(2) \tag{2.46}$$
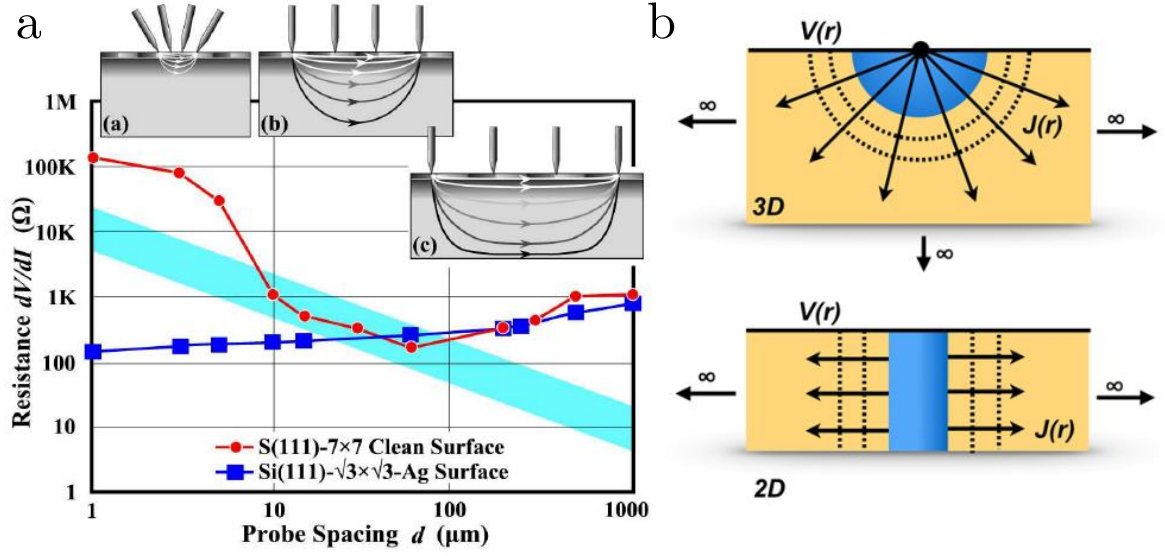
Figure 2.14: a) Four-point transport measurement on a Si(111) - $\sqrt{3} \times \sqrt{3}$ - Ag surface (blue square) and a Si(111)-7×7 surface (red square) at the macroscopic scale and microscopic scale. The distribution of current flowing through the sample is schematically drawn. Figure taken from [?]. b) Voltage V(r)and current density J(r) profiles for a semi-infinite 3D material and infinite 2D sheet. Figure taken and adapted from [?].

However the resistance measured by the four-point method is not a fundamental property of the material, as it depends on the position of the tips on the samples. The equation above shows how to extract the resistivity of the sample for the simplest probe configuration, the collinear equidistant arrangement with a constant probe spacing d. But other configurations exist and require corrections to get access to the resistivity or conductivity of the samples.

The different tip configurations

In the above section, the equations allowing us to extract the resistivity of a sample were valid for equidistant configuration of the tips. Now, we will discuss different other configurations. Depending on the sample configuration or on the tip shape, collinear equidistant arrangement is not always easy to implement. In this case, the most general non-linear probe arrangement equation can be used to access the sample resistivity (see Figure **??** (a)).

Thus, in the most general case (Fig **??** (a)), the current is injected by tip 1 and collected by tip 4 while voltage is probed by tips 2 and 3. The Ohm law for the 3D case results in :

$$R_{3D}^{4p}(\overrightarrow{d_1}, \overrightarrow{d_2}, \overrightarrow{d_3}, \overrightarrow{d_4}) = -\frac{\rho_{3D}}{2\pi} \cdot \left[\frac{1}{|\overrightarrow{d_3} - \overrightarrow{d_1}|} - \frac{1}{|\overrightarrow{d_3} - \overrightarrow{d_4}|} - \frac{1}{|\overrightarrow{d_2} - \overrightarrow{d_1}|} + \frac{1}{|\overrightarrow{d_2} - \overrightarrow{d_4}|} \right] \qquad (2.47)$$
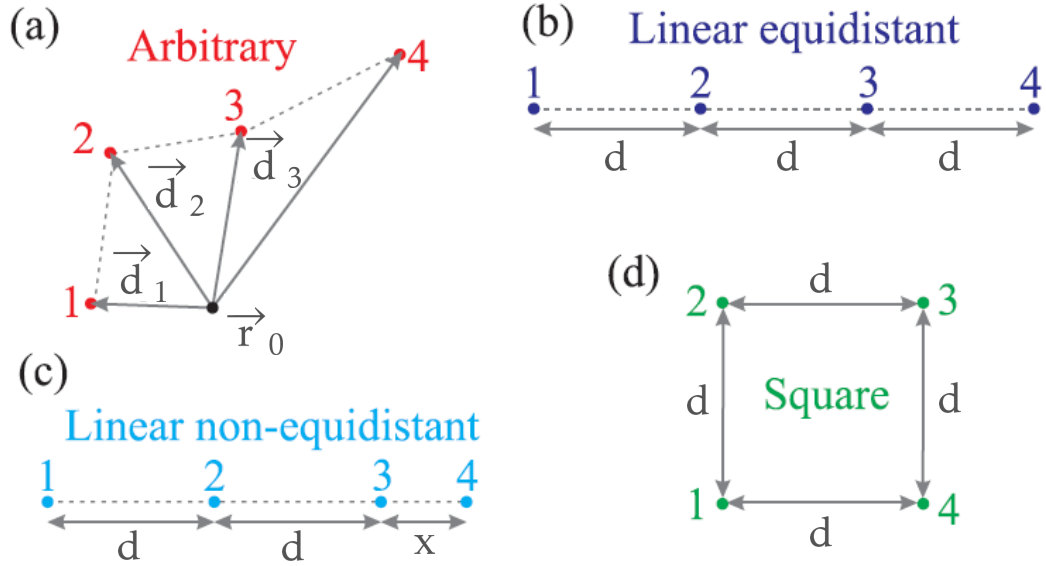
Figure 2.15: Tip configurations for a four-probe measurement. (a) Most general non-linear probe arrangement. (b) Linear equidistant probe arrangement. (c) Linear not equidistant probe arrangement with three tips spaced equally by the distance s and one distance x being not equidistant. (d) Square probe arrangement with which an anisotropy of the resistivity can be detected. From [?]

And for the 2D case :

$$R_{2D}^{4p}(\vec{d_1}, \vec{d_2}, \vec{d_3}, \vec{d_4}) = -\frac{\rho_{2D}}{2\pi} \ln\left[\frac{|\vec{d_3} - \vec{d_4}|.|\vec{d_2} - \vec{d_1}|}{|\vec{d_3} - \vec{d_1}|.|\vec{d_2} - \vec{d_4}|}\right] \tag{2.48}$$

Linear non-equidistant configuration : An interesting configuration is the linear non-equidistant configuration, showed in Figure **??**). Indeed, this method allows to perform resistance measurements while moving only one tip. One can see that this is easily the most convenient and efficient way to perform four-point measurement as function of the distance. Therefore only one tip distance, labeled x in Figure **??** is changed while the two other tip distances, labeled d, are fixed. In this case, the 3D equation becomes :

$$R_{3D}^{4p}(d,x) = \frac{\rho_{3D}}{2\pi} \cdot \left[\frac{1}{x} + \frac{1}{2d} - \frac{1}{d+x}\right] \tag{2.49}$$

and the 2D case :

$$R_{2D}^{4p}(d,x) = \frac{\rho_{2D}}{2\pi} \cdot \left[\ln(\frac{2d}{x}) - \ln(\frac{d}{x+d})\right] \tag{2.50}$$

46
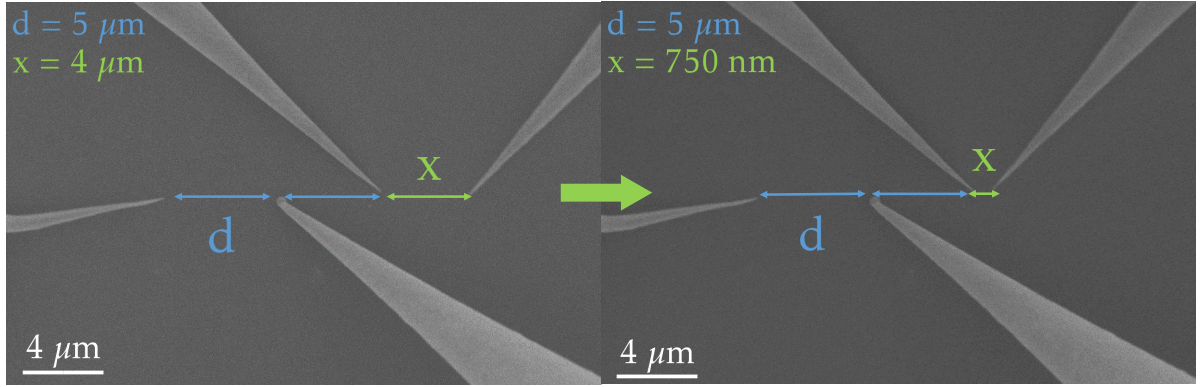
Figure 2.16: Tip configurations for a four-probe measurement. Linear not equidistant probe arrangement with three tips spaced equally by the distance s and one distance x being not equidistant.

Square Configuration :   Until now we assumed that the sample exhibited isotropic conductivity. But in many cases it may not be the case and the standard in line configuration cannot bring information about the anysotropy of the conductivity. For a bi-dimensional transport on an infinite surface, the result of a four-point measurement with an equidistant spacing d between the tip in linear configuration is given by [**?**] :

$$R_{linear} = \frac{1}{\pi \sqrt{\sigma_x \sigma_y}} \ln(2) \qquad (2.51)$$

This equation is similar as Eq.**??** where R does not depend on the tip spacing d. For the same resistance measurement with the tip aligned with y axis, the conductivities σ_x and σ_y need to be permuted. This does not change the result and thus it is not possible to differentiate σ_x from σ_y. It turns out that the linear four-point measurement is not sensitive to a two-dimensional conductance anisotropy. However, the square configuration (also called van der Pauw configuration,[**?**]), showed in Figure **??** (d), is more suitable because it is sensitive to this anisotropic surface change in the conductivity. Here the tips on one side (for example 1 and 2) inject and drain the current and the other two (3 and 4) probe the voltage. Thus four rotation angles can be measured for one fixed orientation of the square, by assigning different probes as current and voltage probes. For the square configuration the resistance becomes :

$$R_{square} = \frac{1}{2\pi \sqrt{\sigma_x \sigma_y}} \times \ln\left(1 + \frac{\sigma_y}{\sigma_x}\right) \qquad (2.52)$$

In this case a rotation of 90° implies a permutation of σ_x and σ_y in the above equation. Therefore the measured resistance changes if the sample exhibits a conductance anisotropy. By rotation of the square by an angle θ, multiple directions can be probed on the same area. The four-point resistance resulting from such a measurement configuration, determined by Poisson

equation becomes [**?**, **?**] :

$$R_\theta = \frac{1}{2\pi\sqrt{\sigma_x\sigma_y}} \times \ln\left(\frac{(\frac{\sigma^x}{\sigma^y}+1)^2 - 4\cos^2\theta\sin^2\theta(\frac{\sigma^x}{\sigma^y}-1)^2}{(\sin^2\theta + \frac{\sigma^x}{\sigma^y}\cos^2\theta)^2}\right) \tag{2.53}$$
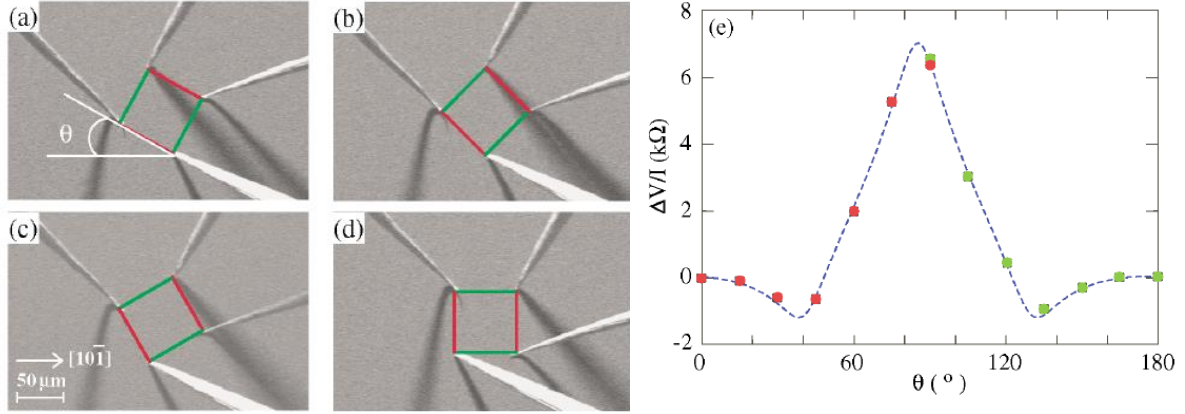
Figure 2.17: SEM images of rotational square four-point resistance measurements with 60 μm probe spacing, at (a) $\theta = 30$, (b) $\theta = 45°$, (c) $\theta = 60°$, and (d) $\theta = 90°$. (e) Angle dependence of the measured resistance of the single-domain 4×1-In surface. Experimental data are fitted by Eq.**??**. Figures taken and adapted from [**?**]

An example of an angle dependence measurement of the four-point resistance is shown in Figure**??**. Here the four-point measurement reveals an anisotropic conductance in the surface reconstruction of a 4×1-In layer formed on a Si(111)-7×7 wafer. The fit visible in Figure**??** (e) corresponds to the equation **??**.

2.3.2 The Nanoprobe, A multiprobe STM

Presentation of the microscope

The Nanoprobe (Omicron) is a sophisticated instrument that allows for local and non-destructive four-point resistance measurements. In that regard, it is more accurate to see it non as a standard STM but a multimeter specially designed for the investigation of electrical properties of materials down to the nanoscale.

Figure **??** shows a picture of the Omicron Nanoprobe. Just as the Omicron LT-STM described earlier, the UHV system consists of preparation chamber (red box), load lock (yellow box), an analysis chamber (blue box) and a SEM (green box). The first two elements are similar to the Omicron LT-STM and therefore won't be described again here. On top of the analysis chamber the column of the SEM is placed just above the sample and the tips. The presence of this additional microscope is central as it allows for probe positioning on the sample, especially when the probe spacing reaches sub-micron distances. The analysis chamber is isolated

from the preparation chamber. It contains the characterization platform and a storage carousel which possesses 10 slots.
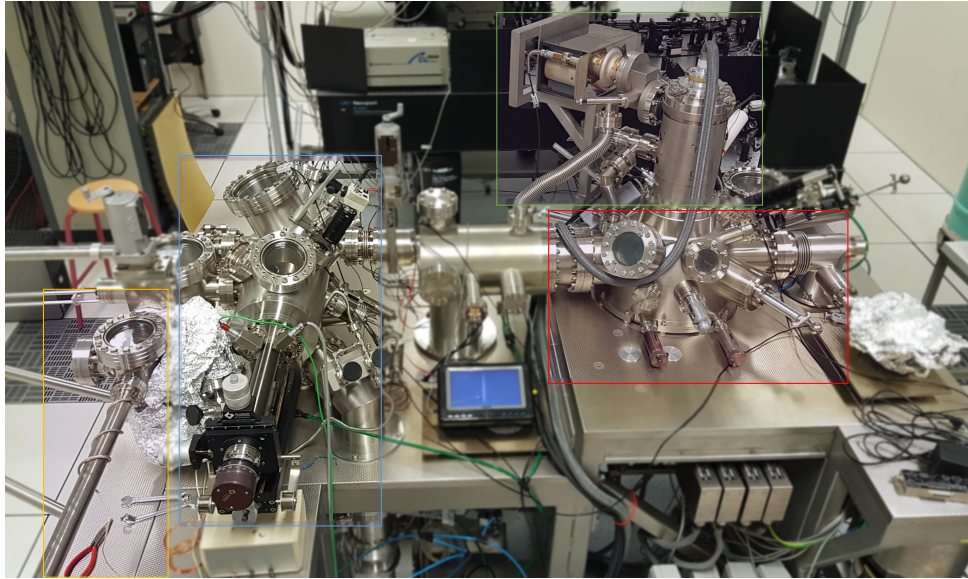
Figure 2.18: The Omicron 4-probes STM chamber (blue box), SEM (green box), preparation chamber (red box) and load lock (yellow box).

The Figure **??** shows the platform containing the four STM scanners labeled as Tip 1 to 4. The scanners are divided in two types, three Low Resolution (LR) tube scanners and one High Resolution (HR) stack of piezoceramics. For the latter one, the tip is closer from the sample and thus less sensitive to mechanical vibrations. This increase of stability is essential to image the atomic structures of clean and well-ordered surfaces. With the help of the SEM a 'rough' approach of the tips to the surface can be performed with sliders for coarse positioning while making sure the tips does not touch each other. Once this is done, a finer approach is performed thanks to the piezoelectric tube scanner or the pizeoelectric stack actuator.
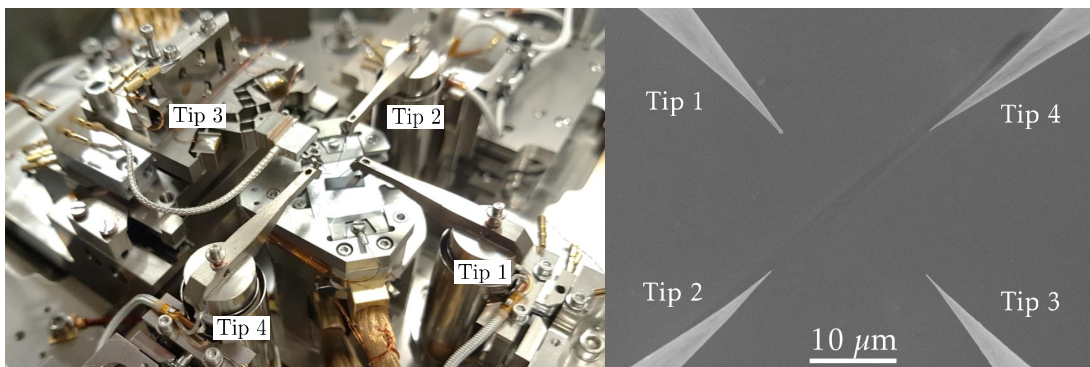
Figure 2.19: Left : Picture of the platform with the four independent STM scanners. The one labeled as Tip 3 is a High Resolution (HR) scanner while the three others are Low Resolution (LR) scanner. A sample is also visible on the platform. Right : SEM image of four sharp STM tips above a surface.

49

Tips preparation

All the tips used in the different STM experiments were home made tungsten tips. The procedure to prepare these tips involves an electrochemical etching of a thin polycristalline wire of tungsten. The tungsten wire is immersed into a sodium hydroxide (NaOh) solution surrounded by a circular electrode and a DC voltage is applied between the tip and the solution. The reaction governing this electrochemical process is :

$$
\begin{aligned}
\text{cathode} \quad & : \quad 6H_2O + 6e^- & \rightarrow \quad & 3H_2(g) + 6OH^- \\
\text{anode} \quad & : \quad W(s) + 8OH^- & \rightarrow \quad & WO_4^{2-} + 4H_2O + 5e^- \\
\text{full reaction} \quad & : \quad W(s) + 2OH^- + 2H_2O & \rightarrow \quad & WO_4^{2-} + 3H_2(g)
\end{aligned}
\tag{2.54}
$$
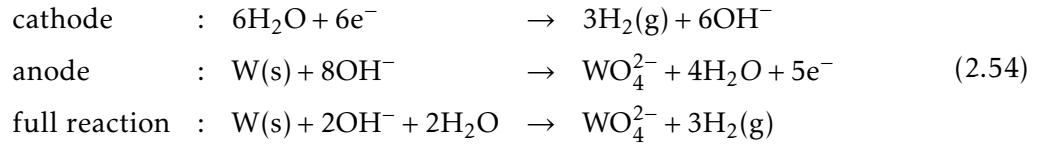
The ionic current etches the dived part of the wire. At the meniscus formed by the wire and the solution a dense layer WO_4^{2-} is formed. Under the effect of gravity, this layer drops and protect the bottom part of the wire. At the bottom of the wire (see Figure **??**). This leads to a faster etching of the wire at the menicus (see Figure **??** (c)). After a while the wire becomes so thin that its tensile strength cannot sustain the weight of the lower part leading to the splitting of the two part. This technique allows for the preparation of sharp tips, which is very important in order to have good and localized contact in the four-points measurements.
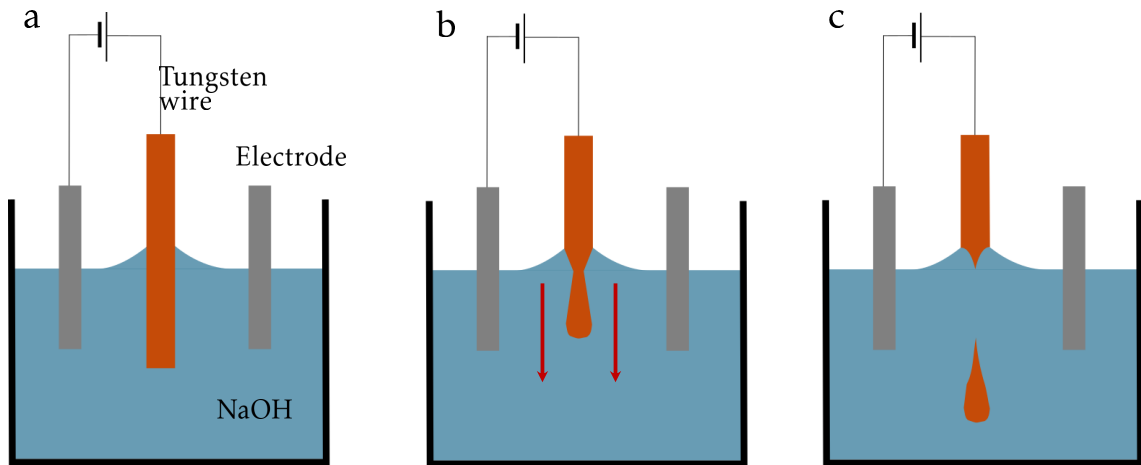
Figure 2.20: Illustration of the tip etching method. a) shows the formation of the meniscus. b) illustrate the flow of WO_4^{2-} towards the lower end of the wire leading to the formation of dense layer of WO_4^{2-} around the bottom of the wire and the necking phenomenon. f) shows the step where the lower part breaks off.

After the electrochimical etching, an oxide layer forms at the tips surface. It is necessary to remove this oxide because it degrades the quality of contacts. Once the tips have been transferred into the UHV chamber, the tips are put in contact with a tantale electrode and a current is injected through the tip in order to anneal it thanks to Joule effect. Typically, tips

are annealed for 45 minutes and currents as high as 2 or 3 amperes are needed to remove completely the oxide layer.

Working principle

The STM technique is very useful for acquiring high resolution images but paradoxically this asset may be a drawback. Indeed, the STM always operates at high resolution making it useless to selectively look for nanostructures that are dispersed over very large areas without being very time consuming [**?**]. For this reason the Nanoprobe is coupled with a SEM placed above the sample and the four tips. Therefore, the low magnification of the SEM allows the direct observation of the tips and their position in real time, avoiding any collision between the different tips. It is also possible to have a quick overview of the sample surface and search for areas of interest whereas STM takes much longer for a single scan with limited sizes of 1 to 2 microns at most. Finally, it makes it possible to look at the shape of the tips used for the contact. As the tips are the central elements of the four-point measurement, their shape may greatly influence the quality of the contact (a big, curved tip may not provide a good ohmic contact). The SEM also facilitates the approach procedure of the tips. In this regard, two steps are required to approach safely the tips on a surface :

Coarse approach : The four tips are first brought (by eyes or thanks to a CCD camera) under the SEM. Subsequently, the tips are approached with the help of the electronic system while visually controlling their position with the SEM. The control of the tip-sample distance is made by manipulating the working distance of the SEM, thus by focusing the electron beam on the tips, and comparing it to the working distance of the sample. With this approach, the tips can quickly be approached at a distance of 50 μm maximum. Under this distance the risk of crashing the tips becomes too high.

Fine approach : Once the tips are sufficiently close to the surface, the final approach is made thanks to the STM control system. The user sets the feedback loop parameters and polarizes the tip. If the tip is too far from the surface no tunnel current can be detected. When the fine approach is launched, the piezo tube along the z axis lowers the tip until a tunnel current is detected. If the piezo reaches its maximum extension without detecting any current, the piezo withdraws the tip and the feedback loop is turned off. Then the STM controller lowers the tip with the coarse motors on a distance smaller than the minimum to the piezo extension in order to avoid any risk of collision between the tip and the surface. After this the feedback loop is reactivated and the piezo lowers the tip again. This procedure is repeated until a tunnel current is detected allowing for a safe and controlled approach of the tips.
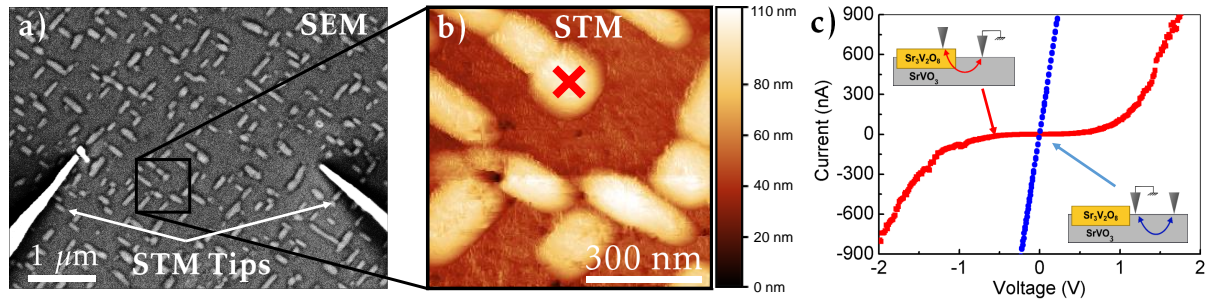
Figure 2.21: (a) SEM image (5 μm × 4 μm; 5 kV) of $Sr_3V_2O_8$ nanorods grown on the SVO matrix together with two STM probes. (b) STM image (-1.5 V, 600 pA) of the area highlighted by a square in the SEM image. (c) I(V) curves taken with a tip in contact with the SVO matrix (blue) or on a $Sr_3V_2O_8$ nanorod (red). For each measurement the reference ground was fixed by an additional probe connected to the SVO matrix. Figures taken and adapted from [?].

Contact of the STM tips on a nanostructure : The combination of the MEB/STM is nicely illustrated by Figure **??**(a) where nanostructures of $Sr_3V_2O_8$ grown upon a strontium vanadate perovskite (SVO) matrix are investigated. The SEM allows to approach the tips without damaging them and to place them over a selected nanorod above the surface. Then the tips are brought in the proximity of the surface. Subsequently, a STM image is performed in order to precisely select one nanostructure (Figure**??**(b)), position the tip above the nanostructure and contact it. Thank to this approach the electrical behavior of one individual nanostructure can be investigated (Figure**??**(c)). This example illustrates the capability of the Nanoprobe to investigate the transport properties of nanostructures. While only two tips where used in this example, usually four tips are used to performed four-point measurement in any area of interest of the sample.
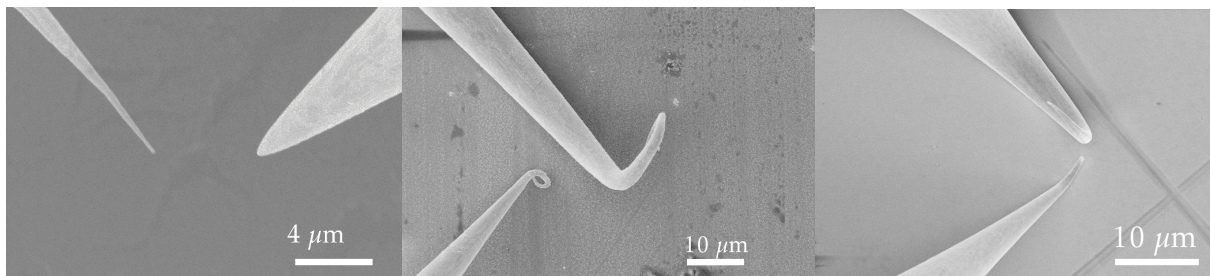
Figure 2.22: a) SEM images of two tips above a metallic surface. The left tip shows a sharp shape adequate for resistance measurement while the right is too big. b) Example of bended and twisted tips. c) SEM images of tips that crashed into the surface and bent. Because they are bent it is difficult to identify which part of the tip is contacting the surface.

Control of the tip shape : As mentioned above the SEM allows for a direct control of the tip shape. This point is crucial in order to perform good resistance measurements. Figure **??**

(a) shows two tips with significantly different apex diameter. The right tip is clearly too big, making it inadequate perform four-point measurements with small probe spacing. If the tips are too severely damaged it becomes impossible to perform good ohmic contact between them and the surface. Figure **??** (b) and (c) show examples of twisted tips. In Figure **??** (c) the two tips are in contact with the surface, but because they are damaged it is difficult to accurately identify the are of the tips that is contacting the surface.

2.4   Conclusion

This chapter discussed the basic principles and operating of the STM. Theoretical background describing the quantum tunnelling effect between two electrodes has been introduced. The exponential dependence of the tunelling current with the tip-sample distance make possible the acquisition of STM images with atomic resolution. STS technique allowing to probes the density of states and electronic configuration of a sample was presented. In a second step, the principle of the four-point measurement and its variation at the small dimension were discussed as well the different possible tip configurations, before presenting the multi-probe STM technique.

Chapter 3

Scanning tunneling spectroscopy of square PbSe QD superlattice on gold substrate

Quantum dots (QDs) solids composed of colloidal nanocrystals have been extensively investigated in the past decade. These artificial solids are of high interest due to the use of QDs as elementary building blocks in the composition of ordered assemblies [?]. Many types of QDs, with different composition, size or shape, can be incorporated in a QDs solid. Moreover by adapting the QD size one can change the band gap providing this class of material considerable tunability and versatility. In these solids, the QDs are usually separated by inorganic capping molecules that create a tunneling barrier limiting the mobility of the charge carrier [?]. Chemical strategies such as ligands exchange have been implemented to reduce the ligands size improving the carrier mobility up to 5 - 20 cm^2/(V.s) [?, ?, ?, ?]. But, so far, the deposition techniques such as spin-coating or dropcasting have led to the formation of disordered arrays of QD, lacking long range order [?].

More recently, superlattice of QDs with individual dots epitaxially connected through covalent bonds have been synthesized. These superlattices exhibit long range order over hundred of nanometers [?, ?]. But surprisingly, mobilities as low as 2× 10^{-2} - 0.1 cm^2/(V.s) [?, ?] have been reported in such materials. Whitham *et al* showed that carrier transport in epitaxial superlattice of PbSe QDs still involves hopping of localized carriers from dot tot dot due to disorder inherent in such self-assembly of QDs [?].

Structural analysis of epitaxial superlattice has been reported to explain the underlying mechanism that linked disorder on the local arrangement of the QD and the superlattice disorder [?]. But experimental evidence and characterization of the local electronic properties of these materials are still lacking. While optical spectroscopy may give some information in that regard, it is still limited as it inherently involves transitions between two energy levels and

does not individual energy levels. On the other Scanning Tunneling Spectroscopy (STS) can provide these information. It has showed to be a reliable technique to investigate the properties of individual [?, ?] and arrays of QDs [?, ?].

Recently, Walravens *et al* [?] showed that the mobility and overall structural order of epitaxial superlattice of PbSe QDs could be greatly improved by thermally treating the QD film. Following this procedure, we investigate by STM and STS the local electronic properties of PbSe QDs superlattice, before and after annealing it.

A solution of nearly monodisperse PbSe QDs with a truncated shape and a 5.8 nm diameter was prepared by reacting lead oleate and trioctylphosphine selenium according to literature procedure [?]. In a second step, the superlattice formation was triggered at the ethylene glycol-air interface by the injection of aniline into the subphase (see Figure **??**). This step induces a striping of all the native Pb-oleate ligands from the (100) facets of the QDs, thus exposing the underlying stoichiometric PbSe facets. This leads to the epitaxial connection of the QDs and to the formation of a square geometry superlattice [?]. The reaction occurs within 30 minutes at room temperature. Then the as-synthetised superlattice was transferred to a gold substrate or a carbon grid by the Langmuir-Schaeffer deposition technique (see Figure **??**). The samples were synthesized and provided by the group of Zeger Hens at Ghent university.
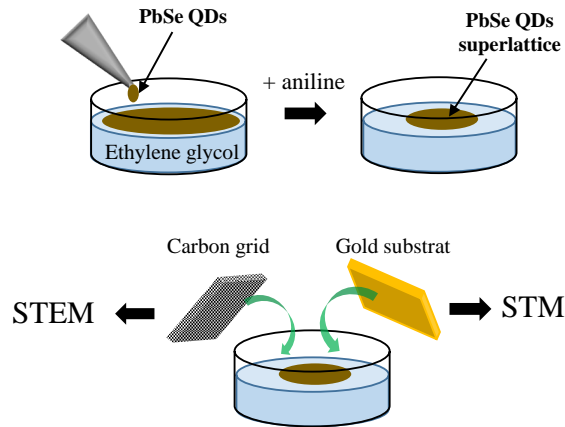
Figure 3.1: Illustration of the superlattice formation and of its transfer on various substrates

3.1 Scanning Transmission Electron Microscopy (STEM) images of PbSe QDs superlattice

In order to check the arrangement of QDs, the QDs superlattice was deposited on a STEM grid and investigated by Scanning Transmission Electron Microscopy (STEM). The STEM images were recorded with a FEI Titan Themis operated at 300kV. The STEM images were obtained by Ahmed Addad at UMET (Lille University). In STEM, an electron beam is accelerated with a

high voltage (300 kV in our case) and focused on the sample thanks to magnetic scanning coils. The electron beam crosses the sample and images are formed by collecting scattered electrons with an annular dark-field detector. It is also possible to perform Electron Energy Loss Spectroscopy (EELS) mapping of the superlattice as shown in Figure **??**.

Figure **??** A confirms the epitaxial connections of PbSe QDs through the (100) facets, creating a superlattice with a square geometry. This is consistent with the ligand stripping triggered by the addition of aniline during the synthesis. The EELS mapping (Figure **??** (B) and (C)) shows the distribution of lead and selenium atoms over a few connected QDs. The two elements are equally distributed over the core of the QDs and the atomic bridge (necking) connecting the QDs. Figure **??** (A) shows the STEM image of three perfectly attached QDs with full and homogeneous atomic bridges between the QDs. On these high-angle annular dark-field imaging (HAADF) STEM images, each white dot corresponds to an atomic column. Here they are separated by 6.12 Å which corresponds to the atomic lattice of PbSe. We attribute the blurry area on the side of the QDs to the remaining ligands still attached on the (111) facets. The interaction between the focused electron beam and these inorganic and non crystalline species results in these blurry stains.

Figure 3.2: STEM High-angle annular dark-field imaging (HAADF) images of 5.8 nm PbSe QDs after aniline treatment (A). (B) and (C) Electron Energy Loss Spectroscopy (EELS) mapping of on the same area as (A) revealing the equal distribution of Pb and Se over the superlattice. (D) overlay of lead and selenium mapping. Scales bar are 5 nm.

Unfortunately, the perfect alignment showed in Figure **??** (A) is not systematic to the superlattice. Typically, self assembly of QDs into a superlattice gives rise to structural disorder

of various nature. In Figure **??** are shown recurrent defects, such as the missing connection between the dots (red arrow in Figure **??** (A)). Poor alignment of the atomic lattice of the QDs during the formation of the superlattice can lead to the formation of dislocations. This is shown in Figure **??** (B) where the atomic lattice orientation of the QDs on the right does not align with the atomic lattice of their left neighbors. This results in a dislocation in the superlattice and a strain into the QDs at the grain boundary. Size dispersion can also be a factor of disorder as it may lead to voids in the arrays and create missing connections between QDs as illustrated in Figure **??** (C).

Figure 3.3: STEM High-angle annular dark-field imaging (HAADF) images of 5.8 nm PbSe QDs after aniline treatment. (A) Example of perfectly connected QDs. Scale bar is 2 nm. (B) Dislocation in the superlattice originating from the misalignment of the atomic lattice of the QD. Scale bar is 5 nm. (C) Example of a significantly smaller QD leading to missed connections. Scale bar is 5 nm.

Moreover at the opposite of Figure **??** (A) the atomic column are not always visible on STEM. Indeed, when the QDs are slightly tilted at least partially toward the $\langle 110 \rangle$ directions, it results in a loss of periodicity in one direction in the atomic resolution STEM image.
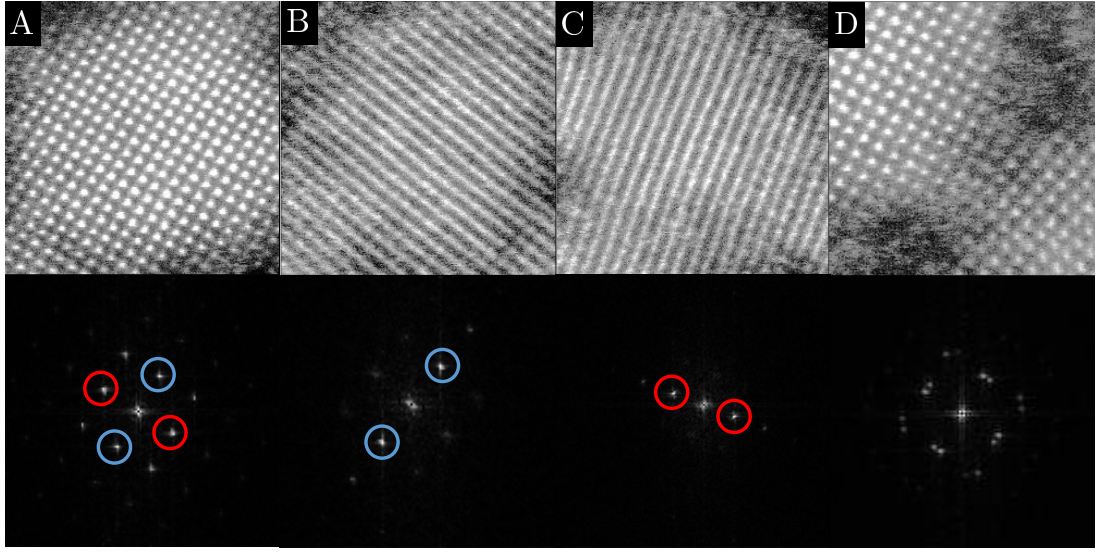
Figure 3.4: Disorder in the atomic lattice of QD superlattice. QDs are either aligned in the out-of-plane direction (A) or tilted toward <111> (B) or rotated toward <110> (C). (D) show the connection between two QDs at a grain boundary. The two atomic lattices are clearly misaligned.

The QDs can also be tilted from the out-of-plane direction by rotating toward the <111> or the <110> directions. This is illustrated in Figure **??** where three QDs STEM images and their associated Fast Fourier Transform (FFT) are shown. Figure **??** (D) illustrates the misalignment of the atomic lattice between two QDs. The FFT clearly shows two orientations separated by a small angle.

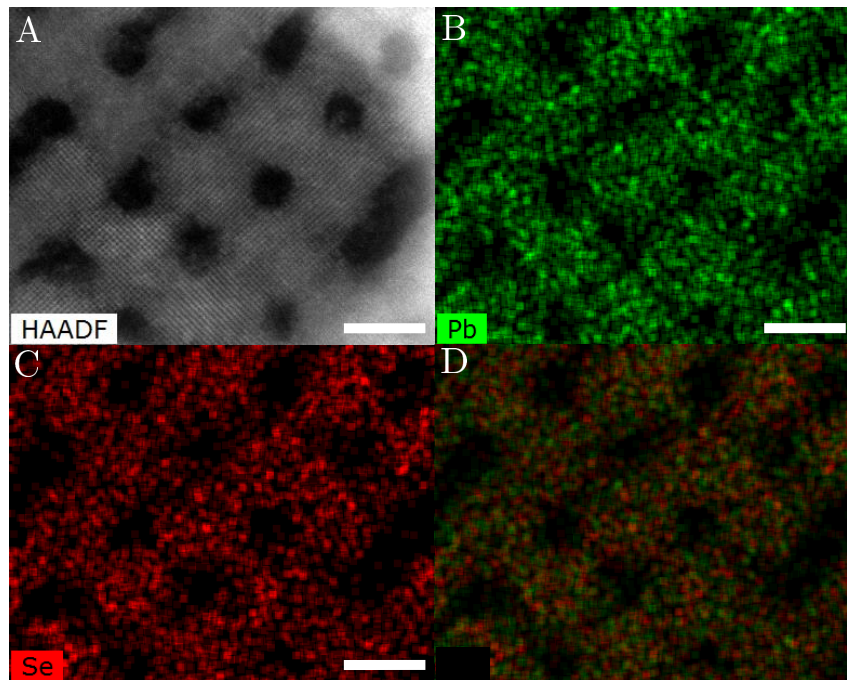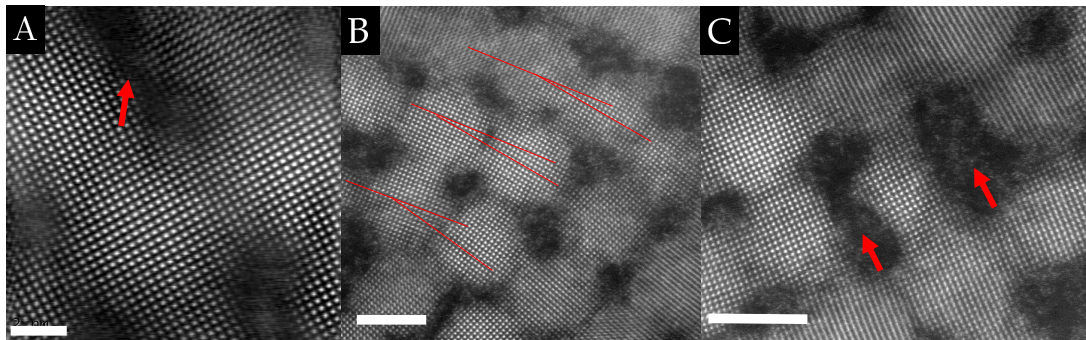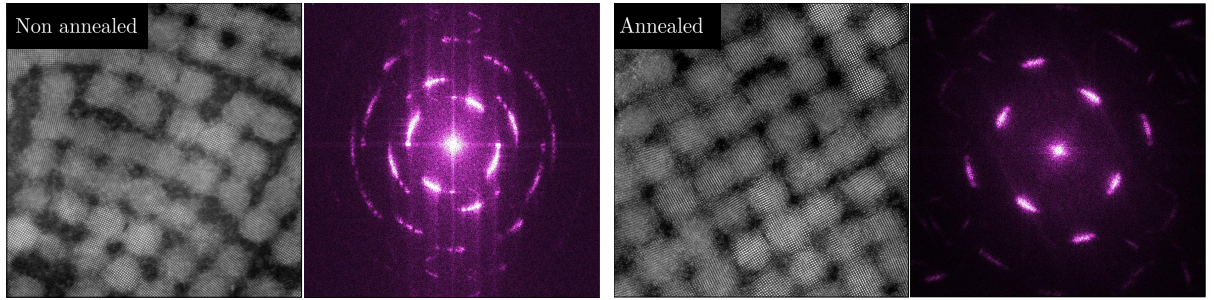**Figure 3.5:** STEM High-angle annular dark-field imaging (HAADF) images of 5.8 nm PbSe QDs after aniline treatment. Left : STEM image of the as-synthesized array and its associated Fast Fourier Transform (FFT). Right : STEM of the annealed array and its associated FFT.

In order to improve the structural properties of the superlattice, the sample has been annealed for one hour at 120°C. Two STEM images, taken before and after the annealing, are shown in Figure **??**. The STEM images of the as-synthesized sample exhibits an important disorder and a plethora of structural defects such as defects in the necking between QDs, misalignment of the atomic plane, or random orientation of the QDs are visible. Moreover, the associated FFT clearly shows a strong dispersion of the QDs orientation. On the other hand, the STEM image of the annealed superlattice taken on another region shows significant improvement in the overall order the QDs, as shown by the FFT. Unfortunately, missing connection

and tilted QDs are still present after annealing the sample.

3.2 STM images of PbSe QDs superlattice

Following the synthesis, the sample was loaded into an ultra high vacuum (UHV) system containing a low-temperature scanning tunneling microscope and characterized at nitrogen temperature (77K). Sharp tungsten tips obtained via chemical etching of a tungsten wire in NaOH solution were used. STM images of the QDs were acquired in constant-current mode with typical sample bias voltages and tunneling currents in the range of +2.5-5 V and 5-50 pA. The differential conductance spectra were acquired by positioning the tip above a selected QD after imaging the superlattice (see Figure **??**(A)). Subsequently, the STS measurements were performed by recording the current and its associated derivative dI/dV while the tip-substrate voltage is swept with the feedback loop open. The dI/dV spectra were acquired using a Signal Recovery lock-in amplifier with a frequency of 480 Hz, a variable modulating amplitude between 7 and 9 mV/RMS and a variable RC time constant between 10 and 20 ms. A large number of curves with identical spectroscopic parameters were acquired (typically 100 spectra) for each QD probed, attesting the excellent stability of the measurements. After this experiment the sample was annealed at 150°C for 1 hour and new measurements were performed subsequently.
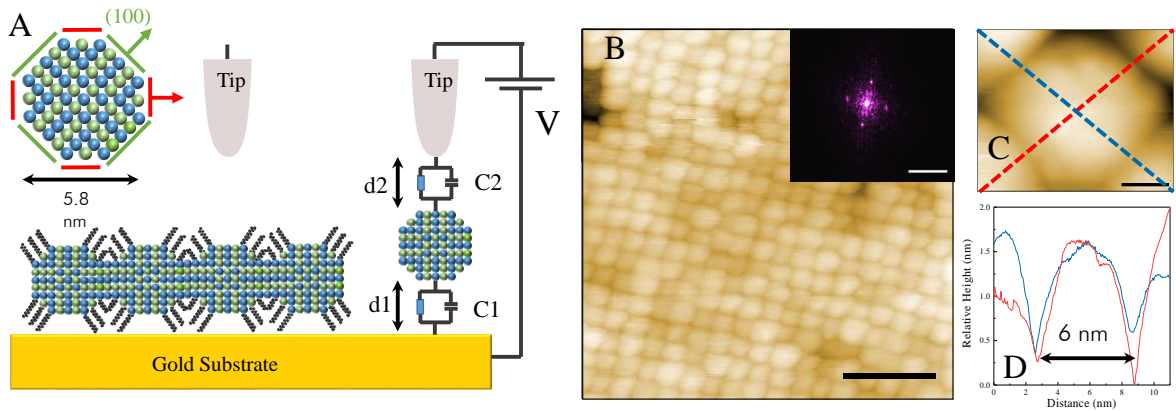
Figure 3.6: (A) Schematic of the sample and the experiment configuration. On the right the equivalent circuit of the Double Barrier Tunneling Junction (DBTJ) related to the tip/QD/substrate system is shown. (B)STM image of the PbSe nanocrystal superlattice transferred onto an Au substrate by the Langmuir-Schaeffer deposition technique after annealing. (Set-point current 10 pA and bias voltage +5V). Scale bar is 20 nm.

Images of the superlattice were successfully acquired using STM. It was easier to perform STM scan after the sample was annealed. This may be due to the desorption of ligands when heating the sample under UHV. For example, a constant current height images of a monolayer of PbSe QDs superlattice with square geometry after being annealed is shown in Figure **??** (B). From the STEM images shown previously it is clear that the QDs were connected with atomic bridge with no ligands in between them. Thus the center-to-center spacing of the FFT associated with the STM image (Figure **??** (B)), yields a direct measurement of the average QD

size. An average center-to-center spacing (or dot-to-dot distance) of 5.81 nm is found. This value is consistent with the mean size obtained by STEM. Therefore, it is possible to determine the size of an individual QD directly from a high resolution STM image, since there is no free space between the QDs. For example, Figure **??** (C) shows a single QD with its size directly obtained from the height profile of Figure **??** (D).

3.3 STS measurements on as-synthesized PbSe QD superlattice

After imaging the superlattice by STM, the tip can be positioned above any selected PbSe QD. STS measurements are done first on the as-synthesized sample right after introducing it in the UHV chamber. Differential conductance spectra taken on five different QDs across the arrays are shown in Figure **??**. The spectrum shown in Figure **??** (A) exhibits classic characteristics of a single QD with discrete peaks on both side of a Zero Conductance Region (ZCR) with the Fermi level positioned in the middle of this ZRC. However, the others spectra shown in Figure **??**, present more diversity in their electronic features, such as the position of the Fermi level, the ZCR or the peaks voltage positions. For example, (B) and (E) spectra have their respective Fermi level close to the peaks at positive bias, but in spectra (C) and (D) the Fermi level lies closer to peaks at negative bias. Moreover, if spectra (A) exhibits a clean ZCR, the spectra (D) and (E) reveal a series of peaks inside this region. These in-gap states most probably originate from trap states.
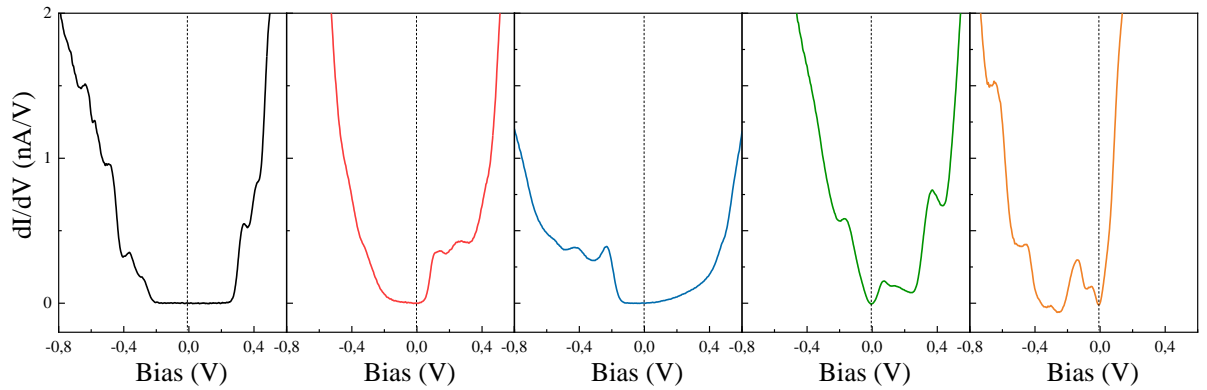
Figure 3.7: Different differential conductance spectra acquired on five different QDs across the as-synthesized array at a temperature of T = 77K. The diversity in the QDs spectra is representative of the inhomogeneous overall behavior of the sample.

The as-synthesized sample reveals plethora of different spectra and an inhomogeneous overall behavior. From the STEM images previously shown, we attribute this variability to the observed disorder, especially the faulted interfaces of some QDs necking (see Figure **??** (D)) and other defects that could lead to the creation of trap for the charge carriers. Figure **??** shows two examples of trap states in STS spectra acquired on two different QDs. The I(V) curve of Figure **??** (A) exhibits a peak inside what should normally be the ZCR, near +0.3V. The associated differential conductance shows a negative differential behavior indicating transport through a

single quantum states. Such a state could be caused by a trap residing at the surface of the QD [?]. On the dI/dV spectra of Figure **??** (B) we can easily identify the two peaks surrounding the usual ZCR around +0.45V and -0.3V. But a careful inspection of the ZCR reveals the presence of smalls peaks within this region. Figure **??** (C) shows a zoom of the ZCR of Figure **??** (B) where such mid-gap states are visible, suggesting again the presence of deep trap states..

The presence of numerous traps states within the gap of the QDs could originate from surface traps due to the removal of the remaining surface Pb-oleate ligands from the (111) facets or could be caused by defects at the interface between two misaligned QDs (see Figure **??** (D)). However, Walraven *et al* showed that careful thermal treatment of these QDs superlattice could improve faulty interfaces and increase the carrier mobility by one order of magnitude [?]. In that regard, we investigated the electronic properties of the QDs in the same sample after annealing it at 120°C for one hour in UHV.
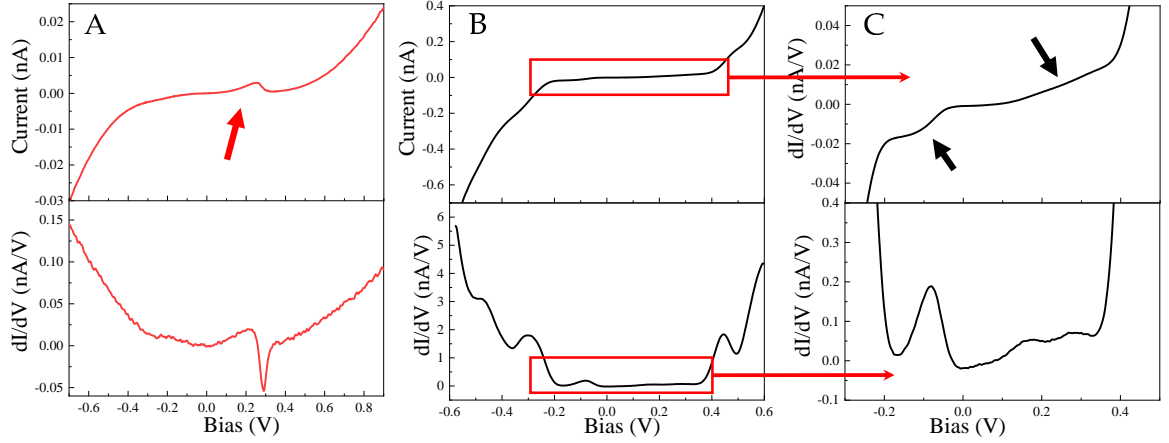
Figure 3.8: Current-Bias curves and their associated differentials conductance spectra measured on two different QDs. The I(V) curve in (A) exhibits a clear peak around 0.3V. (C) shows a zoom in the gap region of the I(V) and dI/dV of (B). The peaks present in (C) are attributed to trap states. The different peaks in the band gap are pointed out by arrows.

3.4   STS characterization of annealed PbSe QD superlattice

After annealing the sample shows a much steadier and reproducible behavior. For a large majority of the spectra a ZCR surrounded by sequence of peaks at positive and negative bias have been observed. A representative example is given in Figure **??**. These conductance peaks are caused by the charge carriers through the discrete levels of the QD. This behavior is characteristic of isolated QDs [?] or weakly coupled QDs and contrasts with the predicted band formation [?] that would have rather given rise to step like DOS. The spectra shown in this figure was obtained by averaging over one hundred spectra as a mean to reduce the signal to noise ratio. All these spectra are shown in Figure **??** (B), where a two dimensional representation of

the one hundred consecutive spectra is presented. This illustrates the stable and reproducible behavior of the tunneling resonances.

Moreover, this behavior was found to be very reproducible across the PbSe superlattice. In order to illustrate this fact, six spectra acquired on QDs located in different areas of the sample are shown. The high number of QDs exhibiting the same behavior (see Figure **??** (C)) contrasts with the inhomogeneous behavior of the as-synthesized sample previously studied. This confirms that annealing the superlattice leads to a more homogeneous overall behavior in the electronic properties of the QDs.

In order to get quantitative information about the broadening of the tunneling resonances and determine if coupling does indeed occur between the QDs in the superlattice, we need to determine the nature of these resonances and calculate the lever arm characterizing the voltage distribution across the DBTJ. In this regard, two spectra have been acquired on the same QD with increasing setpoint currents (see Figure **??** (A)). All the peaks, on both sides of the ZCR, clearly shift towards negative voltage. Each peak at positive bias shifts towards lower voltage value, unlike what is normally expected if electron tunnel through the ground state of the conduction band [**?**]. Thus we can identify the two peaks surrounding the ZCR as the hole ground state h_1 contributing on both sides of the ZCR.
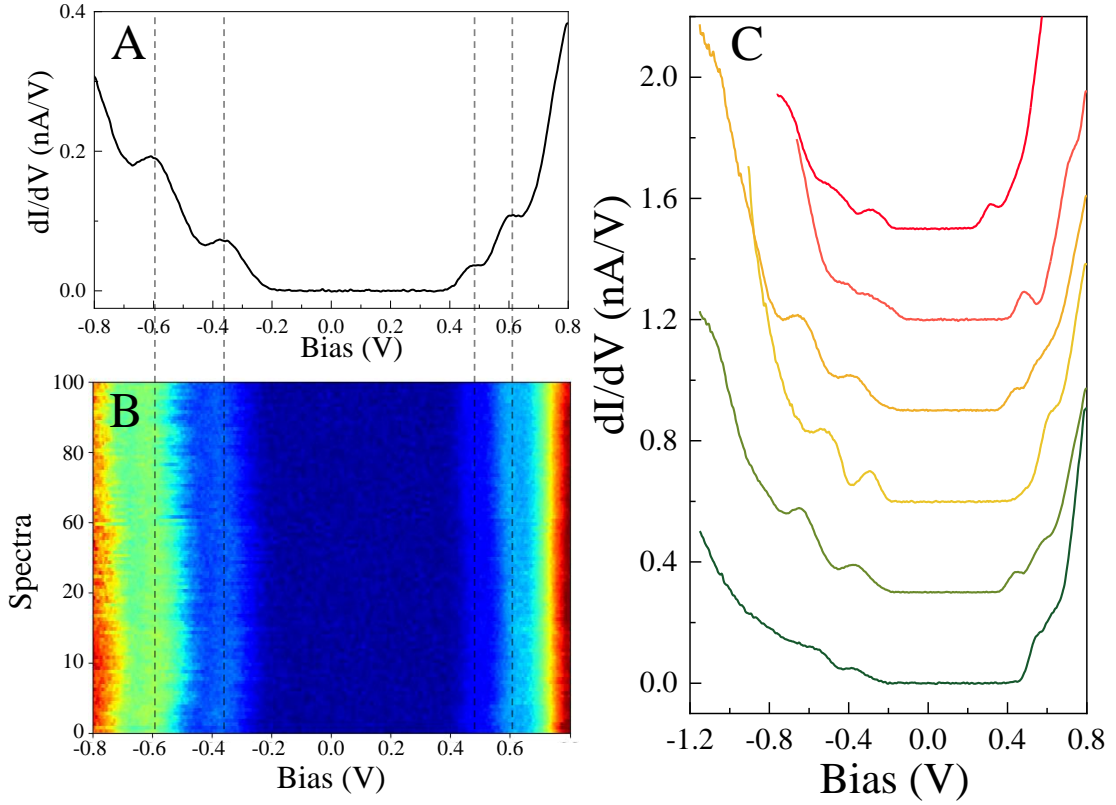
Figure 3.9: (A) Tunneling spectrum measured on a QD with a diameter of 5.8 nm. (B) Two dimensional visualization of the one hundred consecutive spectra averaged to obtain the spectrum in (A), demonstrating the stability of the measurement. (C) Tunneling spectra acquired on six different QDs , with the same setpoint current of 200 pA at a bias voltage of +0.8V. These spectra present a clear ZCR with peaks on both sides, showing the characteristic behavior of an isolated QD.

The peculiar tunneling regime where the hole ground state contributes to tunneling on both sides of the ZCR is call unipolar hole tunneling. This regime occurs in the case of a symmetric double tunneling barrier junction [?], where the capacitance C_2 of the tip-QD junction is of the same order of magnitude as C_1 the capacitance of the QD-substrate junction. It means that the lever arm η characterizing the DTBJ approaches 0.5. Moreover, if the Fermi level in the QD is not positioned midgap, then the same state can contributes on both sides of the ZCR. Here the Fermi level lies close to the valence states suggesting a p-type doping. This observation is consistent with transport measurements reported on similar superlattices [?]. The tunneling processes occurring in this system are depicted in the Figure **??** (C) and (D) where the tunneling trough the first hole level at positive and negative bias are schematized. At negative bias (Figure **??** (C)) hole tunneling through the valence level happens. At positive voltage the hole ground state moves above the substrate Fermi level, before the electron ground state becomes aligned with the tip Fermi level. (Figure **??** (D)). Therefore it contributes a second time to a tunneling resonance but this time, at positive bias.
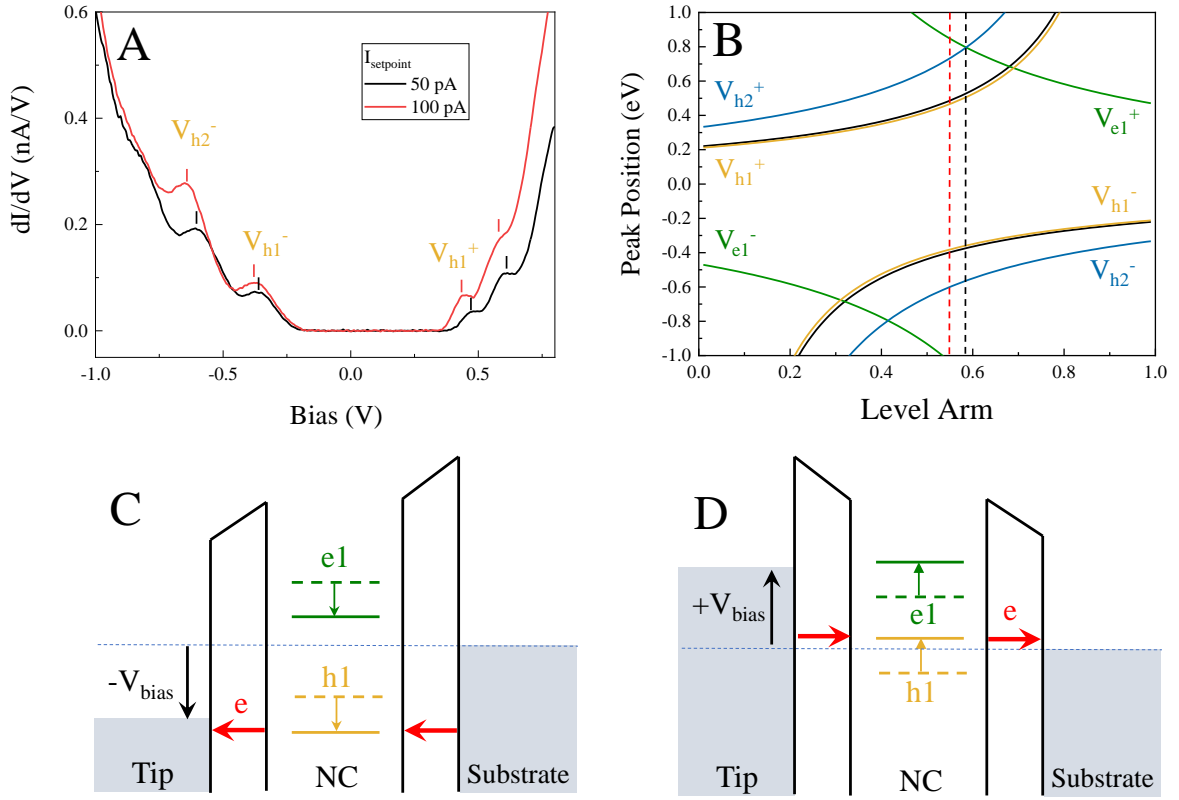
Figure 3.10: (A) Scanning tunneling spectroscopy measurements acquired on the same QD at two different setpoint currents. The shift towards negative bias of all the peaks at higher setpoint current indicates the presence of a hole tunneling on both sides of the gap.(B) Variation of the peak position as function of the lever arm η. We assume a QD with a diameter of 5.8 nm, yielding a band gap of 0.68 eV. This band gap correspond to the apparent band gap measured at a lever arm of 1. $V_{h_1}^+$ and $V_{h_1}^-$ correspond to the hole ground state at positive and negative bias, $V_{h_2}^+$ and $V_{h_2}^-$ to the hole first excited level and $V_{e_1}^+$ and $V_{e_1}^-$ to the electron ground state. The black curve correspond to the peak caused by the charging of the hole ground state, $V_{2h_1}^+$ and $V_{2h_1}^-$. The vertical dashed lines corresponds to the lever arm obtained for the setpoint currents of 50 and 100 pA. The two down panels show schematics of the tunneling process trough the first level of the valence band at negative (C) and positive (D) bias.

Quantitatively, the variation of the peak position with the setpoint current depends on several parameters such as the lever arm η or the polarization energy Σ. Typically, η has to be calculated which introduces some uncertainties. But in the particular case of unipolar tunneling, the lever arm can be accurately determined experimentally. It is experimentally deduced thanks to the equation 1.44 of chapter 2 [?] :

$$\eta = \frac{V_{h_1}^+}{V_{h_1}^+ - V_{h_1}^-} \tag{3.1}$$

Thus a lever arm of 0.58 for the lowest setpoint is found. Then the lever arm decreases down to 0.51 for the highest setpoint. The voltage at which the resonances occur with the hole ground

level h_1 at negative and positive bias are :

$$V_{h_1}^- = \frac{h_1 - E_F - \Sigma}{e\eta} \quad V_{h_1}^+ = -\frac{h_1 - E_F - \Sigma}{e(1-\eta)} \qquad (3.2)$$

Similarly, the voltage corresponding to the resonance with the electronic ground level e_1 are :

$$V_{e_1}^- = -\frac{e_1 - E_F + \Sigma}{e(1-\eta)} \quad V_{e_1}^+ = \frac{e_1 - E_F + \Sigma}{e\eta} \qquad (3.3)$$

Where Σ is the polarization energy and E_F is the Fermi level.

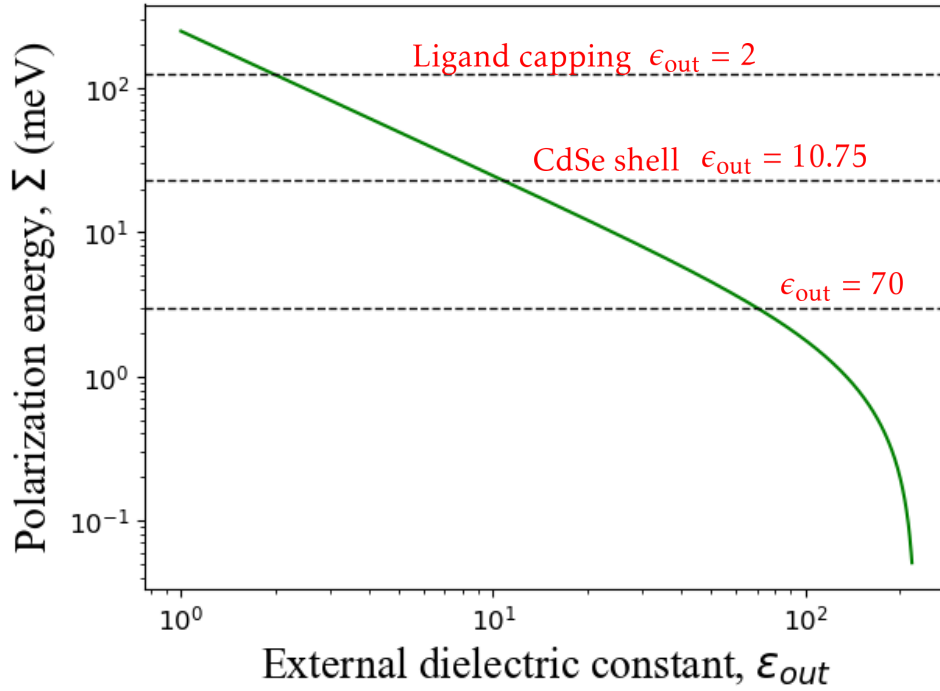Figure 3.11: (a) Evolution of the polarization energy Σ as function of the external dielectric constant ϵ_{out}. The horizontal dashed lines correspond to values of ϵ_{out} typically used in literature, $\epsilon_{out} = 2$ (Ligand capping [?]) and $\epsilon_{out} = 10.75$ (CdSe shell [?]).
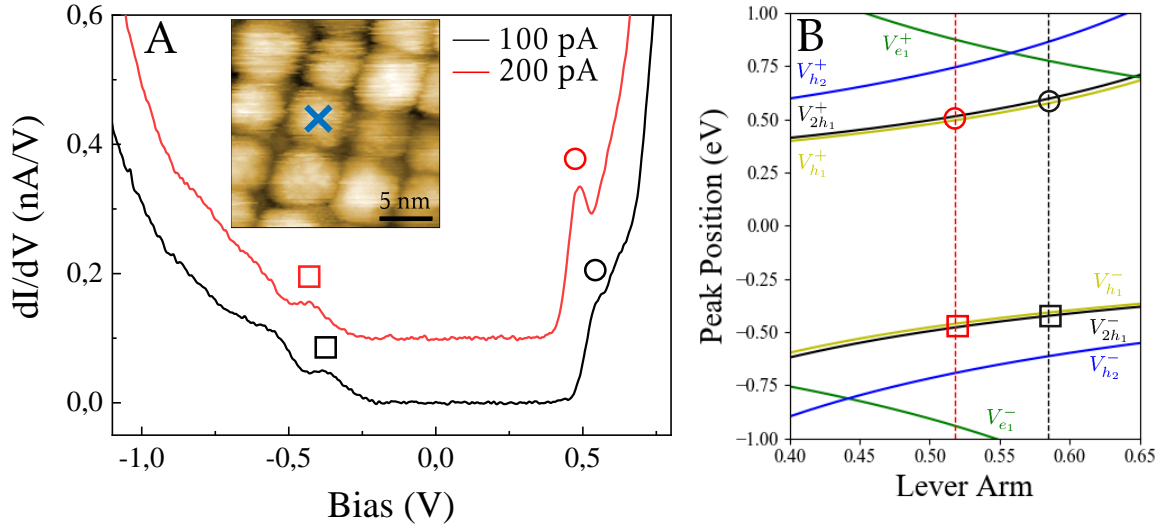
Figure 3.12: ((A) Two spectra measured on the same QD for different current setpoints. From STM image the QD diameter was found to be 5.7 nm. Inset : STM image of the probed QD, (highlighted by the cross); Parameters : +2.5V, 5 pA. (B) Simulated variation the voltage peak position measured in tunneling spectroscopy as function of the lever arm. Calculation are performed for an external dielectric constant ϵ_{out} of 70, i.e., a polarization energy Σ of 3 meV. In parallel, band gap of 0.680 eV was calculated for a PbSe QD with a diameter of 5.8 nm [?].

Knowing the diameter of the QD from the topographic STM image, we determine the theoretical band gap based on tight binding calculations [?]. For a PbSe QD with a diameter of 5.7 nm, the band gap is 0.68 eV [?]. In order to calculate the voltage positions of the peaks, we need to take into account the polarization energy Σ, which is the energy needed to put an additional charge in the valence and conduction levels. This energy is determined by the difference between the dielectric constant of the QD and the dielectric constant of its surrounding, ϵ_{in} and ϵ_{out}, respectively. Based on equation 1.36 of chapter 2, this energy can be written:

$$\Sigma = \frac{1}{2}\frac{e^2}{4\pi\epsilon_0 R}\left(\frac{1}{\epsilon_{out}} - \frac{1}{\epsilon_{in}}\right) + \frac{0.47e^2}{4\pi\epsilon_0\epsilon_{in}R}\left(\frac{\epsilon_{in} - \epsilon_{out}}{\epsilon_{in} + \epsilon_{out}}\right) \tag{3.4}$$

While ϵ_{in} is known in the case of PbSe with $\epsilon_{in} = 227$, evaluating ϵ_{out} in the present case is challenging since the QDs are surrounded by others QDs, vacuum and remaining ligands. For an isolated PbSe QD with a size of 5.8nm covered with its native inorganic ligands ($\epsilon_{out} = 2$ [?]) the polarization energy can be calculated to be 125 meV. On the other hand, an isolated PbSe QD with similar diameter but covered with a thin CdSe shell ($\epsilon_{out} = 10.75$ [?]), Σ is estimated to be 23 meV. In our system, the PbSe QDs are located inside an array of other PbSe QDs on a metallic surface. Therefore, the dielectric mismatch should be far less important than in the two cases mentioned above, leading to a smaller polarization energy. The evolution of the polarization energy as function of the external dielectric constant is plotted in Figure **??**(A) for a PbSe QD ($\epsilon_{in} = 227$). We start by considering QDs with a non truncated cube shape with six facets. In this case two facets are exposed to the vacuum while the four others facets are exposed to the neighboring PbSe QDs. This yields a mean external dielectric constant $\epsilon_{out} =$

$(4/6) \times 227 = 151$. In our experiment however, the QDs have a truncated cube shape with a relative neck width of 0.6 [?, ?] which lowers the ϵ_{out} mean value. From this simple model we estimate an external dielectric constant $\epsilon_{out} = 151 \times 0.6 = 90$.

We tried to estimate a value of ϵ_{out} more precisely. In this regard, a set of spectra, shown in Figure ?? (A) were acquired on the same QD for an increased setpoint current. The peak positions of $V_{h_1}^-$ and $V_{h_1}^+$ were measured from Figure?? (A). Subsequently the lever arm was calculated from equation ??. Then equation ?? was used to determine the evolution of the ZCR as function of the lever arm for different ϵ_{out}. A good agreement was found between equation ?? and $V_{h_1}^-$ and $V_{h_1}^+$ for an external dielectric constant ϵ_{out} of 70. This high dielectric constant value is reasonable considering our system, as described above. Moreover this value is close to the one estimated from the simple geometrical model used previously. The result is shown in Figure ??(B). For this value of ϵ_{out} a polarization energy value of 3 meV is calculated from equation ??.

Since the value of the lever arm clearly indicates a symmetric Double Tunneling Barrier Junction, shell-filling should occurs. The energy needed to inject another electron inside the QD (also called repulsion energy J_{e-e}) depends on the external dielectric constant ϵ_{out}. Based on equation 1.39 of chapter 2, this energy is written :

$$J_{e-e} = \frac{e^2}{4\pi\epsilon_0 R}\left(\frac{1}{\epsilon_{out}} + \frac{0.79}{\epsilon_{in}}\right) \tag{3.5}$$
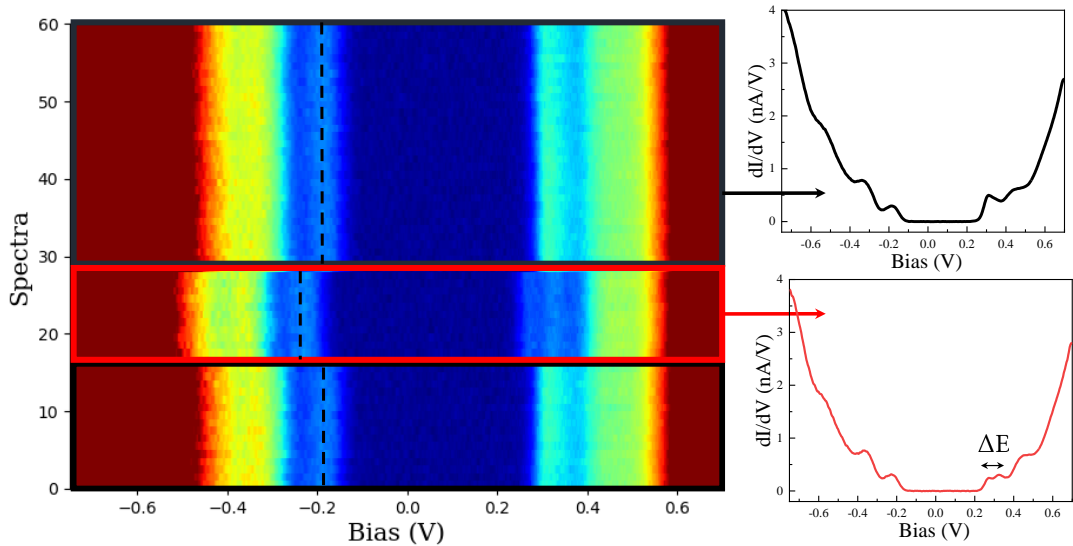

Figure 3.13: Set of 60 spectra taken in a row above a QD in the array. A charging event of the QD occur (red curve) after a while but the charge is released and the QD comes back to its initial state (grey curve).

With our estimation of a large ϵ_{out}, this repulsion energy has a low value (J_{e-e} = 9 meV for ϵ_{out} = 70). Thus, the dielectric mismatch between the internal and external dielectric constant being far less important than in the isolated QD case, it it favorable to inject a new electron without too much energy. Surprisingly, the spectra does not show any doubling of the peak, hallmark of the injection of a second charge carrier inside the QD, characteristic of the shell-filling regime. This means that two carriers are never simultaneously present inside the QD. Therefore, in addition to evacuate the charge carrier through the substrate, the charge carrier must find an other way to leave the QD. A likely path could be the hopping to the next neighbors suggesting again a coupling between the QDs.

One could argue that the low J_{e-e} energy is below the resolution limit achievable in STS because the peak-peak voltage modulation is larger than 9meV in our experiments. The peak in Figure **??** with negative polarization is, for example, very wide and could contain two very close peaks. However, because the DTBJ is symmetric ($\eta \sim$0.5), J_{e-e} have the same value for the two peaks on both sides of the ZCR. If some charging were to occur, the peaks at positive and negative bias should have similar width since they would both contain two unresolved peaks. However, from Figure **??** it is clear that the peak at positive bias is systematically and significantly thinner. Thus the broadening of the peak with negative polarization cannot originate from the presence of two unresolved peaks due to the injection of a second hole in the QD.

Occasionally we could find temporary charging of the QDs as illustrated in Figure **??** where a second charge carrier becomes trapped inside the QD but manages to escape after a while. The doubling of the lowest peak at positive bias is a sign of the presence of a second charge carrier in the quantum state. This charging locally modify the potential resulting in a shift of 40 mV between the red end grey curves (see dashed lines on the left panel of Figure **??**). The splitting voltage on the lowest peak at positive bias ΔE is also of 40 mV. By converting this repulsion energy by the lever arm and using Equation **??** an external dielectric constant of ϵ_{out} = 27 is found. This value is lower than our estimation. We attribute this lower ϵ_{out} to missing connections of this QD with its neighbors modifying the surrounding of the QD (see Figure **??** (C)). This would also explain why the QD is charging since the charge has more difficulties to escape by hopping to the nearest neighbors. This ϵ_{out} value is still very high in comparison of the literature value cited earlier, confirming the lower dielectric mismatch in our system. The explanation of charging occurs at positive bias only is given in the following section.
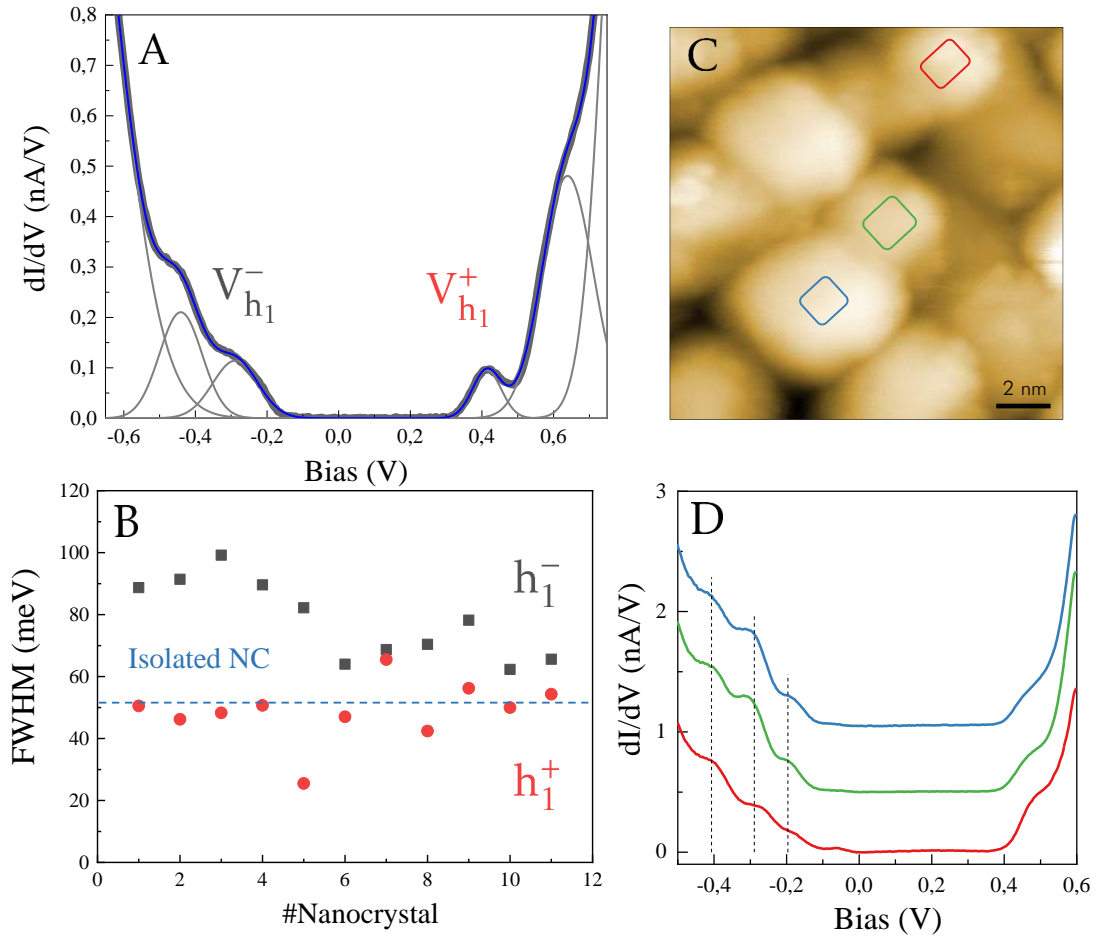
Figure 3.14: (A) Full Width Half Maximum of the peaks V_{h1^+} and V_{h1^-} were obtained by fitting the resonance peaks with gaussian functions. (B) Statistical graph of FWHM normalized by the lever arm of the first level at positive bias (V_{h1}^+) and at negative bias (V_{h1}^-) for a tenth of QDs. The blue line represents the FWHM of V_{h1}^- for an isolated PbSe QD with a diameter of 5.8 nm (from [**?**]). (C) STM image acquired for a bias of +2V and a setpoint current of 10 pA. (D) dI/dV spectra (Iset = 100 pA) of the 3 individual QDs shown in the STM image in (C). Vertical dash line are guide for the eyes.

In order to determine the degree of coupling between the QDs and get a quantitative measure of the broadening of the density of states, Gaussian functions were fitted to the peaks of the spectra (Figure **??** (A)). Then we use the value of the lever arm calculated earlier to convert the Full Width Half Maximum (FWHM) of the peaks into energy. Because there is some uncertainty in fitting the higher order resonances, we only use the first resonance to determine the coupling strength. The FWHM of the two peaks surrounding the ZCR were extracted for a dozen of QDs. We only measured the FWHM for QDs which exhibited a clean ZCR, similar to the spectra shown in Figure **??**. The FWHM for an isolated QD of 5.8 nm diameter is 50 meV for h_1 [**?**] and is represented by a blue line in Figure **??** (B). The first valence resonance $V_{h_1}^-$ is found to be significantly larger than the isolated case. The FWHM of these peaks are found to

range between 100 meV to 70 meV. The broadening of $V_{h_1}^-$ indicates that quantum mechanical coupling occurs between the valence states of the nearest QDs. On the other hand the lowest peak at positive bias $V_{h_1}^+$ has a similar width as the isolated QD. This indicates that at positive bias the electron tunnels through a decoupled, discrete state. At positive bias, due to the p-type doping level, the stronger electric field which is applied to reach h_1, electrostatically decouples the first valence state. This explains why the charging shown in Figure **??** occurs in the first peak at positive bias. Therefore the difference of broadening of the two peaks surrounding the ZCR gives us a clear validation of the coupling of the valence level in our sample. While a few QDs exhibit a coupling strength (defined as the extra broadening of the density of states) around 50 meV, others show moderate coupling with a coupling strength between 20-30 meV.

Sometimes, QD spectra exhibit the characteristic signs of a band transport hence very strong coupling over several QDs. Figure **??** (C) shows the STM images of such QDs. Examples of spectra with step-like features are shown in Figure **??** (D) where the peaks at negative bias are significantly broadened. Remarkably, all the QDs display the same feature in the STS spectra that consists in a clear step-like DOS in the valence band. It strongly suggests the formation of a band within this cluster of QDs. Thus very locally the QDs can connect in such a way that their respective quantum states couple and allow the delocalization of the electron over a few QDs. Unfortunately these spectra were clearly observed in minority. Nevertheless, this proves that band-like transport occurs on the local scale and that strong coupling between QDs could be enhanced by thermal treatment of the superlattice.

A second behavior was also observed among the QDs as shown in Figure **??**. A set of six spectra acquired on six different QDs over the superlattice (Figure **??** (A)) attests of the reproducible occurrence of a peak just above the Fermi level. The peak is positioned around +0.07V. For every spectrum, over one hundred consecutive spectra were averaged as depicted in Figure **??** (C). Again the whole spectrum structure is very stable and reproducible, even for the in-gap state clearly indicating that this is not an artifact. The nature of this peak can be attributed to surface traps originating from the removal of surface Pb-oleate ligands from the (111) facets of the QDs. The (100) facets are stochiometric and it has been shown that these facets do not bear dangling bond states in the energy gap due to the *p*-like nature of the electronic states [**?**]. In contrast, the (111) facets are not stochiometric and thus the removal of ligands can lead to surface trap states. The removal of the Pb-oleate could also explain why the sample is heavily p-doped. This interpretation of the trap nature of in-gap state could explain the low mobility reported on similar PbSe QDs superlattice [**?**]. However, since the Fermi is still close to the valence band, at this stage, we cannot rule out the possibility that this state originates from the degeneracy of the hole ground state with the Fermi level penetrating inside the valence band.
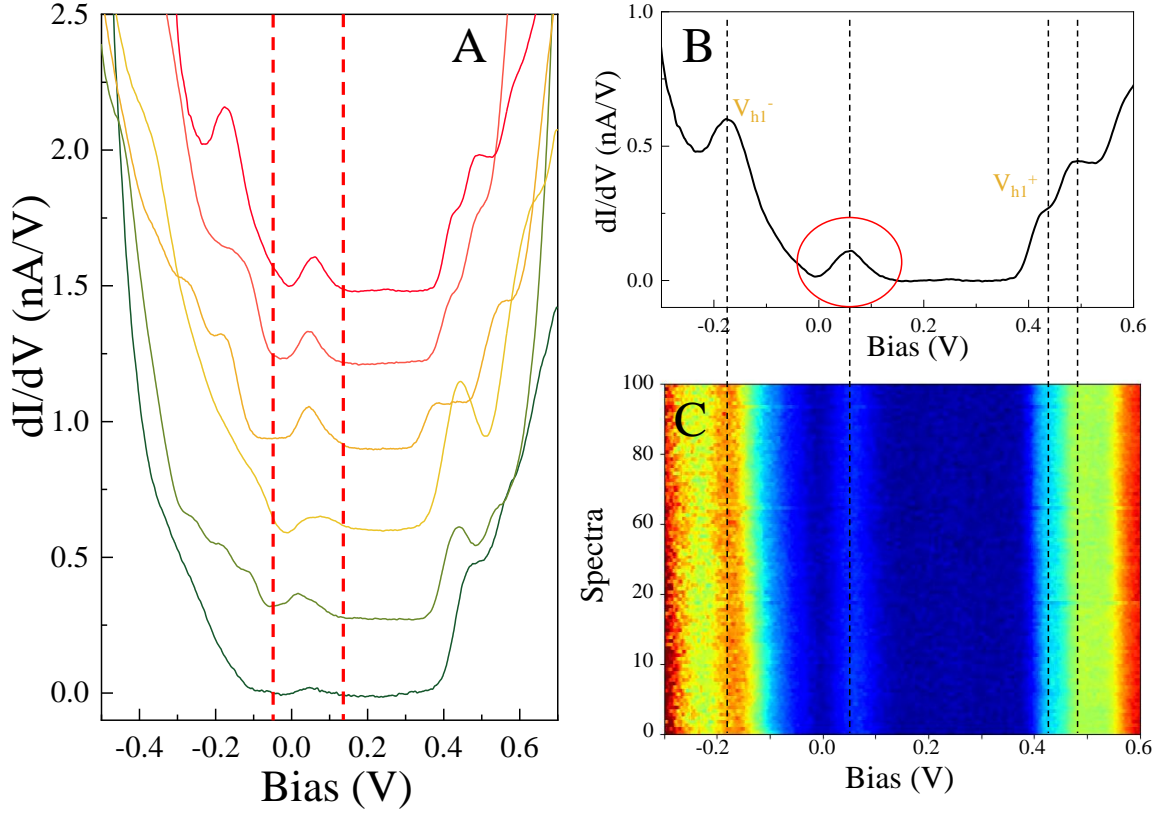
Figure 3.15: (A) Tunneling spectra acquired on six different QDs, all exhibiting peak in the gap around +0.07V. The spectra were acquired with the same setpoint current 200 pA at a bias of +0.7V (B) Tunneling spectrum measured on PbSe QD obtain after averaging the one hundred spectra show in (B).

3.5 Conclusion

In this chapter the electronic properties of PbSe superlattice were investigated before and after thermal treatment of the sample. The as-synthesized sample exhibits the presence of a large variety of spectra. The peaks seen around zero volt are attributed to traps states inside the gap of the QDs, . We believe that they are caused by strong structural disorder. Indeed the square symmetry of the superlattice is far from being perfect with misalignment of the QDs, resulting in the formation of dislocations and missing connections. These misalignments also create faulty interfaces which we assumed to be responsible for most of the trap states. Annealing at 120°C allows to cure the QDs since it clearly improves the homogeneity of the spectra. Measurements of the electronic structure of the superlattice demonstrate that quantum mechanical coupling occurs between the valence states of one QD and its neighbors. Moreover band-like features has been observed in a few spectra showing that strong coupling occurs very locally. These results are encouraging and demonstrate the necessity of a better understanding of the underlying mechanism leading to the formation of the superlattice.

Chapter 4

Scanning tunneling spectroscopy characterization of PbSe QD superlattice deposited on silica substrate

In the previous chapter, STS measurements have been performed on a PbSe QDs superlattice deposited on a gold substrate. Two reproducible behaviors were observed among the annealed QD superlattice. While most of the studied QDs exhibited a clean zero conductance region, a minority showed a peak localized inside this zero conductance region near the Fermi level. So far, the origin of the peak is unsettled. It could be caused by trap states in the gap of the QDs or could arise from a higher doping level in some QDs. In such a case, the Fermi level would be positioned in the valence band and as a result would contribute to the signal at small positive sample bias, giving rise to a peak above the Fermi level. In this chapter we address the exact nature of this peak by changing the host substrate, so that the double tunnel barrier junction becomes more asymmetric, enabling us to reverse the potential distribution across the junction in comparison with the gold substrate. In such a way, the lever arm reaches values below 0.5 and allows to expand the energy scale to get more insight into the origin of the peak.

4.1   Experimental details

The QDs superlattice studied in this section were prepared in Ghent based on the synthesis method previously described in Chapter 3. For this experiment, the QD superlattice was subsequently deposited on a silicon substrate thanks to the Langmuir-Schaeffer deposition technique. Prior to the deposition of the superlattice, a thin film of $1 \sim 2$ nm of SiO_2 was deposited on the wafer. This thin oxide layer was added in order to increase the potential drop between the QDs and the substrate. Due to this important modification of the potential distribution among the DTBJ, a very small lever arm can be reached. It is therefore possible to dilate the

energy scale and get a higher resolution when performing STS experiments, enabling in depth investigation of the nature of the in-gap states shown in the previous chapter. The superlattices were additionally treated after deposition on the SiO_2 surface, in order to remove any residual ligands. This was done by exposing the sample to butylamine solutions. This ligand stripping was performed to allow a better stability of the STM tip and make the STM experiments less challenging. An illustration of the sample geometry is shown in Figure **??** (A). The lever arm was estimated from the equivalent circuit model shown in Figure**??** (A). The lever arm is defined by $\eta = C_2/(C_1 + C_2)$. Therefore, by taking a tip-QD distance of 3 - 4$\mathring{A}$ and a silica dielectric constant of $\epsilon_{SiO2} = 3.9$, a lever of 0.36 is estimated.
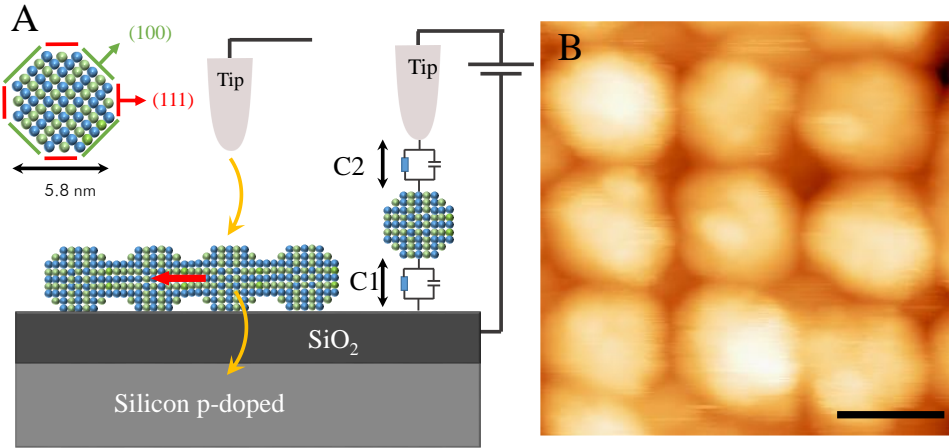
Figure 4.1: A) Scheme of an individual QD where facets are indicated and principle of the STM imaging of PbSe superlattice deposited on a silicon substrate with a 1 nm silica layer on top. On the right the equivalent circuit of the DBTJ related to the tip/QD/substrate system is shown. B) STM image (I_{set} = 25 pA; V = +2.5V) of a superlattice showing the close-packing of PbSe QDs in a square superlattice. The scale bar is 5 nm.

Immediately after sample preparation, the sample was transferred into the UHV system of the LT-STM. The sample was characterized at helium temperature (T = 5K). We used electrochemically etched tungsten tips, annealed in the UHV preparation to get clean and stable STM apex. The topographic images were acquired in constant current mode (see Figure **??** (B)), with typical feedback loop parameters being : a setpoint current in the range 10-50 pA and a sample voltage between +1.5 and +2.5 V. Similarly to the previous chapter STS experiments were performed by first scanning an area of interest and subsequently placing the STM tip above the desired QD. Then the voltage sample was swept with the feedback loop open while the tunnel current I was measured as function of the voltage V. The differential conductance spectra were simultaneously measured using a lock-in, amplifier, with a variable modulation amplitude between 7 and 9 mV/RMS at a frequency of 480 Hz.

4.2 STM images of the PbSe QD superlattice

Despite a small oxide barrier, STM images of the PbSe superlattice were successfully acquired. These images are obtained in the constant current mode so the tunneling current is maintained by adjusting the height, z, of the tip by a feedback loop. In Figure **??**, a STM image of the QD array (150×150 nm^2) is shown. The visible square packing of the the QDs was found to be consistent over the whole image. From the STEM images shown in the previous chapter it was demonstrated that the QDs were atomically connected and that no ligands remained in-between the QDs. Therefore the average dot-to-dot distance (or center-to-center spacing) can be deduced from the FFT shown in the inset of Figure **??**. An average dot-to-dot distance of 5.81 nm was found, which is consistent with the QD size found in the previous chapter. We note some disorder on the local scale, as vacancy or missing connection between QDs (see red circles in Figure **??**). A careful inspection of the color contrast reveals height variation (between 0.8 to 1.4 nm, see height profile in Figure **??**). While most of these height difference originate from size dispersion of the building blocks, we find that the variation of the contrast cannot be explained by a change of size only.
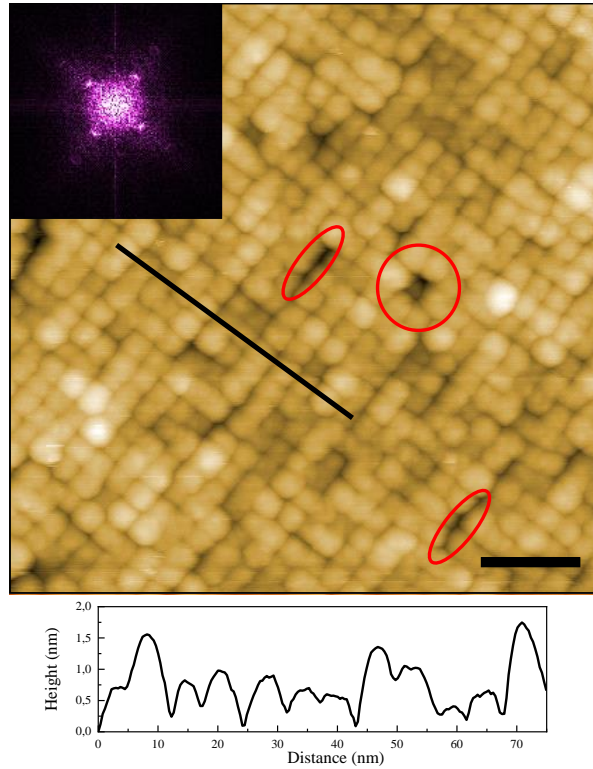
Figure 4.2: Large scale STM images of the PbSe superlattice. The superlattice shows a square geometry extending over 150 nm. The red circles highlight defects in the superlattice such as missing connections and vacancy in the array. Bottom: height profile taken along the black segment. Inset : FFT of the STM image. Feedback loop parameters : $I_{set} = 50$ pA; V = +2 V. The scale bar is 25 nm.
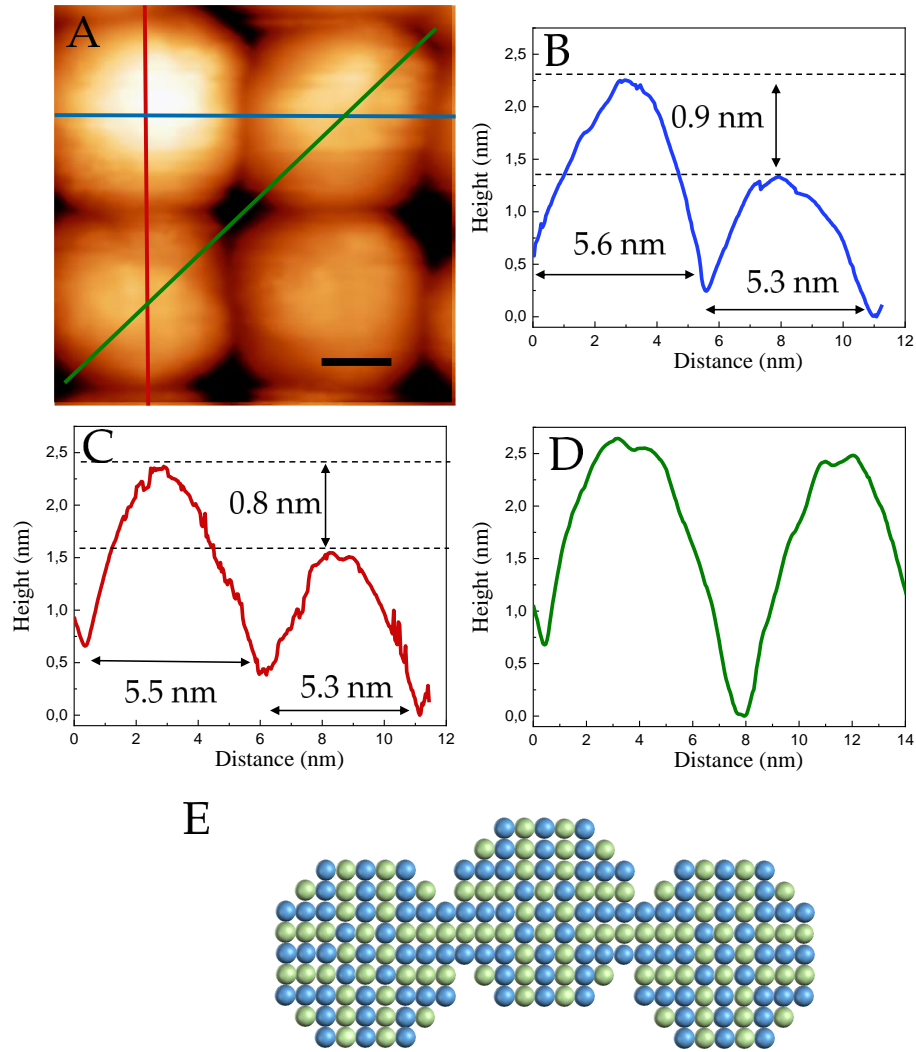
Figure 4.3: (A) High resolution STM images of the PbSe superlattice showing four epitaxially connected QDs. Feedback loop parameters : I_{set} = 25 pA; V = +2.5 V. The scale bar is 2 nm. (B), (C) and (D) relative height profile taken along the different color line in shown in the STM image. (E) Schematic representation of a faulty connection between QDs in the vertical axis.

Figure **??**(A) shows a STM image of four QDs. The top left QD is clearly higher than the others QDs. Since ligands were removed from the QDs surface, the height profile directly gives the height difference between two QD neighbors. The height difference between the top left QD and its nearest neighbors are shown in Figure **??** (B) and (C). From this height profile, height differences of 0.8 and 0.9 nm are found. In comparison, the profile shown in Figure **??** (D) clearly shows two QDs with similar height. In order to determine if this difference is caused by a size difference, we also measured the QD diameter. This is possible because there is no free space between the QDs. As a result, the diameter corresponds to the separation between opposite necks from the profile in Figure **??**(B). The size of the two QDs are 5.6 and 5.3 nm respectively, which yields a size difference of 0.3 nm. Similarly the profile in Figure **??** (C) yields

a size difference of 0.2 nm. These size differences are not sufficient to explain the height difference. Although the left top QD is bigger and could have more electronic states contributing to the tunneling current, implying a larger tip-QD distance in the constant current image, we made sure to image the QDs at a bias high enough so that the variation of the density of states between the QDs is negligible [?]. In both cases the height difference is found to be around 0.6 nm which is close to the lattice constant of PbSe (6.12 $\mathring{A}$). It means that PbSe QDs does not necessarily attach in perfect, symmetric way. Instead the QDs can connect to each other with a small vertical shift as schematized in Figure ?? (E). Therefore, the height information brought by STM topographic mode revealed a new inhomogeneity in the QD coupling that could not be seen in STEM.
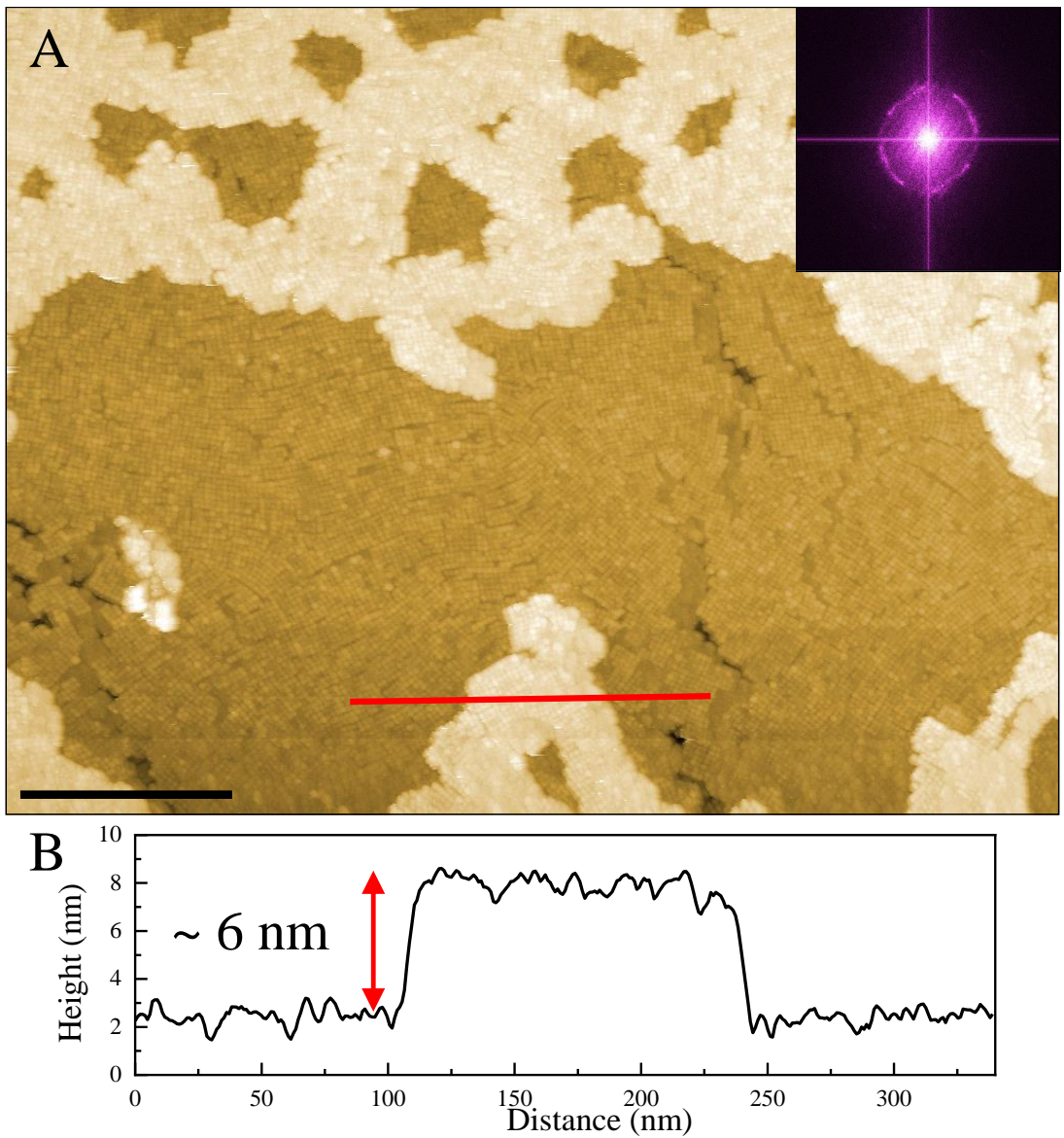
Figure 4.4: (A) Large scale STM images of the PbSe superlattice. Feedback loop parameters : I_{set} = 50 pA; V = +2.5V. The scale bar is 200 nm. (B) Height profile taken along the red line denoted in the topography image.

Zooming out allows to scan over much wider areas in comparison with the gold substrate. We attribute this increased stability to the absence of ligands. The large scale STM image shown in Figure **??** taken over a micron attests of the striking improvement in the scanning conditions compared to the previous chapter. Both monolayer and bilayer are visible in this image. This is confirmed in the height profile (Figure **??** B) taken along the line in the topographic images, where a height of 6nm is found between the brightest and the second layers. This height definitely corresponds to an average QD size of ∼ 6 nm. This is in good agreement with the QDs size found from the FFT (see the inset of Figure **??**). While the superlattice still exhibits locally the square geometry (as shown in Figure **??**) it clearly lacks true long range order. This is due to the dislocations visible in Figure **??** (A) and the cracks in the superlattice. But it can also be due to size and shape dispersion of the QD building blocks and probably also to orientational disorder of the individual QDs. This dispersion in the QD orientation is clearly visible in the FFT (inset of Figure **??** A).

4.3 STS characterization of the superlattice
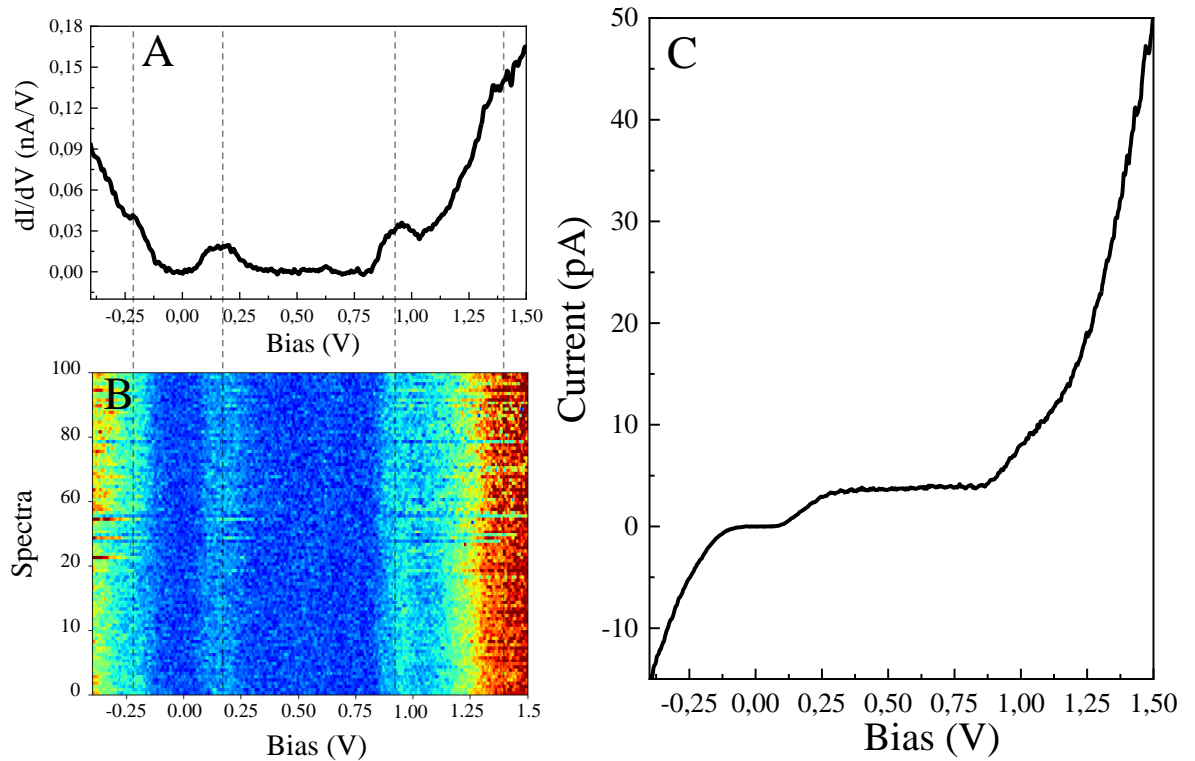
Figure 4.5: (A) Tunneling spectrum measured on a PbSe QD with a diameter of 5.8 nm. Feedback parameters : Bias V = +1.35V; setpoint current I = 100 pA. (B) 100 consecutive dI/dV spectra concatenated into a color map. Vertical dashed lines are guide for the eyes. (C) I(V) curve associated to the differential conductance spectrum.

The spectra were acquired on the QD monolayer. The spectra were found to be reproducible as a hundred of spectra with similar features could be acquired upon a single QD. We note

the existence of small glitches, that do not hinder the averaging process. Figure **??** (A) shows a representative dI/dV spectrum averaged on more than 100 consecutive spectra (see the color map in Figure **??** (B)). The positions of the peaks (and notably the central one) are found to be reproducible. Interestingly the spectrum does not reveal any ZCR. Instead the spectrum exhibits a broad peak located above the Fermi level, centered around +0.2V. Then, a peak is visible near +0.9V.
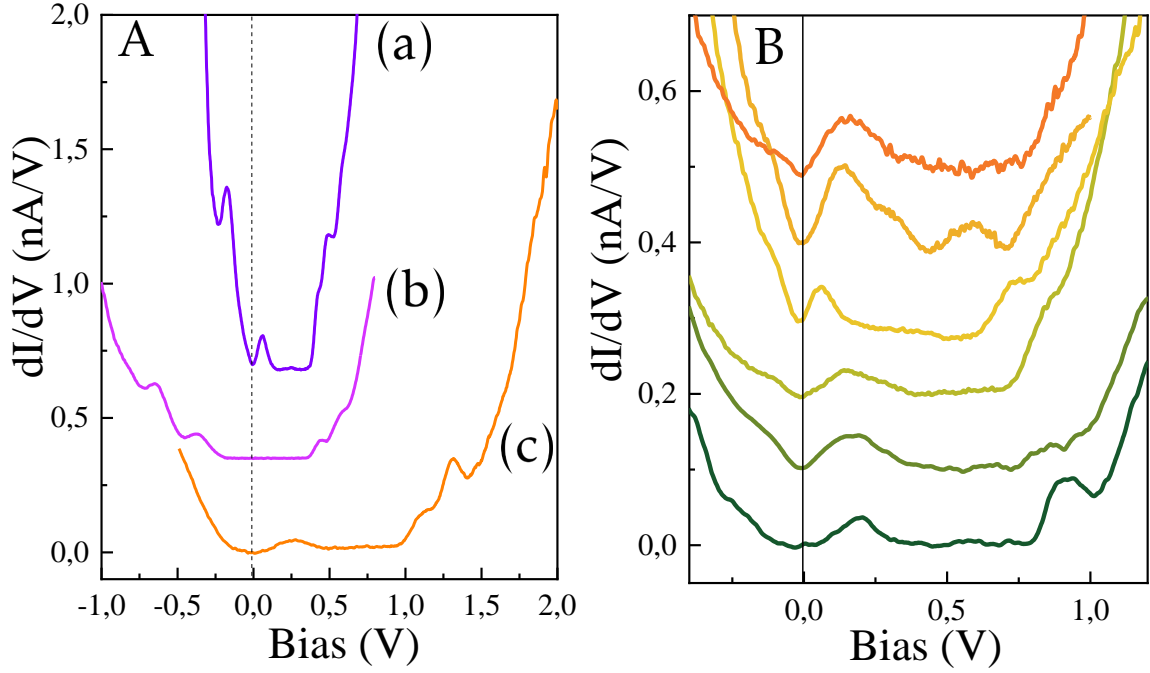
Figure 4.6: (A) Tunneling spectra measured on a PbSe QD with a diameter of 5.8 nm on : (a) and (b) the gold substrate, (c) the silicon substrate. Feedback loop parameters : (a) I_{set} = 100 pA, V = +0.7V; (b) I_{set} = 200 pA, V = +0.8V; (c) I_{set} = 600 pA, V = +2V. (B) Tunneling spectra acquired on six different QDs, with the same setpoint current of 100 pA at a bias voltage of +1.4V. These spectra all present a clear peak near the Fermi level.

Figure **??** (B) shows a set of six spectra acquired on different QDs that show similar features. The main peak above the Fermi level is measured, confirming the reproducible behavior of these spectra. Another example is shown in Figure **??**(A)(c). It is interesting to compare this spectrum with the typical ones measured on the gold substrate (see Figure **??** (A) (a) and (b)). While spectrum (b) shows a clear ZCR, spectrum (a) exhibits a very similar shape and common features with spectrum (c). The same peak located near the Fermi level is present in both spectra while a doublet of peaks is visible at higher voltage. However the energy level separation appears to be much smaller in the case of spectrum (a).

We attribute this difference to the oxide layer between the QD and the substrate. Indeed, the oxide modifies the potential distribution across the two tunneling junctions. Due to the thick tunneling barrier between the QD and the substrate, the voltage dropping over the QD-

substrate junction becomes larger than the ones dropping over the tip-QD junction leading to an asymmetric DTBJ. The lever arm η that characterized the potential distribution is thus expected to become smaller that the one encountered for the gold substrate.
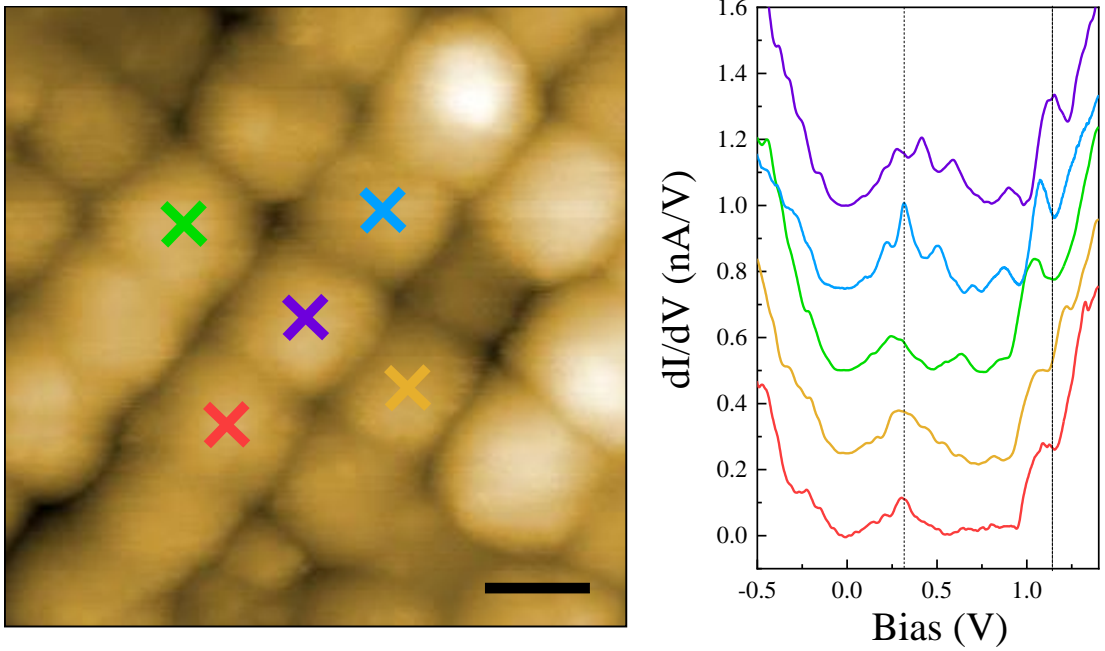
Figure 4.7: Spatially-resolved tunneling spectra of a QDs superlattice area. The spectra were acquired for a setpoint current I_{set} = 200 pA and a bias V = +1.4V. The scale bar is 5 nm.

While the set of spectra shown in Figure **??** were randomly acquired, we also performed spatially resolved tunneling spectra. In Figure **??** a set of five adjacent QDs was probed. All the spectra were acquired with the same sample voltage (V = +1.4V) and the same setpoint current (I_{set} = 200 pA). Apart from minor differences, all the dI/dV spectra interestingly show the same characteristics, with a peak positioned around + 0.3 V, close to zero bias, corresponding to the Fermi level of the sample. Then a second peak is positioned around +1.1 V. These characteristics are similar to the spectra already shown in Figure **??**, confirming the reproducible behavior of these spectra over the sample. However, one can notice that the shape of the central peak slightly differs from one QD to another. For example, the red spectra exhibits a narrower peak than the blue and violet ones. The two top spectra (blue and violet) show a sequence of additional small peaks superimposed to the main one. Moreover the position of this central peak also differs slightly. This is visible by looking at the dashed line in Figure **??**. The peak of the green spectrum is localized at lower voltage while the top violet one is shifted at higher bias. The position of the second peak, around +1.1 V, also varies slightly from one spectrum to another (see solid line in Figure **??**). Surprisingly, the position of both peaks seems to be correlated. Indeed, looking at the green spectra, both peaks are positioned at slightly lower voltages than the other spectra. This is the opposite in the case of the top violet spectra.
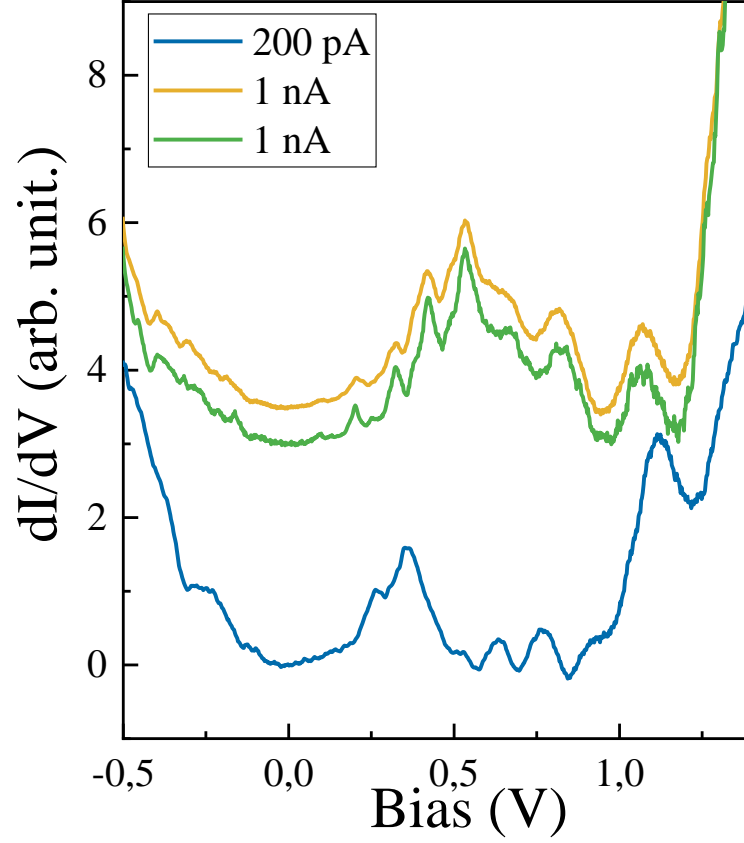
Figure 4.8: Spectra acquired on the same QD at two different setpoint current of 200 pA and 1 nA. The orange and blue spectra were obtained by averaging over 100 curves while the green spectra represents a single spectrum. This shows the sharpness and spacing of the smaller peaks between 0V and +0.5V.

Spectra acquired on the same QD for two different setpoint currents are shown in Figure **??**. At high setpoint current, additional oscillations are visible in the +0.5V - +1V range. Moreover, the central peak located around +0.4V seems to shift towards positive bias, indicating an electron transport through the state, in contrast with the peak seen above +1 V, which corresponds to a hole transport. Remarkably, the progression of smaller peaks between 0V and +0.5V shows equally spacing. They strongly resemble the expected response when the electron level is coupled to phonon modes [**?**, **?**]. The interaction between the confined electron and the lattice vibration leads to the formation of a polaronic DOS. Indeed, in the case of polaronic state, theory predicts a series of equally spaced peaks with a spacing corresponding of the vibrationnally excited states separated by the phonon energy $\hbar\omega$[**?**, **?**].
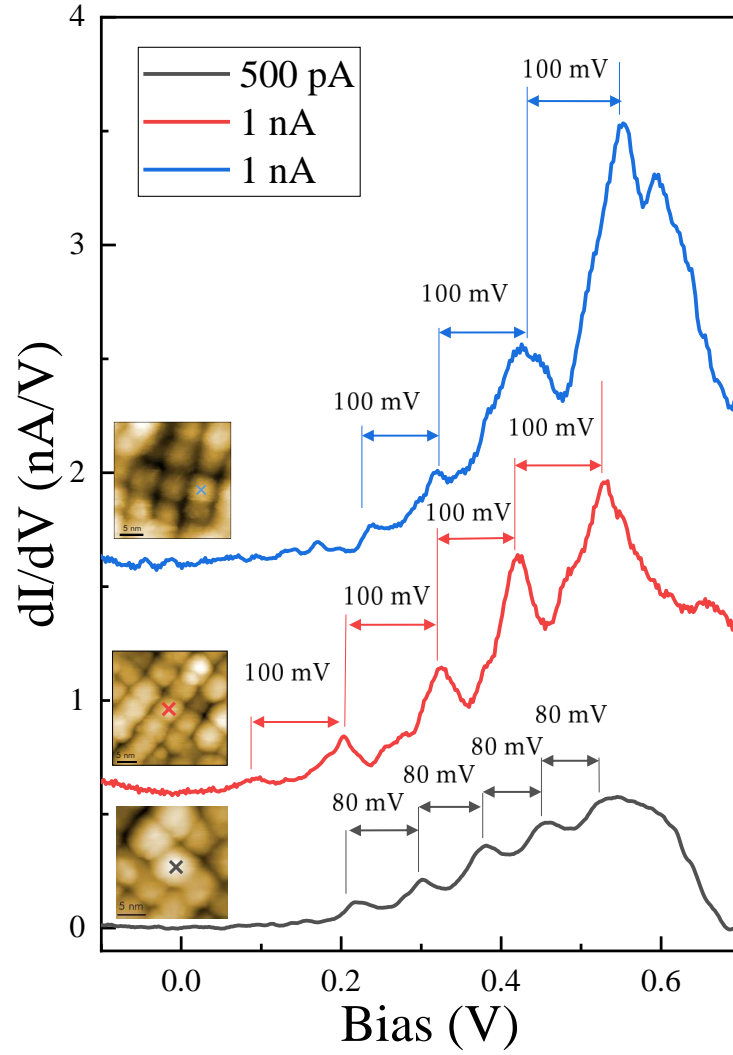
Figure 4.9: Example of three STS spectra acquired on different QDs for a high setpoint current. Each spectrum exhibits small and equally spaced series of peaks attributed to polaron eigenstates. In inset are shown the STM images of the corresponding QDs.

Three examples of spectra showing such polaronic states are represented in Figure **??**. The peaks spacing is found to be dependent of the setpoint current. This is due to the change in the lever arm since the tip to QD distance is not always the same and we expect some fluctuations of the SiO_2 thickness. In PbSe, the energy of the LO phonons modes is about 17 meV [**?**, **?**]. Therefore, by measuring the peak spacing from Figure **??** and comparing to this LO modes enrergy, ones can find the lever arm :

$$\eta = \frac{E_{LO}}{E_{STM}} \tag{4.1}$$

From the above equation a lever arm ranging between 0.17 and 0.21 was calculated for the two different setpoint currents. This estimation of a very low lever arm is coherent with our geometry.

The measurement of vibronic states usually takes place for very localized states that are electronically isolated from the electrodes. Therefore, we believe that the peak measured between 0.0 and +1.0 V corresponds to a trap state on or in the PbSe QDs. As it is found for every QDs and the main difference of the QDs with the previous chapter is the lack of ligands, we believe that the trap state are created at the surface due to the removal of the ligands. The vibronic states are clearly resolved in the measurements of PbSe QDs on the SiO_2/Si surface for three reasons. First, the substrate is not metallic. At the energy of the trap state, there is no available states in the Si substrate to ensure an elastic transfer of the tunneling electrons. As a result, the electrons can only dissipate part of their kinetic energy before they relax to a state aligned with the unoccupied valence band of the degenerated p-type doped Si substrate or recombine with a hole in the superlattice. Then, the use of a thick SiO_2 layer favors a large potential drop across the QD-substrate junction, yielding a small lever arm, that significantly expands the energy scale, allowing the detection of the whole progression. Finally, given that most of the remaining ligands were stripped thanks to the exposure to additional chemicals, the trapped electron cannot relax its energy by interacting with the softer vibrational modes of the ligands. Therefore, the charge carriers confined in this localized state interact preferably with the lattice vibrations leading to an enhancement in the electron-phonon coupling. Because the transfer rate to evacuate the electron is weak, a negative potential repulsion takes place so that the next energy level occurs at higher energy. So far, we do not have gained enough statistic to know if the peak seen at an energy corresponding to the conduction band edge of the silicon susbtrate correspond to a hole level or electron levels of the QDs. For sure, when the energy levels of the QDs become aligned with the conduction band states of the Si substrate, elastic tunneling is allowed and accounts for a significant increase of the signal above 1 V.
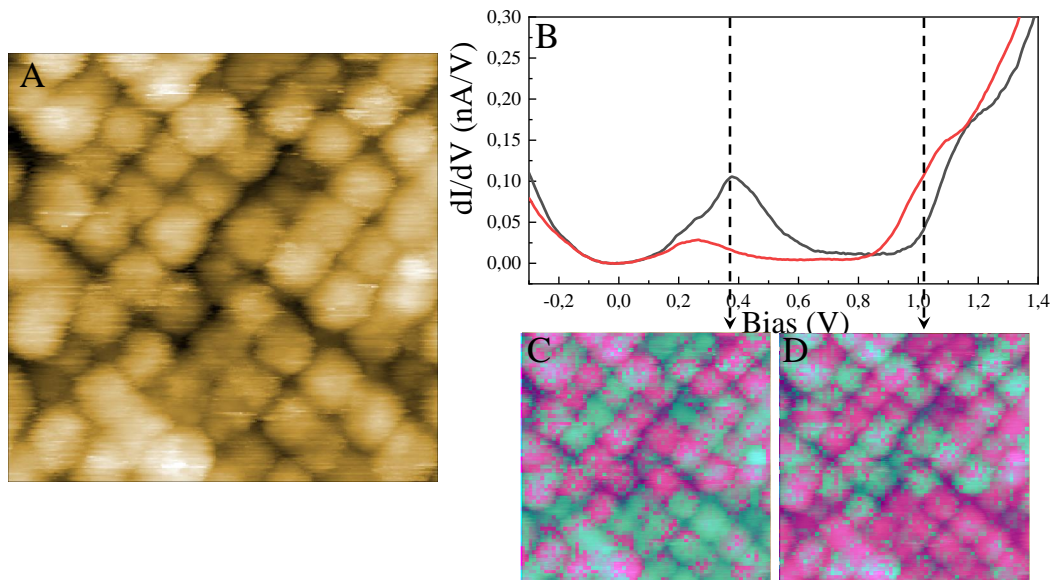

Figure 4.10: (A) Topography associated to the CITS. (B) Two classes of spectra measured among the QDs. (C) and (D) dI/dV maps of the studied area taken at +0.375V and +1.05V respectively.

As the central peak is observed everywhere in the superlattice and has been found to spatially shift between QDs, local spectra measured at constant-tip sample separation were acquired consecutively, following a grid of pixel in a STM image. This technique, called Current Imaging Tunneling Spectroscopy (CITS) allows to spatially resolved the DOS of a sample. This method was performed by acquiring a grid of 64 × 64 grid of spectra simultaneously with the STM images consisting of a grid of 256 × 256 pixels. To ensure the stability of the tip, a constant stabilization voltage was applied to the sample while re-activating the feedback loop. This way the tip height was adjusted to maintain the tunneling current and safely moved to the next pixel.

The result from the CITS is shown in Figure **??**. Here, the CITS was performed on a region of 50 × 50 nm. The topographic STM image is shown in Figure **??** (A). Almost 70 QDs were studied during this experiment. Every single QDs probed during this experiment exhibited a similar shape as the spectrum showed in Figure **??** (B) with a peak close to the zero bias and a second at higher bias near +1V. Interestingly, two trends were observed among the probed QDs. The grey spectrum from Figure **??** (B) exhibited two peaks in the gap and a peak around +1.1 V. The second red spectrum resembles the previous one but with a smaller in-gap peak and another one at +1 V, thus at lower bias than for the previous spectrum. dI/dV maps at +0.375 V (the top of the in-gap paek) and at +1.05V are shown in Figure **??** (C) and (D) respectively. The spatial distribution of the two classes of QDs showed that the QDs formed small equipotential clusters. Therefore the distribution of the trap states in the QDs superlattice creates another source of energetic disorder. We attribute this variation of potential to residual charges in the surroundings, in particular at the surface of the SiO_2 surface, that rigidly shift the energy levels of the QDs, likewise for graphene flakes deposited on SiO_2 [**?**].

Conclusion

In this chapter the topographic and electronic properties of a PbSe QD superlattice deposited on a silicon substrate were investigated. The nature of the in-gap state observed in the previous chapter was analysed revealing the presence of a strongly localized state in the band gap of the PbSe QDs. This trap state most likely arises from the removal of the ligands. The (100) facets of PbSe QDs does not induce in-gap state even when stripped of all there ligands (see previous chapter). Therefore we conclude that these trap states originate from the (111), non stochiometric facets of the QDs which are, without ligands and thus non passivated. We found that the trap states can be used as a sensor of the electrostatic fluctuations at the SiO_2 surface. In order to improve the electronic coupling between the QDs, such fluctuations must be reduced and call for more controlled insulating layers as tunneling barriers. One solution could consist of using thin boron-nitride layers that are known to be much more homogeneous.

Chapter 5

Transport properties of PbSe QDs square superlattice by Multiprobe STM

Early QD solid consisted in QD assembled in a solid phase with each QDs separated from their nearest neighbors by the native surface ligands which cover the QDs during the synthesis. However most organic native ligands act as insulating barrier between the QDs leading to highly insulating QD solid with conductivity of $\sigma \sim 10^{-12}$ - $10^{-9}\Omega^{-1}.cm^{-1}$ [?]. Recently, expitaxially connected QDs superlattice have been prepared. These atomic connections between QDs remove any tunnel barrier between QDs. Therefore, a spectacular enhancement of the charge carrier mobility was expected. Morevoer theoretical calculations have predicted band structure in these materials. Therefore these superlattices promise to combine the tunable optical properties and processability of QDs with the high-efficiency band-like transport of bulk semiconductors. However, charge transport studies have so far failed to demonstrate band-like transport [?, ?, ?]. While missed connection, inhomogeneous coupling between QDs, grain boundary or other structural disorder have been invoked to explain this poor transport properties [?, ?], the problem may arise from the integration of the superlattice into FET device. Indeed, the integration of the QD array to a FET devices is not always perfectly controlled. This results in problematic channel-electrode contact due to the 150 nm height difference between the top of the electrode and the channel (see Figure ??). This surely induces undesirable strain in the QD superlattice that may have a deleterious effect on the transport. Moreover, cracks can appear in the QD thin film, reducing the transport properties.

In order to access the local transport properties of the QD superlattice without being affected by such undesirable problems, we used MultiProbe Scanning Tunneling Microscope (MultiProbe-STM) to study the superlattices in a non-destructive way. The technique relies on a distance-dependent method between the probes in order to measure the four-point resistance of the sample and extract the conductivity of the PbSe superlattice. By considering different arrangement between the probes, we also study the conductance anisotropy in the sample. Based on the structural morphology of the superlattice which is obtained from high resolution SEM, the origin of this conductance anisotropy is explained by the presence of elongated regions of

missing QDs called crack in the QD array. Finally, we quantified the influence of the cracks visible in the QD film by disentangling the crack-free surface resistivity from the crack-induced resistivity.
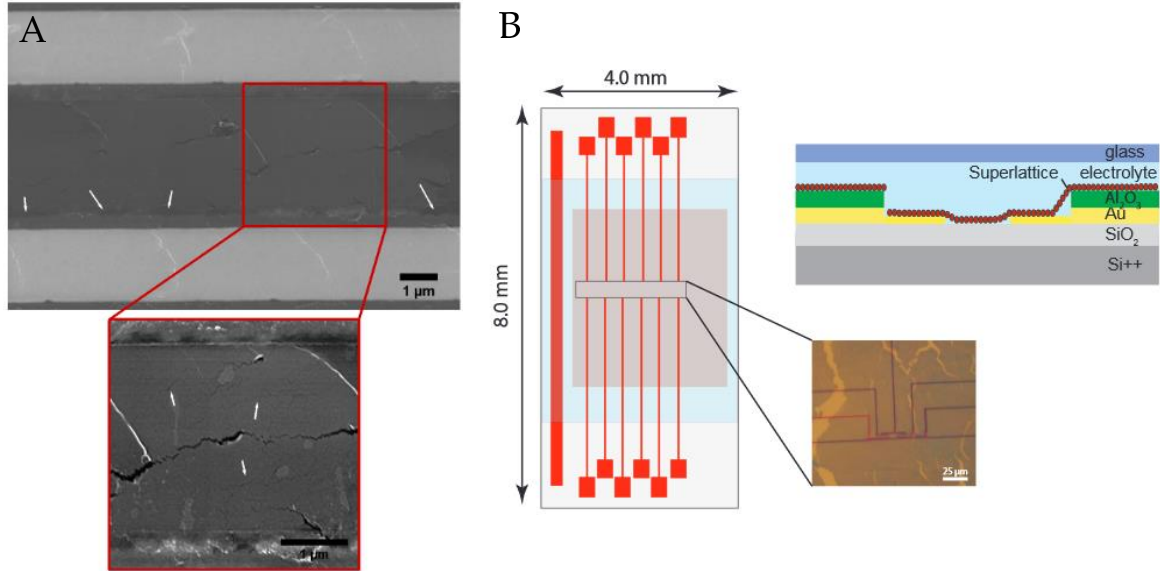
Figure 5.1: (A) SEM image of a single monolayer QD superlattice as FET channel. The white arrows indicate macroscopic defects such as cracks in the QD superlattice and problematic channel-electrode contact due to the 150 nm height difference. Figure taken and adapted from [?]. (B) Electrode designs used for four-probe measurements. Figure taken and adapted from [?].

5.1 Experimental details

The synthesis and the formation of the QD superlattice are based on the methods already described in the chapter 3. The superlattice studied in this chapter consists of PbSe QDs atomically connected covered with their native Pb-oleate ligands on their (111) facets. The mean diameter of the QDs is 5.8 nm. For this experiment, the QD array was transferred onto a heavily p-doped silicon wafer with a resitivity of 0.01-0.05 Ω.cm thanks to the Langmuir-Schaeffer deposition technique. Prior to the deposition of the superlattice, a thin film of 80 nm of SiO_2 was deposited on the wafer. The addition of this oxide layer avoids any current leakage through the substrate while performing four-point measurements. This way the current is forced to flow inside the QD array. An illustration of the experimental setup and the four-point measurement is shown in Figure **??**. The source tip is used to inject charge carrier inside the superlattice. Then the current flows inside the arrays and is collected by the drain tip in contact with the superlattice. The two internal probes are used to measure the potential drop induced by the electrical resistance of the superlattice. As explained in Chapter 2.3.1, the ratio between the potential drop and the current yields a direct access to the conductivity in the superlattice.

Figure 5.2: Schematics of the experimental setup. The superlattice was transferred to a silicon wafer where a 80 nm silica layer was first deposited. The four tips are brought in contact with the QDs and one of the external tip is set as the source in order to inject charge carriers inside the superlattice. Then the current flows in the QD array (green arrows) and is collected by the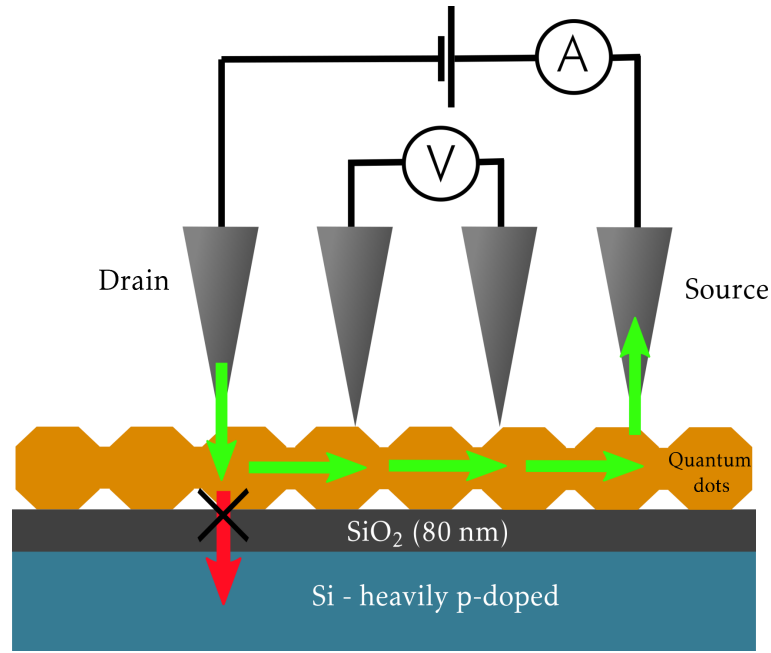 drain tip. Thanks to the oxide, the current cannot leak through the substrate (red arrow) and is forced to run through the QDs in the superlattice. The drop in voltage across the superlattice is measured by the two inner probes.

Following the synthesis, the sample was placed on a sample holder. Two beryllium wires connected to the sample holder were used to top contact the sample. Subsequently, the sample was quickly loaded into Ultra High Vacuum (UHV) system containing a MultiProbe Scanning Tunneling Microscope (MultiProbe-STM, Omicron Nanotechnology). In these experiments, the tips were made by chemically etching a polycrystalline tungsten wire with a NaOH solution, similarly to the previous STM experiments. Images of the four tips are presented in Figure **??**. Measurements have been carried out on the as-synthesized sample at room temperature after loading it in UHV. Remarkably, it was possible to approach the four STM tips in the vicinity of the surface by tunneling approach. In order to perform this tunnel approach despite the oxide layer, the tips were approached with a high bias (5 to 10V) and a small setpoint (*sim* 10 pA) current in a region close to the contact. In this way, the current detected by the tip when approaching the tunnel did not pass through the thick oxide barrier, but passed through the superlattice straight to contact. This was made possible thanks to the high conductive nature of the sample. This approach allows for controlled contact of the tips with the superlattice, any damage of the superlattice and the probes. After contacting the superlattice, the quality of the contact was checked by performing an I(V) curve between the contacted tip and the beryllium contact (used as the ground electrode). A typical I(V) characteristic for a good tip/sample contact is shown in Figure **??**. The linear behavior in the I(V) curve is representative of a

good Ohmic contact. Once each of the four tips was contacted properly, following the above procedure, four-point measurements were performed.
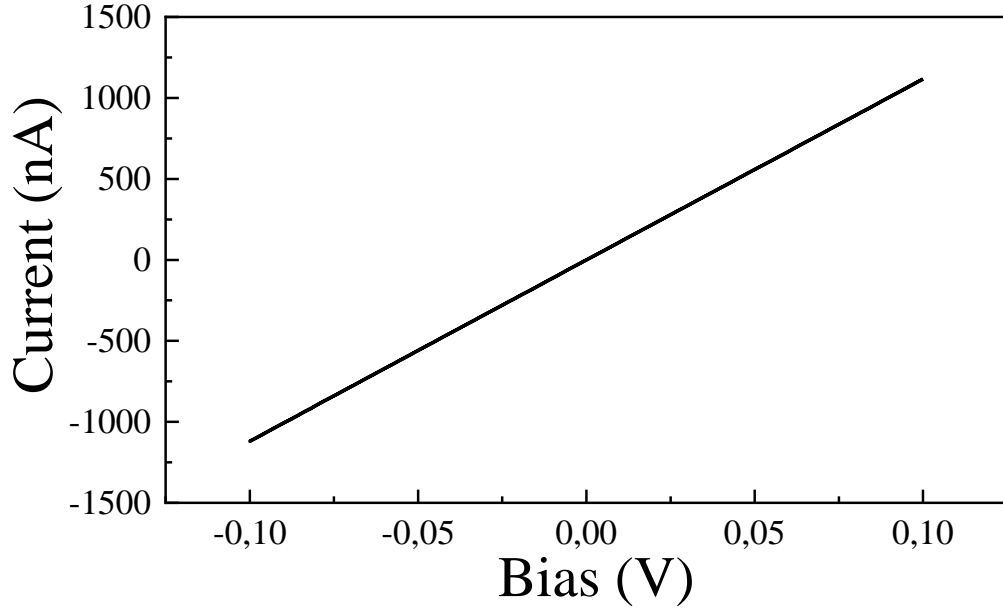
Figure 5.3: Example an I(V) curve characteristic of a good tip/sample contact.

5.2 Surface conductivity of PbSe superlattice

The standard four-point measurement procedure involves four tips placed in line with an equidistant spacing between them. In this work we preferentially use a linear nonequidistant configuration where three tips remain at a fixed mutual distance d while the fourth one is allowed to move. Its separation with its neighbor tip, labelled x, is varied (see Figure **??**). We choose this configuration in order to minimize the number of tips to be moved and repositioned. This configuration is both convenient and efficient since it also prevents modification of the contact resistance of the three remaining tips between the measurements.

In the case of the classic linear equidistant probe spacing, the relationships between the measured four-point resistance and the resistivity of a 3D sample ρ_{3D} or the sheet resistivity of 2D sample ρ_{2D} [**?**] are given by the equations 1.45 and 1.46 of chapter 2 :

$$R_{3D} = \frac{\rho_{3D}}{2\pi d} \quad \text{(3D)} \quad R_{2D} = \frac{\rho_{2D}}{\pi} \ln(2) \quad \text{(2D)} \tag{5.1}$$
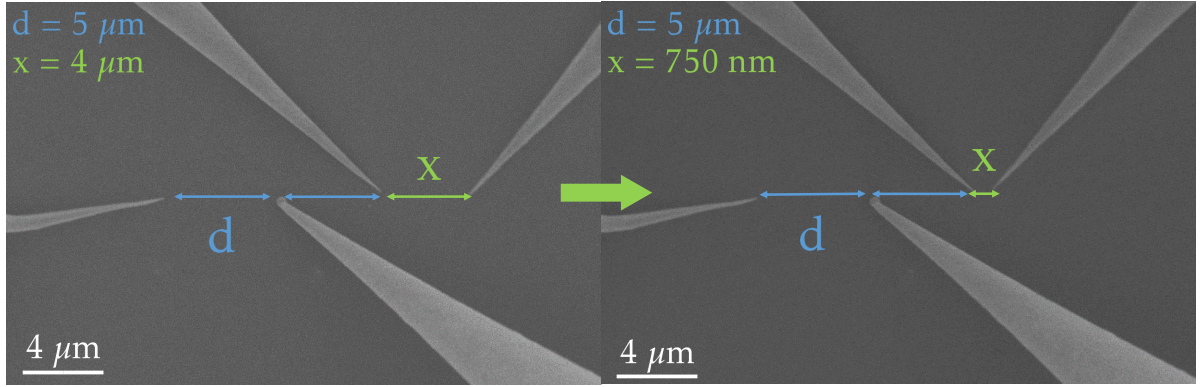
Figure 5.4: Nonequidistant tips configuration of a four-probe measurement. Three tips are placed with equidistant spacing d (here $d = 5$ μm). Only the last tip is moved to change the distance x. In our experiments, x can be varied from 25 μm down to 75 nm. The figure shows two x spacings of 4 μm and 750 nm.

The 3D case exhibits a dependence with the spacing d. On the contrary, the equation for a current flowing in a 2D layer leads to a constant four-point resistance, independent of the probe spacing. For the nonequidistant configuration, the signature of a 2D transport, namely the constant four-point resistance, is lost. Equation **??** needs to be modified as follow (equation 1.5 from chapter 2) [**?**, **?**, **?**] :

$$R_{2D}^{4p}(d,s) = \frac{\rho_{2D}}{2\pi}\left[\ln\left(\frac{2d}{x}\right) - \ln\left(\frac{d}{x+d}\right)\right] \tag{5.2}$$

The four-point resistances measured on the PbSe QD superlattice are shown in Figure **??**. These resistances are directly extracted from the four-point V(I) curves shown in the inset of Figure **??**. Four-point measurements have been performed with a nonequidistant configuration for $x \leq d = 15$ μm, and with the equidistant configuration for distance $x = d \geq 15$ μm. For the linear equidistant configuration (right half of Figure **??**) the resistance shows no dependence with the probe spacing and exhibits a constant behavior. This clearly indicates a pure 2D transport. From Equation **??**, the constant resistance measured with the equidistant configuration yields a sheet conductivity σ_{2D} of 4.16 $\times 10^{-5}$ $\Omega^{-1}/\square$. For the nonequidistant probe configuration, the best fit of our experimental data is obtained with Equation **??** (see red curves on left part of Figure **??**). It yields a sheet conductivity σ_{2D} of 4.54 $\times 10^{-5}$ $\Omega^{-1}/\square$. The values found with these two different techniques are in good agreement, confirming the two dimensional behavior of the transport in the PbSe superlattice.

Note that the four-point resistance measured by the equidistant probe spacing is only 5 kΩ. For comparison, previous four-probe measurements performed on similar PbSe superlattice with identical probe spacings gave resistances in the range between 15 and 287 kΩ [**?**]
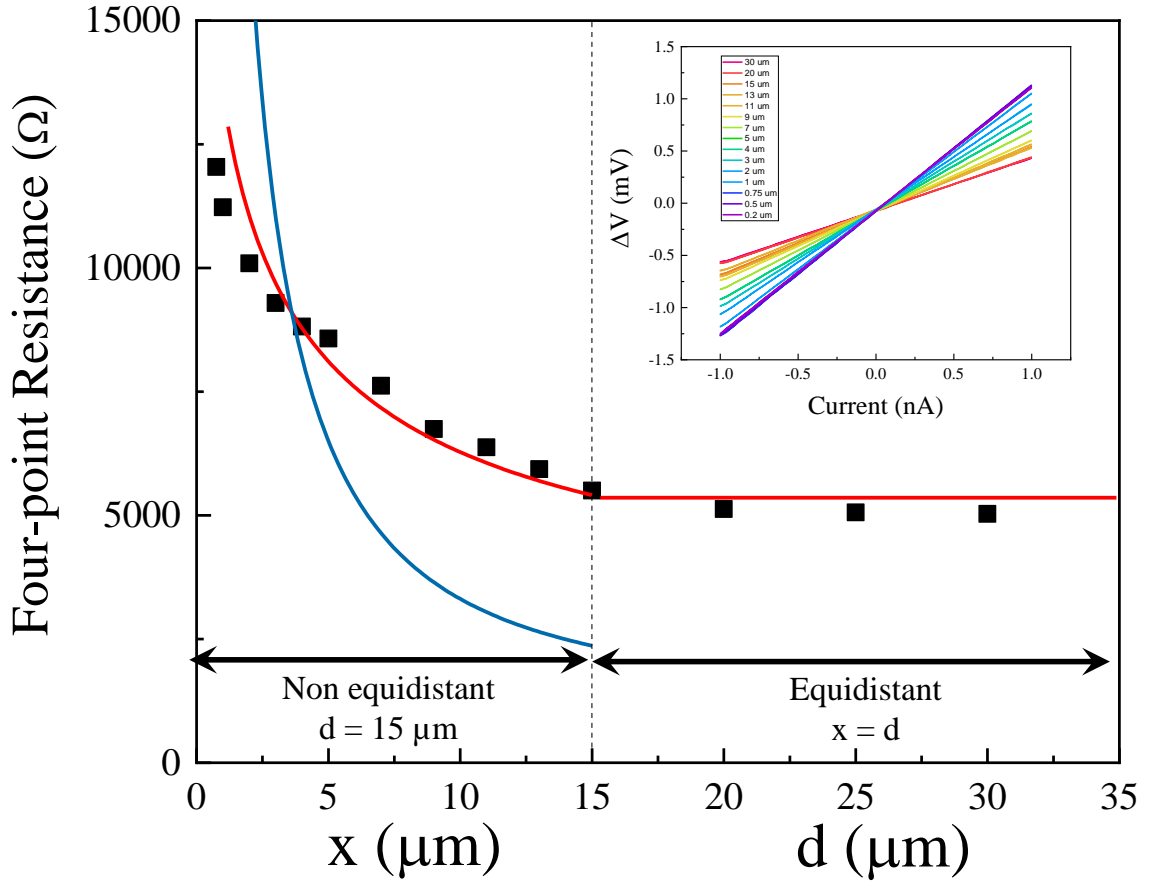
Figure 5.5: Four-point resistances measured on the PbSe superlattice as function of the probe distance d and x. The four-point resistances were measured for two configurations, the equidistant (right half) and the nonequidistant (left half). The red solid line on the left half shows the best fit obtained from Equation **??** for the 2D case while the red line on the right part shows the fit obtained from Equation **??**. The blue curve shows the best fit obtained from Equation **??** for the 3D case. In both cases these equations represent the expected behavior for a pure 2D conductance. The corresponding conductivities σ_{2D} yield consistent values of 4.16×10^{-5} $\Omega^{-1}/\square$ and 4.54×10^{-5} $\Omega^{-1}/\square$ for the left and right parts, respectively. In the inset the raw four-point measurement data are shown.

Additional four-point measurements have been performed solely with the nonequidistant configuration for different equidistant probe spacings d of 5 and 25 μm. The corresponding four-point measurements are shown in Figure **??**. The data fitted nicely with Equation **??**, revealing again a 2D transport. We find slightly lower sheet conductivities values $\sigma_{2D} = 3.125 \times 10^{-5}$ $\Omega^{-1}/\square$ and $\sigma_{2D} = 3.225 \times 10^{-5}$ $\Omega^{-1}/\square$ for the probe spacing d of 5 and 25 μm, respectively. These measurements were performed in other regions of the sample with similar tip orientation. We will show in the next section that this small changes in the sheet conductivity can be attributed to an anisotropic conductance induced by the existence of cracks in the superlattice.
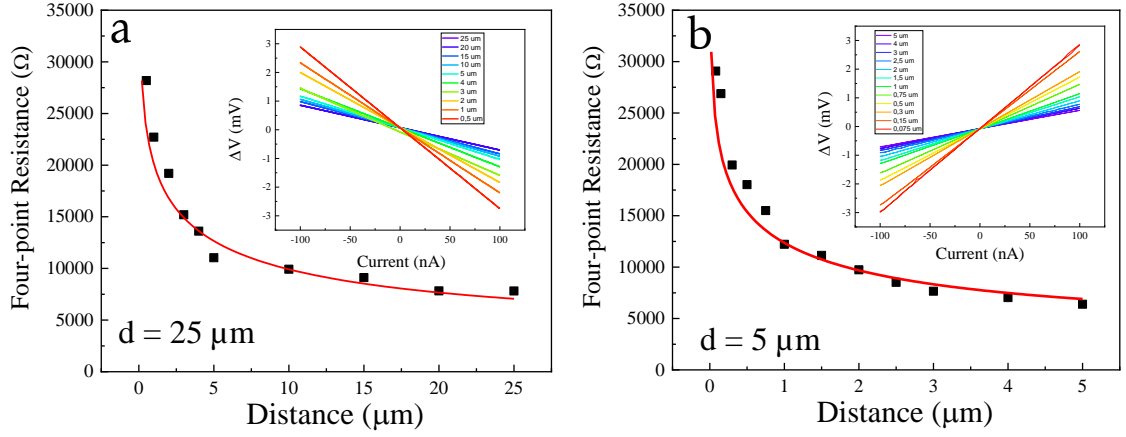
Figure 5.6: Four-point resistances of an epitaxilly connected QD superlattice as function of the probe distance x for nonequidistant spacing. The four-point resistance has been measured for two different probe spacings $d = 25\mu m$ (a) and $d = 5\mu m$ (b). The red solid line represents the best fit of the data obtained by Equation **??**. It represents the expected behavior for a pure 2D conductance. The corresponding sheet conductivities σ_{2D} are of 3.125×10^{-5} $\Omega^{-1}/\square$ and $3.225 \times 10^{-5}\ \Omega^{-1}/\square$ for d = 25μm and d = 5 μm, respectively. Insets : raw V(I) four-point measurement data.

5.3 Conductance anisotropy and influence of the cracks in the transport across the PbSe superlattice
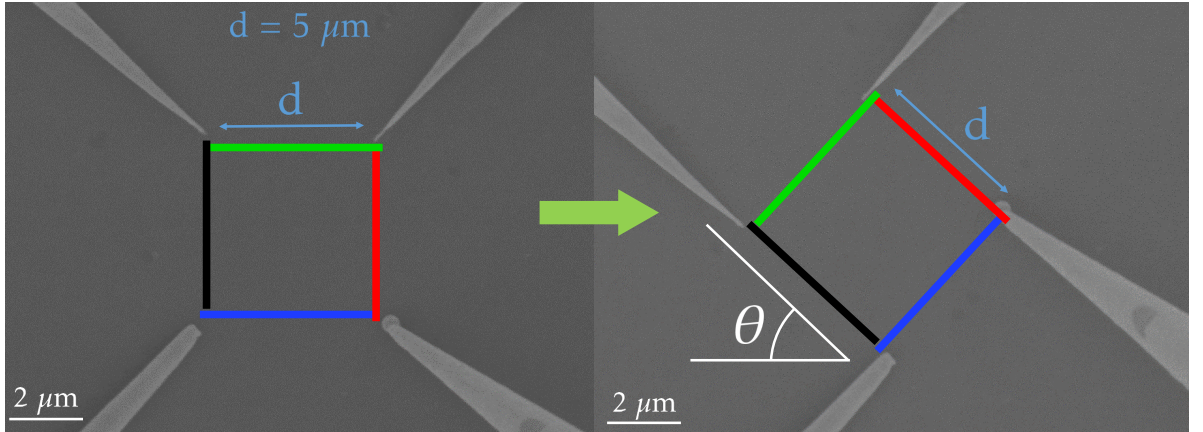
Figure 5.7: Square tips configuration of a four-probe measurement. The four tips are placed with equidistant spacing d (here $d = 5\ \mu m$). For one fixed orientation of the probes four different rotation angles can be realized by successively assigning different probes as current and voltage probes. This is illustrated by the different colored lines (red, green, blue and black) on the figure. Subsequently, the tip square is rotated by an angle θ.

The distance-dependent linear configuration was a powerful technique to access the sheet conductivity of the sample and disentangle the 3D transport from the 2D transport. Unfortunately, this method is not suitable to measure the conductance anisotropy of a sample. On the other

hand, the Van der Pauw configuration of the tips, shown in Figure **??**, can measure the four-point resistance along different orientations. In this particular configuration, the tips are in contact with the sample in a square configuration. Similar to the linear configuration, two tips positioned at one side of the square are configured to inject and collect the current. The two remaining tips, on the other side, are used as potential probing tips. Thanks to this tip arrangement, it is possible to determine if a sample exhibits an anisotropic transport behavior. The electrical conductivity in the case of an anisotropic material is no longer a scalar but becomes a conductivity tensor with different components $\sigma_{i,j}$ representing the conductivities along the different directions of the solid. These anisotropic conductivities can be accessed by rotating the square tip arrangement by an angle θ and performing four-point measurements for each angle (see Figure **??**).
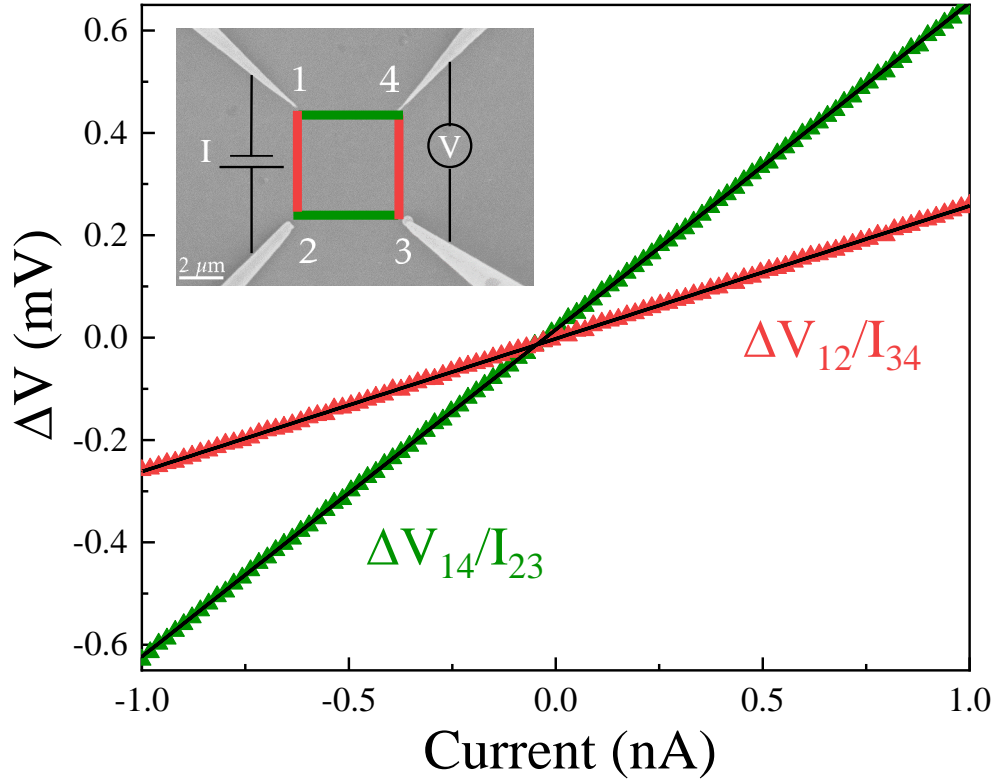
Figure 5.8: V(I) curves obtained with a square configuration with a probe spacing of $d = 5$ μm. The inset shows the STM tips in a Van der Pauw configuration with the tips 1 and 2 set as the injection and collection probes while the tips 3 and 4 are the voltage probes. The red curve corresponds to the measure performed with this tip configuration $\Delta V_{12}/I_{34}$. The green curve corresponds to the $\Delta V_{14}/I_{23}$ configuration.

Figure **??** shows V(I) curves measured with the square configuration for a probe spacing d of 5 μm. ΔV_{ij} corresponds to the voltage drop between tip i and probe j while the current $I_{k,l}$ is injected and collected by tips k and l, as shown in the inset of Figure **??**. The resistances were extracted thanks to a linear fit of the data (black solid lines on Figure **??**). From these measurements, we show that a change of the combination of source-drain and voltage probes

has a significant impact on the measured resistances : $\Delta V_{14}/I_{23} = 6400\ \Omega$ (green) and $\Delta V_{12}/I_{34}$ = 2500 Ω (red). The resistances measured along two orthogonal directions exhibit two distinct trends revealing the presence of an anisotropy in the conductance of the superlattice.
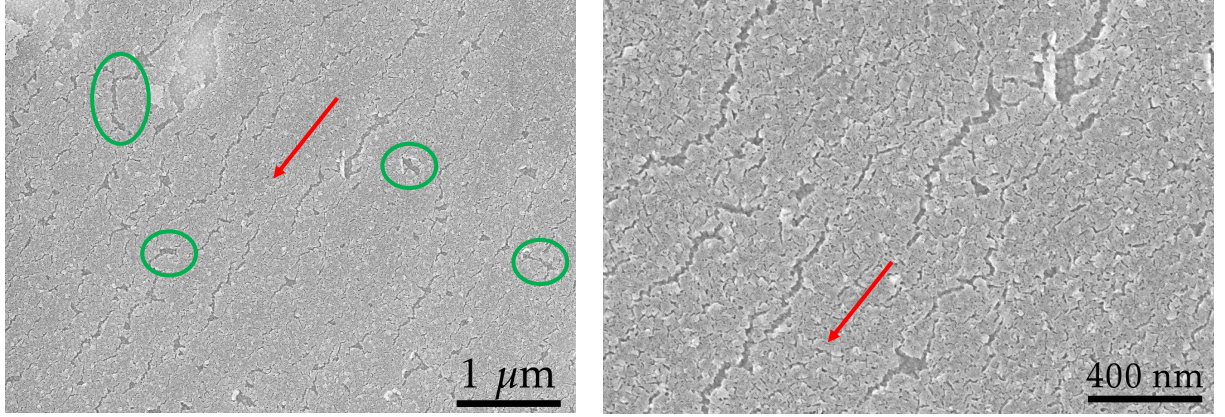
Figure 5.9: SEM images of the superlattice. Acceleration voltage : 5 kV. The red arrows indicate the major direction for the propagation of the cracks. The green circle highlight crack that are not aligned with the major crack orientation.

High resolution SEM images taken at the same position on the sample reveal the presence of cracks in the superlattice. The major cracks, visible in Figure **??**, show dimensions of 20 to 50 nm in width and of hundred of nanometers to few microns in length. The cracks are somewhat well ordered as they seem to be parallel between them and are pointed toward one direction (see the red arrow in Figure **??**). This observation explains the anisotropy measured with the transport experiment as the cracks prevent the current to flow homogeneously in the superlattice along the direction of the cracks. The presence of cracks in this type of material is known to limit the transport in PbSe superlattices [**?**, **?**].

In principle, the resistances obtained from the measurements in Figure **??** could allow us to derive $\sigma_{\parallel}$ and $\sigma_{\perp}$ separately. But in order to further quantify the crack-induced conductance anisotropy and improve the measurement precision, the square formed by the tips was rotated successively by an angle θ relative to the cracks propagation direction. This way, the four-point resistance is measured in every directions in the plane of the superlattice. The measured four-point resistances as a function of the rotation angle θ are shown in Figure **??** for a probe spacing d of 5 μm. For one fixed orientation of the four tips in the square configuration, four different rotation angles can be realized by successively assigning different tips as current and voltage probes. These four different combinations correspond to the different colored data points in Figure **??**. The angle dependence of the square configuration on the four-point resistance can be obtained from the solution of the Poisson equation for an anisotropic 2D sheet (equation

1.53 from chapter 2) [**?, ?**] :

$$R_\theta = C \ln \left(\frac{(\frac{\sigma^\parallel}{\sigma^\perp} + 1)^2 - 4\cos^2\theta \sin^2\theta (\frac{\sigma^\parallel}{\sigma^\perp} - 1)^2}{(\sin^2\theta + \frac{\sigma^\parallel}{\sigma^\perp}\cos^2\theta)^2} \right) \tag{5.3}$$

where $C = 1/(4\pi\sqrt{\sigma^\parallel\sigma^\perp})$. By fitting this equation to the results of an angle-dependent measurement one can determines the components $\sigma_\perp$ and $\sigma_\parallel$ of a sample with anisotropic conductivity.

Figure 5.10: Angle dependence of the measured four-point measured resistance with a square configuration and a tip spacing $d = 5$ μm. The experimental data are fitted by Equation **??** (see red curve). The colored data points correspond to the four directions accessible by changing the source-drain combination of the probes.

The results reported in Figure **??** show the dependence of the conductance as function of the angle θ. Equation **??** was used to fit the experimental data (see red curves in Figure **??**). The fit from the data yields parallel conductivity of $\sigma^\parallel = 4.54 \times 10^{-5} \Omega^{-1}/\square$ and perpendicular conductivity of $\sigma^\perp = 2.07 \times 10^{-5} \Omega^{-1}/\square$. The anisotropy measured in this case $\sigma^\parallel/\sigma^\perp$ is found to be 2.4, meaning that the cracks only induce a moderate modification of the conductivity of the sample. While the experimental behavior seems to be in good agreement with the theory, the measured resistance does not reach the expected minimum around 0° and 180°. A slight bump at the expected minimum resistance is observed instead. This can be explained by the

distribution of the cracks. While the majority of the cracks are pointed toward the same direction and have the similar length, some smaller cracks, placed in between the main ones, follow different orientations (see green circle in Figure **??**). When the square angle is aligned with the main cracks the contribution to the resistance from the main cracks is minimum. In this case, the contribution from the smaller cracks becomes dominant, explaining this slight increase in the resistance. This means that performing an angle-dependent four-point measurement with a smaller probe spacing d should eliminate this artifact.
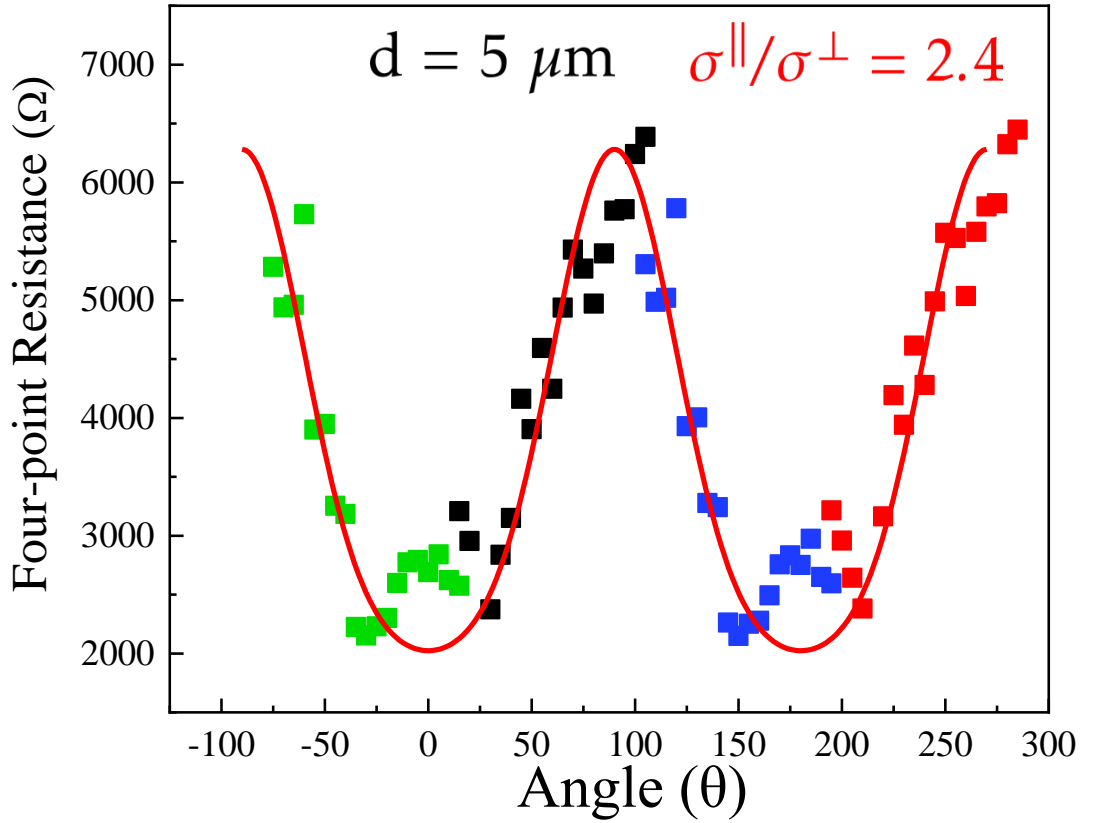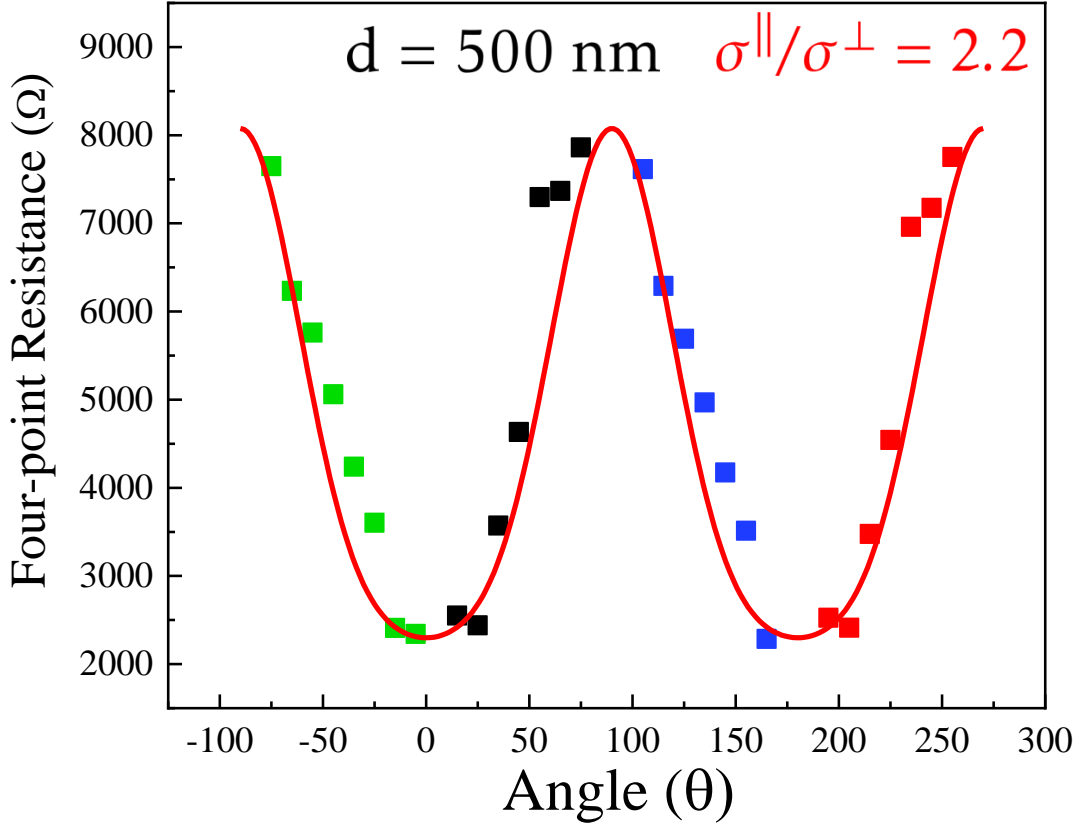

Figure 5.11: Angle dependence of the measured four-point measured resistance with a square configuration and a tip spacing d = 500 μm. The experimental data are fitted by Equation **??** (see red curve). The colored data point corresponds to the four directions accessible by changing the source-drain combination of the probes.

Therefore, we performed angle-dependence four-point measurement for a square with probe spacing of d = 500 nm. In this case, the fit of the experimental data by the Equation **??** gives a value for the parallel $\sigma^\perp$ and perpendicular $\sigma^\parallel$ conductivities of 1.62 $\times 10^{-5}\Omega^{-1}/\square$ and 3.5 $\times 10^{-5}\Omega^{-1}/\square$, respectively. The measured anisotropy $\sqrt{\sigma^\parallel \sigma^\perp}$ is 2.2 which is very similar to the value given by the previous angle-dependent measurement over 5 μm. No bump around the minimum value of the resistance is visible here unlike the previous measurement. This confirms the assumption previously made about the influence of the smaller, misaligned cracks.

From the angle-dependent square configuration, we can extract the geometric mean con-

ductivity $\sqrt{\sigma^{\parallel}\sigma^{\perp}}$. We found a value of $\sqrt{\sigma^{\parallel}\sigma^{\perp}}$ = 3.06 $\times 10^{-5}\Omega^{-1}/\square$ for d = 5 μm and $\sqrt{\sigma^{\parallel}\sigma^{\perp}}$ = 2.41 $\times 10^{-5}\Omega^{-1}/\square$ for d = 500 nm. These conductivities are found to have nearly the same value as the previously measured sheet conductivities with the linear nonequidistant configuration. Therefore, by using two independent methods, namely, the angle dependent square configuration and the nonequidistant linear distance dependent configuration, similar results were obtained for the surface conductivity. A summary of all the sheet conductivity values on the PbSe superlattice measured by MultiProbe STM is presented in Table 1.1.

In Line configuration (Probes spacing)	Conductivity σ_{2D} ($\Omega^{-1}/\square$)	Square configuration (Probes spacing)	Conductivity $\sigma_{\perp}$ ($\Omega^{-1}/\square$)	Conductivity $\sigma_{\parallel}$ ($\Omega^{-1}/\square$)	Geometric mean value $\sqrt{\sigma^{\parallel}\sigma^{\perp}}$($\Omega^{-1}/\square$)
25 μm	3.125 $\times 10^{-5}$	5 μm	2.07 $\times 10^{-5}$	4.54 $\times 10^{-5}$	3.06 $\times 10^{-5}$
15 μm	4.16 $\times 10^{-5}$	500 nm	1.62 $\times 10^{-5}$	3.5 $\times 10^{-5}$	2.41 $\times 10^{-5}$
5 μm	3.225 $\times 10^{-5}$				

Table 5.1: Sheet conductivities measured with the different probes configuration

In order to fully quantify the cracks influence, the sheet resistivity of the crack-free surface ρ_{surf} must be disentangled from the resistivity induced by a single crack ρ_{crack}. The conductivity measured in the direction parallel to the cracks by the angle-dependence square configuration corresponds directly to the crack-free conductivity :

$$\frac{1}{\sigma^{\parallel}} = \rho^{\parallel} = \rho_{surf} \tag{5.4}$$
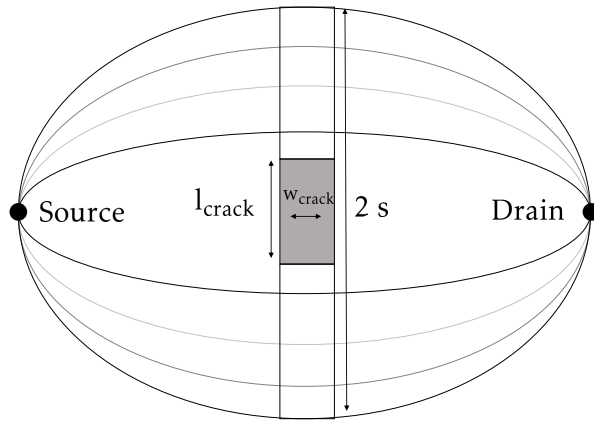
Figure 5.12: Illustration of the current distribution induced by the two current probes around a single crack.

In a second step the resistivity induced by a single crack is estimated. A crack corresponds to a void in the superlattice, an elongated region empty of any QDs. Usually, these crack have an elongated shape with width w_{crack} and a length l_{crack}. In order to estimate the resistance induced by a single crack we considered a model were the cracks simply blocks the field lines. By solving a simple Poisson equation it has been shown that that almost 90% of the surface

current was spread over twice the length of the current probe spacing $3d$ in a direction perpendicular to the probe alignment for a line configuration [?]. This current enter in the void related to the crack. It passes through a limited region extending over $2\times3d - l_{crack}$. Therefore, if the length of the crack, l_{crack}, is of the order of $3d$, it adds a significant resistance to the measured resistance. Indeed, the resistance is the product of ρ_{surf} with w_{crack} divided by l_{crack}. As a result, the resistance of the stripe of width d and length $6d - l$ is :

$$R_{crack} = \frac{\rho_{surf} \times w_{crack}}{6d - l_{crack}} \tag{5.5}$$

When compared with the resistance of the same stripe without the crack, then :

$$R = \frac{R_{surf}}{1 - \dfrac{l}{6d}} \tag{5.6}$$

For the tip separation is larger than the length of the crack, the crack increases the resistance only slightly. However, for a tip separation of 500 nm and a crack with a length of 500 nm, as shown in Figure 5.5, then the resistance of stripe the can be multiplied by a factor of 2, accounting for the ratio found for the conductivity between both directions.

5.4 Influence of bigger cracks on transport
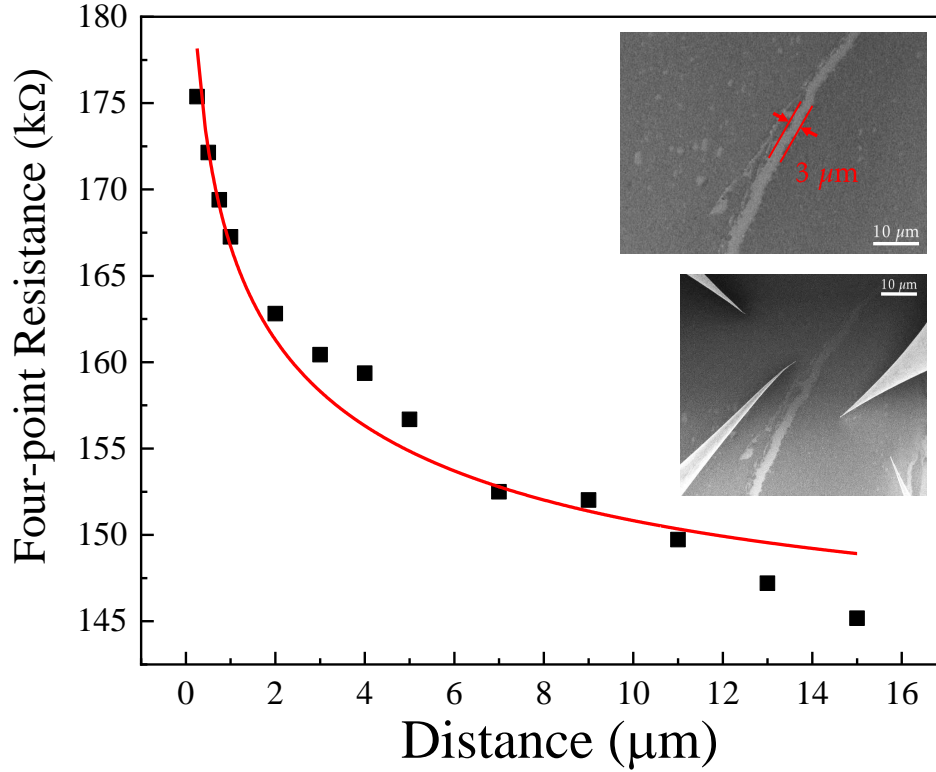
Figure 5.13: Four-point resistances of an epitaxilly connected QDs superlattice as function of the probe distance *x* for nonequidistant spacing. The four-point resistance was measured for a probe spacing d = 15 μm. The red solid line represents the fit of the data by Equation 1.2 plus an offset corresponding to the crack induced resistance. Inset : SEM image of the crack and a SEM image of the STM tip positioned around the crack.

While cracks investigated in the previous section had a width of approximately 30 to 50 nanometers, larger ones can be encountered in the superlattice. For example, a crack with a width 3 μm is shown in the inset of Figure **??**. The linear configuration was used to performed four-point measurements with the two voltage probing tips placed on both sides of the crack. In this way the increase of the resistance induced by the large crack could be measured (see lower inset of Figure **??**). The measured resistance for the equidistant linear configuration with a distance *d* of 15 μm, is found to yield 145 000 Ω. This a 30 fold compared to the resistance value (R = 5000Ω) found above for similar measurements with the same probes spacing (see Figure **??**). We considered that the contribution of the crack to the total measured resistance could be expressed as a resistance in series. In order to fit Equation **??** to the experimental data, an offset of 137500 Ω, corresponding to the resistance induced by the crack, was added. Therefore, bigger cracks induce huge limitation for the transport of charge carriers in the superlattices.

5.5 Estimation of the mobility

A key parameter for potential applications is the mobility. This intrinsic quantity of the material can be deduced from the expression of the resistivity :

$$\rho = \frac{1}{\mu n e} \Rightarrow \mu = \frac{1}{\rho n e} \tag{5.7}$$

From the above experiments the crack-free resistivity was measured. The charge carrier concentration p can be deduced from :

$$p = N_V e^{\dfrac{-(E_V - E_F)}{k_B T}} \tag{5.8}$$

Where N_V is the effective density of states, k_B the Boltzmann constant, T the temperature, and $E_V - E_F$ the energy difference between the Fermi level and the valence band of the material. From the STS spectra measured on similar superlattice in Chapter 3, the valence level of the QDs was found to be very close from the Fermi level (see Figure ??). The difference between the onset of the bias at negative bias corresponding to the top of the valence band and the zero gives values between 50 and 80 mV. Subsequently, the lever arm calculated in Chapter 3 was used in order to convert the bias difference in energy. Thus, $E_V - E_F$ was found to range between 30 and 50 meV.
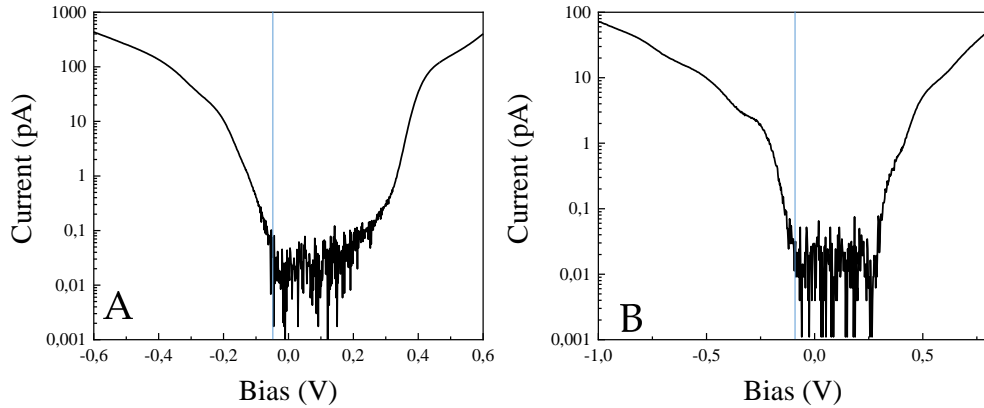
Figure 5.14: A and B : Example of I(V) measured with STS on the PbSe superlattice studied in chapter 3. The vertical line indicates the position of the top of the valence band.

Since the superlattice can be considered as a thin film the two dimensional effective density of states was calculated from the following expression :

$$N_V = \frac{m_h^* k_B T}{\pi \hbar^2} \tag{5.9}$$

Where m_h^* is the hole effective mass in PbSe. In the case of PbSe, the effective masses of holes and electrons are similar $m_h^* \approx m_e^*$ [?]. Therefore, the hole effective mass in PbSe is 0.16

[**?**]. From the two above equations the charge carrier concentration was estimated to range between $2.55 \times 10^{-11} \mathrm{cm}^{-2}$ and $5.52 \times 10^{-11} \mathrm{cm}^{-2}$. By considering this hole concentration and the crack-free resistivity of the superlattice (ρ_{2D}= 22 kΩ.$\square$) the superlattice mobility was estimated to yields between 508 cm^2/(V.s) and 1101 cm^2/(V.s). These high mobility are found to be of the same order of magnitude as the ones measured in bulk PbSe at room temperature [**?**].

In a second approximation, the charge carrier concentration was calculated from the surface density of QDs. In the literature, the QD surface density was estimated from TEM images. For QDs with a diameter close to 5.8 nm this surface density was found to yields around 2.3 -2.9 $\times 10^{12} \mathrm{cm}^2$ [**?, ?, ?**]. In good agreement with previous transport measurement [**?**] our STS experiments showed that QDs superlattice were p-doped. In the past, the charge concentration per QD of n-doped superlattice had been estimated to be 1 electron/QD [**?**]. Assuming a charge concentration per QD of 1 hole per QD. The previously measured conductivity $\sigma^{textsurf}$ yields the mobility around 120 cm^2/(V.s). While this new estimation is lower than the previous ones, it is still one order of magnitude than the higher mobility reported in the literature thanks to an ion-gel FET [**?**] .

Conclusion

The transport properties of a PbSe QDs solid were the QDs are attached through epitaxial connections were investigated in this chapter. We use a distance-dependent linear configuration for both the equidistant and nonequidistant probes spacings to unveil the 2D nature of the transport. The sheet conductivity was measured and found consistent for two different probe spacing in the 1×10^{-5} - 5×10^{-5} Ω^{-1}/$\square$ range. In a second time, an angle-dependent square configuration was used to show the influence of cracks present in the superlattice on the transport properties. The anisotropy induced by the cracks yields a ratio $\sigma^{\parallel}/\sigma^{\perp} \simeq 2.4$, which can be explained by the choice of the probe spacing with respect to the length of the major cracks in the superlattice. While the cracks obviously reduce the electrical transport in the superlattice, their existence is common to all the studies published in the literature so far. Therefore, the low resistivity that we measure should arise from a better coupling of the QDs. Despite the lack of an estimation of the carrier mobility has been performed based on the position of the Fermi level found in the tunneling spectra of the previous chapter. A mobility in the range of hundreds of cm^2/(V.s) has been estimated, highlighting the benefit of fusing the facets to improve the transport of charge carriers in the superlattice.

Conclusion

Advances in terms of chemical synthesis now allow to prepare 2D structures using colloidal quantum dots as building blocks. These materials have many advantages in term of cost and flexibility, making them very attractive from a scientific and technological point of view. The aim of this thesis was to study the electronic structure and transport properties of novel colloidal QD superlattice with epitaxial connections. For this purpose, scanning tunnelling microscopy and spectroscopy was used to access local information about the individual behaviour of QDs in the superlattice.

Thanks to its ability to acquire high-resolution image, scanning tunnelling microscopy was used to image a PbSe QD superlattice deposited on a gold substrate. Then spectroscopy was performed on an individual QD in the array to measure the quantum energy levels of individual QDs. We performed STS on the as-synthesized sample revealing a lack of homogeneity in the measured spectra. We showed that annealing the superlattice to 120°C led to a stable and reproducible spectroscopy of the QDs across the superlattice. The STS performed on more than 25 individual QDs showed a systematic p-doping, likely due to the Pb-oleate ligand removal at the surface of the QDs. Moreover, the analysis of the width of the peaks shows a more or less pronounced coupling of the valence band states.

As a minority of QDs shows a peak in the band gap, a deeper understanding of this peak led is us to study. The topographic and electronic properties of PbSe QDs superlattice deposited on a silicon substrate. The state observed in the STS spectra revealed to be a strongly localized state in the band gap of the PbSe QD. From the absence of ligands in our system we conclude that this trap state originate from the (111), non stochiometric facets of the QDs which are non passivated. We found that the trap states can be used as a sensor of the electrostatic fluctuations at the SiO_2 surface.

The transport properties of the PbSe QDs superlattice with a square geometry where the (111) facets were passivated, were investigated by multi-probe STM. We first unveiled the two dimensional nature of the transport by using distance-dependent linear probes configuration. Subsequently, we measured the electrical sheet resistivity of the sample. Thanks to an angle-dependent square configuration, the influence of cracks present in the QD array was quantified. Surprisingly, the conductance anisotropy induced by this cracks only moderately influ-

ence the current propagation into the superlattice. We estimated the mobility of the charge carriers in this sample and found record values that need to be confirmed with gate transport measurements. Such a result demonstrates the potential of assemblies of fused QDs to ensure good performances in electronic QD-based devices.

Bibliography

[1] N. A. Franchina Vergel, A. Tadjine, V. Notot, M. Mohr, A. Kouassi N'Guissan, C. Coinon, M. Berthe, L. Biadala, K. K. Sossoe, M. M. Dzagli, J.-C. Girard, G. Rodary, L. Desplanque, R. Berndt, D. Stiévenard, X. Wallart, C. Delerue, and B. Grandidier. Influence of doping level and surface states in tunneling spectroscopy of an I n 0.53 G a 0.47 As quantum well grown on p -type doped InP(001). *Physical Review Materials*, 3(9):094604, September 2019.

[2] Peter Liljeroth, Pedro A. Zeijlmans van Emmichoven, Stephen G. Hickey, Horst Weller, Bruno Grandidier, Guy Allan, and Daniël Vanmaekelbergh. Density of States Measured by Scanning-Tunneling Spectroscopy Sheds New Light on the Optical Transitions in PbSe Nanocrystals. *Physical Review Letters*, 95(8):086801, August 2005.

[3] Joshua J. Choi, Yee-Fun Lim, Mitk'El B. Santiago-Berrios, Matthew Oh, Byung-Ryool Hyun, Liangfeng Sun, Adam C. Bartnik, Augusta Goedhart, George G. Malliaras, Héctor D. Abruña, Frank W. Wise, and Tobias Hanrath. PbSe Nanocrystal Excitonic Solar Cells. *Nano Letters*, 9(11):3749–3755, November 2009.

[4] Zhenyu Yang, James Z. Fan, Andrew H. Proppe, F. Pelayo García de Arquer, David Rossouw, Oleksandr Voznyy, Xinzheng Lan, Min Liu, Grant Walters, Rafael Quintero-Bermudez, Bin Sun, Sjoerd Hoogland, Gianluigi A. Botton, Shana O. Kelley, and Edward H. Sargent. Mixed-quantum-dot solar cells. *Nature Communications*, 8(1):1325, December 2017.

[5] AmirAbbas YousefiAmin, Niall A. Killilea, Mykhailo Sytnyk, Philipp Maisch, Ka Cheong Tam, Hans-Joachim Egelhaaf, Stefan Langner, Tobias Stubhan, Christoph J. Brabec, Tobias Rejek, Marcus Halik, Katharina Poulsen, Jan Niehaus, Anton Köck, and Wolfgang Heiss. Fully Printed Infrared Photodetectors from PbS Nanocrystals with Perovskite Ligands. *ACS Nano*, page acsnano.8b09223, February 2019.

[6] Zhenwei Ren, Jiankun Sun, Hui Li, Peng Mao, Yuanzhi Wei, Xinhua Zhong, Jinsong Hu, Shiyong Yang, and Jizheng Wang. Bilayer PbS Quantum Dots for High-Performance Photodetectors. *Advanced Materials*, 29(33):1702055, September 2017.

[7] Rinku Saran and Richard J. Curry. Lead sulphide nanocrystal photodetector technologies. *Nature Photonics*, 10(2):81–92, February 2016.

[8] Nanocrystals in their prime. *Nature Nanotechnology*, 9(5):325–325, May 2014.

[9] V B Verma and J J Coleman. High density patterned quantum dot arrays fabricated by electron beam lithography and wet chemical etching. *Appl. Phys. Lett.*, page 4, 2008.

[10] Paola Atkinson, Oliver G. Schmidt, Stephen P. Bremner, and David A. Ritchie. Formation and ordering of epitaxial quantum dots. *Comptes Rendus Physique*, 9(8):788–803, October 2008.

[11] Katsuyuki Watanabe, Nobuyuki Koguchi, and Yoshihiko Gotoh. Fabrication of GaAs Quantum Dots by Modified Droplet Epitaxy. *Japanese Journal of Applied Physics*, 39(Part 2, No. 2A):L79–L81, February 2000.

[12] P. W. Fry, I. E. Itskevich, D. J. Mowbray, M. S. Skolnick, J. J. Finley, J. A. Barker, E. P. O'Reilly, L. R. Wilson, I. A. Larkin, P. A. Maksym, M. Hopkinson, M. Al-Khafaji, J. P. R. David, A. G. Cullis, G. Hill, and J. C. Clark. Inverted Electron-Hole Alignment in InAs-GaAs Self-Assembled Quantum Dots. *Physical Review Letters*, 84(4):733–736, January 2000.

[13] Wiel H. Evers, Bart Goris, Sara Bals, Marianna Casavola, Joost de Graaf, René van Roij, Marjolein Dijkstra, and Daniël Vanmaekelbergh. Low-Dimensional Semiconductor Superlattices Formed by Geometric Control over Nanocrystal Attachment. *Nano Letters*, 13(6):2317–2323, June 2013.

[14] Sang-Min Lee, Young-wook Jun, Sung-Nam Cho, and Jinwoo Cheon. Single-Crystalline Star-Shaped Nanocrystals and Their Evolution: Programming the Geometry of Nano-Building Blocks. *Journal of the American Chemical Society*, 124(38):11244–11245, September 2002.

[15] S. Ithurria, M. D. Tessier, B. Mahler, R. P. S. M. Lobo, B. Dubertret, and Al. L. Efros. Colloidal nanoplatelets with two-dimensional electronic structure. *Nature Materials*, 10(12):936–941, December 2011.

[16] James E. Murphy, Matthew C. Beard, Andrew G. Norman, S. Phillip Ahrenkiel, Justin C. Johnson, Pingrong Yu, Olga I. Mićić, Randy J. Ellingson, and Arthur J. Nozik. PbTe Colloidal Nanocrystals: Synthesis, Characterization, and Multiple Exciton Generation. *Journal of the American Chemical Society*, 128(10):3241–3247, March 2006.

[17] Young-wook Jun, Sang-Min Lee, Nam-Jung Kang, and Jinwoo Cheon. Controlled Synthesis of Multi-armed CdS Nanorod Architectures Using Monosurfactant System. *Journal of the American Chemical Society*, 123(21):5150–5151, May 2001.

[18] Yadong Yin and A. Paul Alivisatos. Colloidal nanocrystal synthesis and the organic–inorganic interface. *Nature*, 437(7059):664–670, September 2005.

[19] D. Sumanth Kumar, B. Jai Kumar, and H.M. Mahesh. Quantum Nanostructures (QDs): An Overview. In *Synthesis of Inorganic Nanomaterials*, pages 59–88. Elsevier, 2018.

[20] D. J. Norris, A. Sacra, C. B. Murray, and M. G. Bawendi. Measurement of the size dependent hole spectrum in CdSe quantum dots. *Physical Review Letters*, 72(16):2612–2615, April 1994.

[21] Huibing Mao, Jing Chen, Jiqing Wang, Zhifeng Li, Ning Dai, and Ziqiang Zhu. Photoluminescence investigation of CdSe quantum dots and the surface state effect. *Physica E: Low-dimensional Systems and Nanostructures*, 27(1-2):124–128, March 2005.

[22] A. Lipovskii, E. Kolobkova, V. Petrikov, I. Kang, A. Olkhovets, T. Krauss, M. Thomas, J. Silcox, F. Wise, Q. Shen, and S. Kycia. Synthesis and characterization of PbSe quantum dots in phosphate glass. *Applied Physics Letters*, 71(23):3406–3408, December 1997.

[23] Freddy T. Rabouw and Celso de Mello Donega. Excited-State Dynamics in Colloidal Semiconductor Nanocrystals. *Topics in Current Chemistry*, 374(5):58, October 2016.

[24] Celso de Mello Donegá. Synthesis and properties of colloidal heteronanocrystals. *Chem. Soc. Rev.*, 40(3):1512–1546, 2011.

[25] Lead selenide (pbse) crystal structure, lattice parameters, thermal expansion: Datasheet from landolt-börnstein - group iii condensed matter · volume 41c: "non-tetrahedrally bonded elements and binary compounds i" in springermaterials (https://doi.org/10.1007/10681727_903). Copyright 1998 Springer-Verlag Berlin Heidelberg.

[26] Athmane TADJINE. *Structure électronique et propriétés de réseaux cohérents de nanocristaux semi-conducteurs*. PhD thesis, 2018.

[27] Inuk Kang and Frank W. Wise. Electronic structure and optical properties of PbS and PbSe quantum dots. *Journal of the Optical Society of America B*, 14(7):1632, July 1997.

[28] Frank W. Wise. Lead Salt Quantum Dots: the Limit of Strong Quantum Confinement. *Accounts of Chemical Research*, 33(11):773–780, November 2000.

[29] G. Allan and C. Delerue. Confinement effects in PbSe quantum wells and nanocrystals. *Physical Review B*, 70(24):245321, December 2004.

[30] J. M. An, A. Franceschetti, S. V. Dudiy, and Alex Zunger. The Peculiar Electronic Structure of PbSe Quantum Dots. *Nano Letters*, 6(12):2728–2735, December 2006.

[31] K. Overgaag, D. Vanmaekelbergh, P. Liljeroth, G. Mahieu, B. Grandidier, C. Delerue, and G. Allan. Electron-phonon coupling and intervalley splitting determine the linewidth of single-electron transport through PbSe nanocrystals. *The Journal of Chemical Physics*, 131(22):224510, December 2009.

[32] A. Aziza, E. Amzallag, and M. Balkanski. Free electron effective mass in PbSe and Pb-SnSe mixed crystals. *Solid State Communications*, 8(11):873–877, June 1970.

[33] A. Sashchiuk, L. Amirav, M. Bashouti, M. Krueger, U. Sivan, and E. Lifshitz. PbSe Nanocrystal Assemblies: Synthesis and Structural, Optical, and Electrical Characterization. *Nano Letters*, 4(1):159–165, January 2004.

[34] Wanli Ma, Sarah L. Swisher, Trevor Ewers, Jesse Engel, Vivian E. Ferry, Harry A. Atwater, and A. Paul Alivisatos. Photovoltaic Performance of Ultrasmall PbSe Quantum Dots. *ACS Nano*, 5(10):8140–8147, October 2011.

[35] W. H. Strehlow and E. L. Cook. Compilation of Energy Band Gaps in Elemental and Binary Compound Semiconductors and Insulators. *Journal of Physical and Chemical Reference Data*, 2(1):163–200, January 1973.

[36] A. Svane, N. E. Christensen, M. Cardona, A. N. Chantis, M. van Schilfgaarde, and T. Kotani. Quasiparticle self-consistent *GW* calculations for PbS, PbSe, and PbTe: Band structure and pressure coefficients. *Physical Review B*, 81(24):245120, June 2010.

[37] Iwan Moreels, Karel Lambert, David De Muynck, Frank Vanhaecke, Dirk Poelman, José C. Martins, Guy Allan, and Zeger Hens. Composition and Size-Dependent Extinction Coefficient of Colloidal PbSe Quantum Dots. *Chemistry of Materials*, 19(25):6101–6106, December 2007.

[38] Jeffrey M. Pietryga, Richard D. Schaller, Donald Werder, Michael H. Stewart, Victor I. Klimov, and Jennifer A. Hollingsworth. Pushing the Band Gap Envelope: Mid-Infrared Emitting Colloidal PbSe Quantum Dots. *Journal of the American Chemical Society*, 126(38):11752–11753, September 2004.

[39] E. Kalesaki, W. H. Evers, G. Allan, D. Vanmaekelbergh, and C. Delerue. Electronic structure of atomically coherent square semiconductor superlattices with dimensionality below two. *Physical Review B*, 88(11):115431, September 2013.

[40] A. P. Alivisatos. Perspectives on the Physical Chemistry of Semiconductor Nanocrystals. *The Journal of Physical Chemistry*, 100(31):13226–13239, January 1996.

[41] Z. Adam Peng and Xiaogang Peng. Formation of High-Quality CdTe, CdSe, and CdS Nanocrystals Using CdO as Precursor. *Journal of the American Chemical Society*, 123(1):183–184, January 2001.

[42] C. B. Murray, D. J. Norris, and M. G. Bawendi. Synthesis and characterization of nearly monodisperse CdE (E = sulfur, selenium, tellurium) semiconductor nanocrystallites. *Journal of the American Chemical Society*, 115(19):8706–8715, September 1993.

[43] Jongnam Park, Kwangjin An, Yosun Hwang, Je-Geun Park, Han-Jin Noh, Jae-Young Kim, Jae-Hoon Park, Nong-Moon Hwang, and Taeghwan Hyeon. Ultra-large-scale syntheses of monodisperse nanocrystals. *Nature Materials*, 3(12):891–895, December 2004.

[44] Yongan Andrew Yang, Huimeng Wu, Kathryn R. Williams, and Y. Charles Cao. Synthesis of CdSe and CdTe Nanocrystals without Precursor Injection. *Angewandte Chemie International Edition*, 44(41):6712–6715, October 2005.

[45] Clemens Burda, Xiaobo Chen, Radha Narayanan, and Mostafa A. El-Sayed. Chemistry and Properties of Nanocrystals of Different Shapes. *Chemical Reviews*, 105(4):1025–1102, April 2005.

[46] Victor K. LaMer and Robert H. Dinegar. Theory, Production and Mechanism of Formation of Monodispersed Hydrosols. *Journal of the American Chemical Society*, 72(11):4847–4854, November 1950.

[47] Jörg Polte. Fundamental growth principles of colloidal metal nanoparticles – a new perspective. *CrystEngComm*, 17(36):6809–6830, 2015.

[48] Sandeep Kumar and Thomas Nann. Shape Control of II–VI Semiconductor Nanomaterials. *Small*, 2(3):316–329, March 2006.

[49] Celso DeMello Donega, Peter Liljeroth, and Daniel Vanmaekelbergh. Physicochemical Evaluation of the Hot-Injection Method, a Synthesis Route for Monodisperse Nanocrystals. *Small*, 1(12):1152–1162, December 2005.

[50] Shouheng Sun and C. B. Murray. Synthesis of monodisperse cobalt nanocrystals and their assembly into magnetic superlattices (invited). *Journal of Applied Physics*, 85(8):4325–4330, April 1999.

[51] C. B. Murray, C. R. Kagan, and M. G. Bawendi. Self-Organization of CdSe Nanocrystallites into Three-Dimensional Quantum Dot Superlattices. *Science*, 270(5240):1335–1338, November 1995.

[52] Cherie R. Kagan and Christopher B. Murray. Charge transport in strongly coupled quantum dot solids. *Nature Nanotechnology*, 10(12):1013–1026, December 2015.

[53] Yao Liu, Markelle Gibbs, James Puthussery, Steven Gaik, Rachelle Ihly, Hugh W. Hillhouse, and Matt Law. Dependence of Carrier Mobility on Nanocrystal Size and Ligand Length in PbSe Nanocrystal Solids. *Nano Letters*, 10(5):1960–1969, May 2010.

[54] Yunan Gao, Michiel Aerts, C. S. Suchand Sandeep, Elise Talgorn, Tom J. Savenije, Sachin Kinge, Laurens D. A. Siebbeles, and Arjan J. Houtepen. Photoconductivity of PbSe Quantum-Dot Solids: Dependence on Ligand Anchor Group and Length. *ACS Nano*, 6(11):9606–9614, November 2012.

[55] Dong Yu, Congjun Wang, Brian L. Wehrenberg, and Philippe Guyot-Sionnest. Variable Range Hopping Conduction in Semiconductor Nanocrystal Solids. *Physical Review Letters*, 92(21):216802, May 2004.

[56] M. Drndić, M. V. Jarosz, N. Y. Morgan, M. A. Kastner, and M. G. Bawendi. Transport properties of annealed CdSe colloidal nanocrystal solids. *Journal of Applied Physics*, 92(12):7498–7503, December 2002.

[57] D. S. Ginger and N. C. Greenham. Charge injection and transport in films of CdSe nanocrystals. *Journal of Applied Physics*, 87(3):1361–1368, February 2000.

[58] Nicole Y. Morgan, C. A. Leatherdale, M. Drndic, Mirna Vitasovic, Marc A. Kastner, and Moungi Bawendi. Electronic transport in films of colloidal CdSe nanocrystals. *Physical Review B*, 66(7):075339, August 2002. arXiv: cond-mat/0204560.

[59] Elise Talgorn, Elli Moysidou, Ruben D. Abellon, Tom J. Savenije, Albert Goossens, Arjan J. Houtepen, and Laurens D. A. Siebbeles. Highly Photoconductive CdSe Quantum-Dot Films: Influence of Capping Molecules and Film Preparation Procedure. *The Journal of Physical Chemistry C*, 114(8):3441–3447, March 2010.

[60] Dong Yu, Congjun Wang, and Philippe Guyot-Sionnest. n-type conducting cdse nanocrystal solids. *Science*, 300(5623):1277–1280, 2003.

[61] M. V. Kovalenko, M. Scheele, and D. V. Talapin. Colloidal Nanocrystals with Molecular Metal Chalcogenide Surface Ligands. *Science*, 324(5933):1417–1420, June 2009.

[62] Angang Dong, Yucong Jiao, and Delia J. Milliron. Electronically Coupled Nanocrystal Superlattice Films by *in Situ* Ligand Exchange at the Liquid–Air Interface. *ACS Nano*, 7(12):10978–10984, December 2013.

[63] Moon Sung Kang, Jiyoul Lee, David J. Norris, and C. Daniel Frisbie. High Carrier Densities Achieved at Low Voltages in Ambipolar PbSe Nanocrystal Thin-Film Transistors. *Nano Letters*, 9(11):3848–3852, November 2009.

[64] Steven C. Erwin, Lijun Zu, Michael I. Haftel, Alexander L. Efros, Thomas A. Kennedy, and David J. Norris. Doping semiconductor nanocrystals. *Nature*, 436(7047):91–94, July 2005.

[65] D. J. Norris, A. L. Efros, and S. C. Erwin. Doped Nanocrystals. *Science*, 319(5871):1776–1779, March 2008.

[66] Wenyong Liu, Jong-Soo Lee, and Dmitri V. Talapin. Iii–v nanocrystals capped with molecular metal chalcogenide ligands: High electron mobility and ambipolar photoresponse. *Journal of the American Chemical Society*, 135(4):1349–1357, 2013. PMID: 23267673.

[67] Wenyong Liu, Angela Y. Chang, Richard D. Schaller, and Dmitri V. Talapin. Colloidal InSb Nanocrystals. *Journal of the American Chemical Society*, 134(50):20258–20261, December 2012.

[68] Jong-Soo Lee, Maksym V. Kovalenko, Jing Huang, Dae Sung Chung, and Dmitri V. Talapin. Band-like transport, high electron mobility and high photoconductivity in all-inorganic nanocrystal arrays. *Nature Nanotechnology*, 6(6):348–352, June 2011.

[69] Ji-Hyuk Choi, Aaron T. Fafarman, Soong Ju Oh, Dong-Kyun Ko, David K. Kim, Benjamin T. Diroll, Shin Muramoto, J. Greg Gillen, Christopher B. Murray, and Cherie R. Kagan. Bandlike Transport in Strongly Coupled and Doped Quantum Dot Solids: A Route to High-Performance Thin-Film Electronics. *Nano Letters*, 12(5):2631–2638, May 2012.

[70] Jaeyoung Jang, Dmitriy S. Dolzhnikov, Wenyong Liu, Sooji Nam, Moonsub Shim, and Dmitri V. Talapin. Solution-Processed Transistors Using Colloidal Nanocrystals with Composition-Matched Molecular "Solders": Approaching Single Crystal Mobility. *Nano Letters*, 15(10):6309–6317, October 2015.

[71] D. S. Dolzhnikov, H. Zhang, J. Jang, J. S. Son, M. G. Panthani, T. Shibata, S. Chattopadhyay, and D. V. Talapin. Composition-matched molecular "solders" for semiconductors. *Science*, 347(6220):425–428, January 2015.

[72] Jong-Soo Lee, Elena V. Shevchenko, and Dmitri V. Talapin. AuˇPbS CoreˇShell Nanocrystals: Plasmonic Absorption Enhancement and Electrical Doping via Intraparticle Charge Transfer. *Journal of the American Chemical Society*, 130(30):9673–9675, July 2008.

[73] Daniel M. Balazs, Nisrina Rizkia, Hong-Hua Fang, Dmitry N. Dirin, Jamo Momand, Bart J. Kooi, Maksym V. Kovalenko, and Maria Antonietta Loi. Colloidal Quantum Dot Inks for Single-Step-Fabricated Field-Effect Transistors: The Importance of Postdeposition Ligand Removal. *ACS Applied Materials & Interfaces*, 10(6):5626–5632, February 2018.

[74] Weon-kyu Koh, Sangameshwar R. Saudari, Aaron T. Fafarman, Cherie R. Kagan, and Christopher B. Murray. Thiocyanate-Capped PbS Nanocubes: Ambipolar Transport Enables Quantum Dot Based Circuits on a Flexible Substrate. *Nano Letters*, 11(11):4764–4767, November 2011.

[75] D. V. Talapin. PbSe Nanocrystal Solids for n- and p-Channel Thin Film Field-Effect Transistors. *Science*, 310(5745):86–89, October 2005.

[76] James E. Murphy, Matthew C. Beard, and Arthur J. Nozik. Time-Resolved Photoconductivity of PbSe Nanocrystal Arrays [†]. *The Journal of Physical Chemistry B*, 110(50):25455–25461, December 2006.

[77] Soong Ju Oh, Nathaniel E. Berry, Ji-Hyuk Choi, E. Ashley Gaulding, Taejong Paik, Sung-Hoon Hong, Christopher B. Murray, and Cherie R. Kagan. Stoichiometric Control of Lead Chalcogenide Nanocrystal Solids to Enhance Their Electronic and Optoelectronic Device Performance. *ACS Nano*, 7(3):2413–2421, March 2013.

[78] Soong Ju Oh, Zhuqing Wang, Nathaniel E. Berry, Ji-Hyuk Choi, Tianshuo Zhao, E. Ashley Gaulding, Taejong Paik, Yuming Lai, Christopher B. Murray, and Cherie R. Kagan. Engineering Charge Injection and Charge Transport for High Performance PbSe Nanocrystal Thin Film Devices and Circuits. *Nano Letters*, 14(11):6210–6216, November 2014.

[79] Yao Liu, Jason Tolentino, Markelle Gibbs, Rachelle Ihly, Craig L. Perkins, Yu Liu, Nathan Crawford, John C. Hemminger, and Matt Law. Pbse quantum dot field-effect transistors with air-stable electron mobilities above 7 cm2 v−1 s−1. *Nano Letters*, 13(4):1578–1587, 2013.

[80] Soong Ju Oh, Nathaniel E. Berry, Ji-Hyuk Choi, E. Ashley Gaulding, Hangfei Lin, Taejong Paik, Benjamin. T. Diroll, Shin Muramoto, Christopher B. Murray, and Cherie R. Kagan. Designing High-Performance PbS and PbSe Nanocrystal Electronic Devices through Stepwise, Post-Synthesis, Colloidal Atomic Layer Deposition. *Nano Letters*, 14(3):1559–1566, March 2014.

[81] Aaron T. Fafarman, Weon-kyu Koh, Benjamin T. Diroll, David K. Kim, Dong-Kyun Ko, Soong Ju Oh, Xingchen Ye, Vicky Doan-Nguyen, Michael R. Crump, Danielle C. Reifsnyder, Christopher B. Murray, and Cherie R. Kagan. Thiocyanate-Capped Nanocrystal Colloids: Vibrational Reporter of Surface Chemistry and Solution-Based Route to Enhanced Coupling in Nanocrystal Solids. *Journal of the American Chemical Society*, 133(39):15753–15761, October 2011.

[82] Christophe Delerue and D Vanmaekelbergh. Electronic band structure of zinc blende CdSe and rock salt PbSe semiconductors with silicene-type honeycomb geometry. *2D Materials*, 2(3):034008, June 2015.

[83] E. Kalesaki, C. Delerue, C. Morais Smith, W. Beugeling, G. Allan, and D. Vanmaekelbergh. Dirac Cones, Topological Edge States, and Nontrivial Flat Bands in Two-Dimensional Semiconductors with a Honeycomb Nanogeometry. *Physical Review X*, 4(1):011010, January 2014.

[84] W. Beugeling, E. Kalesaki, C. Delerue, Y.-M. Niquet, D. Vanmaekelbergh, and C. Morais Smith. Topological states in multi-orbital HgTe honeycomb lattices. *Nature Communications*, 6(1):6316, May 2015.

[85] M. P. Boneschanscher, W. H. Evers, J. J. Geuchies, T. Altantzis, B. Goris, F. T. Rabouw, S. A. P. van Rossum, H. S. J. van der Zant, L. D. A. Siebbeles, G. Van Tendeloo, I. Swart, J. Hilhorst, A. V. Petukhov, S. Bals, and D. Vanmaekelbergh. Long-range orientation and atomic attachment of nanocrystals in 2D honeycomb superlattices. *Science*, 344(6190):1377–1380, June 2014.

[86] Jaco J. Geuchies, Carlo van Overbeek, Wiel H. Evers, Bart Goris, Annick de Backer, Anjan P. Gantapara, Freddy T. Rabouw, Jan Hilhorst, Joep L. Peters, Oleg Konovalov, Andrei V. Petukhov, Marjolein Dijkstra, Laurens D. A. Siebbeles, Sandra van Aert, Sara

Bals, and Daniel Vanmaekelbergh. In situ study of the formation mechanism of two-dimensional superlattices from PbSe nanocrystals. *Nature Materials*, 15(12):1248–1254, December 2016.

[87] Haitao Zhang, Bo Hu, Liangfeng Sun, Robert Hovden, Frank W. Wise, David A. Muller, and Richard D. Robinson. Surfactant Ligand Removal and Rational Fabrication of Inorganically Connected Quantum Dots. *Nano Letters*, 11(12):5356–5361, December 2011.

[88] William J. Baumgardner, Kevin Whitham, and Tobias Hanrath. Confined-but-Connected Quantum Solids via Controlled Ligand Displacement. *Nano Letters*, 13(7):3225–3231, July 2013.

[89] Willem Walravens, Jonathan De Roo, Emile Drijvers, Stephanie ten Brinck, Eduardo Solano, Jolien Dendooven, Christophe Detavernier, Ivan Infante, and Zeger Hens. Chemically Triggered Formation of Two-Dimensional Epitaxial Quantum Dot Superlattices. *ACS Nano*, 10(7):6861–6870, July 2016.

[90] Daniel M. Balazs, Bartosz M. Matysiak, Jamo Momand, Artem G. Shulga, Maria Ibáñez, Maksym V. Kovalenko, Bart J. Kooi, and Maria Antonietta Loi. Electron Mobility of 24 cm ^{2} V $^{-1}$ s $^{-1}$ in PbSe Colloidal-Quantum-Dot Superlattices. *Advanced Materials*, 30(38):1802265, September 2018.

[91] Wiel H. Evers, Juleon M. Schins, Michiel Aerts, Aditya Kulkarni, Pierre Capiod, Maxime Berthe, Bruno Grandidier, Christophe Delerue, Herre S. J. van der Zant, Carlo van Overbeek, Joep L. Peters, Daniel Vanmaekelbergh, and Laurens D. A. Siebbeles. High charge mobility in two-dimensional percolative networks of PbSe quantum dots connected by atomic bonds. *Nature Communications*, 6(1):8195, November 2015.

[92] M. Alimoradi Jazi, V. A. E. C. Janssen, W. H. Evers, A. Tadjine, C. Delerue, L. D. A. Siebbeles, H. S. J. van der Zant, A. J. Houtepen, and D. Vanmaekelbergh. Transport Properties of a Two-Dimensional PbSe Square Superstructure in an Electrolyte-Gated Transistor. *Nano Letters*, 17(9):5238–5243, September 2017.

[93] Maryam Alimoradi Jazi, Aditya Kulkarni, Sophia Buhbut Sinai, Joep L. Peters, Eva Geschiere, Michele Failla, Christophe Delerue, Arjan J. Houtepen, Laurens D. A. Siebbeles, and Daniel Vanmaekelbergh. Room-Temperature Electron Transport in Self-Assembled Sheets of PbSe Nanocrystals with a Honeycomb Nanogeometry. *The Journal of Physical Chemistry C*, 123(22):14058–14066, June 2019.

[94] Kevin Whitham, Jun Yang, Benjamin H. Savitzky, Lena F. Kourkoutis, Frank Wise, and Tobias Hanrath. Charge transport and localization in atomically coherent quantum dot solids. *Nature Materials*, 15(5):557–563, May 2016.

[95] Willem Walravens, Eduardo Solano, Filip Geenen, Jolien Dendooven, Oleg Gorobtsov, Athmane Tadjine, Nayyera Mahmoud, Patrick Peiwen Ding, Jacob P. C. Ruff, Andrej

Singer, Gunther Roelkens, Christophe Delerue, Christophe Detavernier, and Zeger Hens. Setting Carriers Free: Healing Faulty Interfaces Promotes Delocalization and Transport in Nanocrystal Solids. *ACS Nano*, 13(11):12774–12786, November 2019.

[96] C. S. Suchand Sandeep, Jon Mikel Azpiroz, Wiel H. Evers, Simon C. Boehme, Iwan Moreels, Sachin Kinge, Laurens D. A. Siebbeles, Ivan Infante, and Arjan J. Houtepen. Epitaxially Connected PbSe Quantum-Dot Films: Controlled Neck Formation and Optoelectronic Properties. *ACS Nano*, 8(11):11499–11511, November 2014.

[97] Alex Abelson, Caroline Qian, Trenton Salk, Zhongyue Luan, Kan Fu, Jian-Guo Zheng, Jenna L. Wardini, and Matt Law. Collective topo-epitaxy in the self-assembly of a 3D quantum dot superlattice. *Nature Materials*, 19(1):49–55, January 2020.

[98] Justin C. Ondry, Matthew R. Hauwiller, and A. Paul Alivisatos. Dynamics and Removal Pathway of Edge Dislocations in Imperfectly Attached PbTe Nanocrystal Pairs: Toward Design Rules for Oriented Attachment. *ACS Nano*, 12(4):3178–3189, April 2018.

[99] Arthur R. C. McCray, Benjamin H. Savitzky, Kevin Whitham, Tobias Hanrath, and Lena F. Kourkoutis. Orientational Disorder in Epitaxially Connected Quantum Dot Solids. *ACS Nano*, 13(10):11460–11468, October 2019.

[100] Taylor Woehl. Refocusing *in Situ* Electron Microscopy: Moving beyond Visualization of Nanoparticle Self-Assembly To Gain Practical Insights into Advanced Material Fabrication. *ACS Nano*, 13(11):12272–12279, November 2019.

[101] O. Voznyy, S. M. Thon, A. H. Ip, and E. H. Sargent. Dynamic Trap Formation and Elimination in Colloidal Quantum Dots. *The Journal of Physical Chemistry Letters*, 4(6):987–992, March 2013.

[102] Carlo Giansante and Ivan Infante. Surface Traps in Colloidal Quantum Dots: A Combined Experimental and Theoretical Perspective. *The Journal of Physical Chemistry Letters*, 8(20):5209–5215, October 2017.

[103] Arjan J. Houtepen, Zeger Hens, Jonathan S. Owen, and Ivan Infante. On the origin of surface traps in colloidal ii–vi semiconductor nanocrystals. *Chemistry of Materials*, 29(2):752–761, 2017.

[104] Alexander H. Ip, Susanna M. Thon, Sjoerd Hoogland, Oleksandr Voznyy, David Zhitomirsky, Ratan Debnath, Larissa Levina, Lisa R. Rollny, Graham H. Carey, Armin Fischer, Kyle W. Kemp, Illan J. Kramer, Zhijun Ning, André J. Labelle, Kang Wei Chou, Aram Amassian, and Edward H. Sargent. Hybrid passivated colloidal quantum dot solids. *Nature Nanotechnology*, 7(9):577–582, September 2012.

[105] Peter Liljeroth, Lucian Jdira, Karin Overgaag, Bruno Grandidier, Sylvia Speller, and Dani?l Vanmaekelbergh. Can scanning tunnelling spectroscopy measure the density of

states of semiconductor quantum dots? *Physical Chemistry Chemical Physics*, 8(33):3845, 2006.

[106] T. H. Nguyen, J. Habinshuti, Y. Justo, R. Gomes, G. Mahieu, S. Godey, J. P. Nys, S. Carrillo, Z. Hens, O. Robbe, S. Turrell, and B. Grandidier. Charge carrier identification in tunneling spectroscopy of core-shell nanocrystals. *Physical Review B*, 84(19):195133, November 2011.

[107] Giuseppe Maruccio, Martin Janson, Andreas Schramm, Christian Meyer, Tomohiro Matsui, Christian Heyn, Wolfgang Hansen, Roland Wiesendanger, Massimo Rontani, and Elisa Molinari. Correlation Effects in Wave Function Mapping of Molecular Beam Epitaxy Grown Quantum Dots. *Nano Letters*, 7(9):2701–2706, September 2007.

[108] G. Binnig, H. Rohrer, Ch. Gerber, and E. Weibel. Tunneling through a controllable vacuum gap. *Applied Physics Letters*, 40(2):178–180, January 1982.

[109] G. Binnig, H. Rohrer, Ch. Gerber, and E. Weibel. Surface Studies by Scanning Tunneling Microscopy. *Physical Review Letters*, 49(1):57–61, July 1982.

[110] Gerd Binnig and Heinrich Rohrer. Scanning tunneling microscopy—from birth to adolescence. *Reviews of Modern Physics*, 59(3):615–625, July 1987.

[111] L. D. Landau and L. M. Lifshitz. *Quantum Mechanics Non-Relativistic Theory, Third Edition: Volume 3.* Butterworth-Heinemann, 1981.

[112] J. Bardeen. Tunnelling from a Many Particle Point of View. *Physical Review Letters*, 6(2):57–59, 1961.

[113] Bert Voigtländer. *Scanning Probe Microscopy: Atomic Force Microscopy and Scanning Tunneling Microscopy.* NanoScience and Technology. Springer Berlin Heidelberg, Berlin, Heidelberg, 2015.

[114] S. Vieira. The behavior and calibration of some piezoelectric ceramics used in the stm. *IBM Journal of Research and Development*, 30(5):553–556, 1986.

[115] L. Limot, J. Kröger, R. Berndt, A. Garcia-Lekue, and W. A. Hofer. Atom Transfer and Single-Adatom Contacts. *Physical Review Letters*, 94(12):126102, April 2005.

[116] N. Néel, J. Kröger, L. Limot, T. Frederiksen, M. Brandbyge, and R. Berndt. Controlled Contact to a C 60 Molecule. *Physical Review Letters*, 98(6):065502, February 2007.

[117] N. Néel, J. Kröger, L. Limot, K. Palotas, W. A. Hofer, and R. Berndt. Conductance and Kondo Effect in a Controlled Single-Atom Contact. *Physical Review Letters*, 98(1):016801, January 2007.

[118] J. Tersoff and D. R. Hamann. Theory of the scanning tunneling microscope. *Physical Review B*, 31(2):805–813, January 1985.

[119] R. M. Feenstra, W. A. Thompson, and A. P. Fein. Real-space observation of pi-bonded chains and surface disorder on Si(111)2×1. *Physical Review Letters*, 56(6):608–611, February 1986.

[120] R M Feenstra, Joseph A Stroscio, and A P Fein. TUNNELING SPECTROSCOPY OF THE Si(111)2 x 1 SURFACE. page 12.

[121] J. A. Kubby, J. E. Griffith, R. S. Becker, and J. S. Vickers. Tunneling microscopy of Ge(001). *Physical Review B*, 36(11):6079–6093, October 1987.

[122] Christophe Delerue and Michel Lannoo. *Nanostructures*. NanoScience and Technology. Springer Berlin Heidelberg, Berlin, Heidelberg, 2004.

[123] Y. M. Niquet, C. Delerue, G. Allan, and M. Lannoo. Interpretation and theory of tunneling experiments on single nanostructures. *Physical Review B*, 65(16):165334, April 2002.

[124] E. P. A. M. Bakkers, Z. Hens, A. Zunger, A. Franceschetti, L. P. Kouwenhoven, L. Gurevich, and D. Vanmaekelbergh. Shell-Tunneling Spectroscopy of the Single-Particle Energy Levels of Insulating Quantum Dots. *Nano Letters*, 1(10):551–556, October 2001.

[125] Lucian Jdira, Peter Liljeroth, Eric Stoffels, Daniël Vanmaekelbergh, and Sylvia Speller. Size-dependent single-particle energy levels and interparticle Coulomb interactions in CdSe quantum dots measured by scanning tunneling spectroscopy. *Physical Review B*, 73(11):115305, March 2006.

[126] Uri Banin, YunWei Cao, David Katz, and Oded Millo. Identi®cation of atomic-like electronic states in indium arsenide nanocrystal quantum dots. 400:3, 1999.

[127] M. Lannoo, C. Delerue, and G. Allan. Screening in Semiconductor Nanocrystallites and Its Consequences for Porous Silicon. *Physical Review Letters*, 74(17):3415–3418, April 1995.

[128] Ph Hofmann and J W Wells. Surface-sensitive conductance measurements. *Journal of Physics: Condensed Matter*, 21(1):013003, January 2009.

[129] Contact Resistance and Schottky Barriers. In *Semiconductor Material and Device Characterization*, pages 127–184. John Wiley & Sons, Inc., Hoboken, NJ, USA, April 2005.

[130] Sven Just, Marcus Blab, Stefan Korte, Vasily Cherepanov, Helmut Soltner, and Bert Voigtländer. Surface and Step Conductivities on Si(111) Surfaces. *Physical Review Letters*, 115(6):066801, August 2015.

[131] Shuji Hasegawa, Ichiro Shiraki, Takehiro Tanikawa, Christian L Petersen, Torben M Hansen, Peter Boggild, and Francois Grey. Direct measurement of surface-state conductance by microscopic four-point probe method. *Journal of Physics: Condensed Matter*, 14(35):8379–8392, September 2002.

[132] Bert Voigtländer, Vasily Cherepanov, Stefan Korte, Arthur Leis, David Cuma, Sven Just, and Felix Lüpke. Invited Review Article: Multi-tip scanning tunneling microscopy: Experimental techniques and data analysis. *Review of Scientific Instruments*, 89(10):101101, October 2018.

[133] Shuji Hasegawa, Ichiro Shiraki, Fuhito Tanabe, Rei Hobara, Taizo Kanagawa, Takehiro Tanikawa, Iwao Matsuda, Christian L. Petersen, Torben M. Hansen, Peter Boggild, and Francois Grey. ELECTRICAL CONDUCTION THROUGH SURFACE SUPERSTRUCTURES MEASURED BY MICROSCOPIC FOUR-POINT PROBES. *Surface Review and Letters*, 10(06):963–980, December 2003.

[134] I Miccoli, F Edler, H Pfnür, and C Tegenkamp. The 100th anniversary of the four-point probe technique: the role of probe geometries in isotropic and anisotropic systems. *Journal of Physics: Condensed Matter*, 27(22):223201, June 2015.

[135] L. J. van der PAUW. A METHOD OF MEASURING SPECIFIC RESISTIVITY AND HALL EFFECT OF DISCS OF ARBITRARY SHAPE. In *Semiconductor Devices: Pioneering Papers*, pages 174–182. WORLD SCIENTIFIC, March 1958.

[136] Taizo Kanagawa, Rei Hobara, Iwao Matsuda, Takehiro Tanikawa, Akiko Natori, and Shuji Hasegawa. Anisotropy in Conductance of a Quasi-One-Dimensional Metallic Surface State Measured by a Square Micro-Four-Point Probe Method. *Physical Review Letters*, 91(3):036805, July 2003.

[137] Ch Gerber, G Binnig, H Fuchs, O Marti, and H Rohrer. Scanning tunneling microscope combined with a scanning electron microscope. page 5.

[138] Rosine Coq Germanicus, Yoan Bourlier, Vincent Notot, Bruno Bérini, Valérie Demange, Maxime Berthe, Alexis Boileau, Matthieu Euchin, Yves Dumont, Damien Aureau, Mathieu Fregnaux, Bruno Grandidier, Ulrike Lüders, Adrian David, Wilfrid Prellier, Louis Biadala, and Arnaud Fouchet. Three dimensional resistance mapping of self-organized Sr3V2O8 nanorods on metallic perovskite SrVO3 matrix. *Applied Surface Science*, 510:145522, April 2020.

[139] Zhihong Nie, Alla Petukhova, and Eugenia Kumacheva. Properties and emerging applications of self-assembled structures made from inorganic nanoparticles. *Nature Nanotechnology*, 5(1):15–25, January 2010.

[140] Dmitri V. Talapin, Jong-Soo Lee, Maksym V. Kovalenko, and Elena V. Shevchenko. Prospects of Colloidal Nanocrystals for Electronic and Optoelectronic Applications. *Chemical Reviews*, 110(1):389–458, January 2010.

[141] Jong-Soo Lee, Maksym V. Kovalenko, Jing Huang, Dae Sung Chung, and Dmitri V. Talapin. Band-like transport, high electron mobility and high photoconductivity in all-inorganic nanocrystal arrays. *Nature Nanotechnology*, 6(6):348–352, June 2011.

[142] C. R. Kagan, E. Lifshitz, E. H. Sargent, and D. V. Talapin. Building devices from colloidal quantum dots. *Science*, 353(6302):aac5523–aac5523, August 2016.

[143] Tuo Wang, Roman Vaxenburg, Wenyong Liu, Sara M. Rupich, Efrat Lifshitz, Alexander L. Efros, Dmitri V. Talapin, and S. J. Sibener. Size-Dependent Energy Levels of InSb Quantum Dots Measured by Scanning Tunneling Spectroscopy. *ACS Nano*, 9(1):725–732, January 2015.

[144] Karin Overgaag, Peter Liljeroth, Bruno Grandidier, and Daniël Vanmaekelbergh. Scanning Tunneling Spectroscopy of Individual PbSe Quantum Dots and Molecular Aggregates Stabilized in an Inert Nanocrystal Matrix. *ACS Nano*, 2(3):600–606, March 2008.

[145] Peter Liljeroth, Karin Overgaag, Ana Urbieta, Bruno Grandidier, Stephen G. Hickey, and Daniël Vanmaekelbergh. Variable Orbital Coupling in a Two-Dimensional Quantum-Dot Solid Probed on a Local Scale. *Physical Review Letters*, 97(9):096803, September 2006.

[146] Jonathan S. Steckel, Brian K. H. Yen, David C. Oertel, and Moungi G. Bawendi. On the Mechanism of Lead Chalcogenide Nanocrystal Formation. *Journal of the American Chemical Society*, 128(40):13032–13033, October 2006.

[147] Boaz Alperson, Israel Rubinstein, and Gary Hodes. Identification of surface states on individual CdSe quantum dots by room-temperature conductance spectroscopy. *Physical Review B*, 63(8):081303, February 2001.

[148] B. Grandidier, Y. M. Niquet, B. Legrand, J. P. Nys, C. Priester, D. Stiévenard, J. M. Gérard, and V. Thierry-Mieg. Imaging the Wave-Function Amplitudes in Cleaved Semiconductor Quantum Boxes. *Physical Review Letters*, 85(5):1068–1071, July 2000.

[149] B. J. LeRoy, S. G. Lemay, J. Kong, and C. Dekker. Electrical generation and absorption of phonons in carbon nanotubes. *Nature*, 432(7015):371–374, November 2004.

[150] Zhixiang Sun, Ingmar Swart, Christophe Delerue, Daniël Vanmaekelbergh, and Peter Liljeroth. Orbital and Charge-Resolved Polaron States in CdSe Dots and Rods Probed by Scanning Tunneling Spectroscopy. *Physical Review Letters*, 102(19):196401, May 2009.

[151] Ned S. Wingreen, Karsten W. Jacobsen, and John W. Wilkins. Inelastic scattering in resonant tunneling. *Physical Review B*, 40(17):11834–11850, December 1989.

[152] Yang Ai-Ling, Wu Hui-Zhen, Li Zhi-Feng, Qiu Dong-Jiang, Chang Yong, Li Jian-Feng, P J McCann, and X M Fang. Raman Scattering Study of PbSe Grown on (111) BaF_2 Substrate. *Chinese Physics Letters*, 17(8):606–608, August 2000.

[153] L. Jdira, K. Overgaag, R. Stiufiuc, B. Grandidier, C. Delerue, S. Speller, and D. Vanmaekelbergh. Linewidth of resonances in scanning tunneling spectroscopy. *Physical Review B*, 77(20):205308, May 2008.

[154] A. Deshpande, W. Bao, F. Miao, C. N. Lau, and B. J. LeRoy. Spatially resolved spectroscopy of monolayer graphene on SiO2. *Physical Review B*, 79(20):205411, May 2009. arXiv: 0812.1073.

[155] J.W. Wells, J.F. Kallehauge, and Ph. Hofmann. Surface-sensitive conductance measurements on clean and stepped semiconductor surfaces: Numerical simulations of four point probe measurements. *Surface Science*, 602(10):1742–1749, May 2008.

[156] J. W. Wells, K. Handrup, J. F. Kallehauge, L. Gammelgaard, P. Bøggild, M. B. Balslev, J. E. Hansen, P. R. E. Petersen, and Ph. Hofmann. The conductivity of Bi(111) investigated with nanoscale four point probes. *Journal of Applied Physics*, 104(5):053717, September 2008.

[157] Iwao Matsuda, Masashi Ueno, Toru Hirahara, Rei Hobara, Harumo Morikawa, Canhua Liu, and Shuji Hasegawa. Electrical Resistance of a Monatomic Step on a Crystal Surface. *Physical Review Letters*, 93(23):236801, November 2004.

[158] Pierre Capiod. Caractérisation physique de nanomatériaux semi-conducteurs complexes : Des hétéro-structures aux réseaux bidimensionnels. page 175, 2014.